An investigation of gas phase ion-molecule complexes involving novel binding modes

by

Joshua Robert John Featherstone

A thesis
presented to the University of Waterloo
in fulfillment of the
thesis requirement for the degree of
Doctor of Philosophy
in
Chemistry

Waterloo, Ontario, Canada, 2021

Examining Committee Membership

The following served on the Examining Committee for this thesis. The decision of the Examining Committee is by majority vote.

External Examiner: Dr. Travis Fridgen
Professor
Memorial University, St. John's, NL, Canada

Internal-External Examiner: Dr. Andrew C. Doxey
Associate Professor
University of Waterloo, Waterloo, ON, Canada

Supervisor: Dr. Terry McMahon
Professor
University of Waterloo, Waterloo, ON, Canada

Advisory Committee: Dr. W. Scott Hopkins
Associate Professor
University of Waterloo, Waterloo, ON, Canada

Dr. P. N. Roy
Professor
University of Waterloo, Waterloo, ON, Canada

Dr. Marcel Nooijen
Professor
University of Waterloo, Waterloo, ON, Canada

Author's Declaration

This thesis consists of material all of which I authored or co-authored: see Statement of Contributions included in the thesis. This is a true copy of the thesis, including any required final revisions, as accepted by my examiners.

I understand that my thesis may be made electronically available to the public.

Statement of Contributions

This thesis contains works which have been published in peer reviewed journals. These works have been acknowledged in the references section of this thesis. My contributions, relating to this thesis are summarized below:

The contents of Chapter 7 are reproduced from the following publication:

Featherstone, J., Chong, T., Martens, J. K., Oomens, J., & McMahon, T. B. (2018). Inverse Sandwich Cyclopentadienyl Complexes of Sodium in the Gas Phase. Journal of Physical Chemistry A. https://doi.org/10.1021/acs.jpca.8b09366

Abstract

In this thesis, an innovative method is introduced to advance the study of gas phase clusters and used to analyse a number of novel binding modes. The systematic sampling of cluster surfaces (SSCS) routine, introduced in Chapter 3, is a computational technique that identifies cluster geometries by examining subsequent additions of solvent molecules along the surface of a core cluster. This technique examines the electrostatic potential of the solvent and cluster to determine favourable sites of interaction. This technique was found to result in a ten-fold increase in efficiency over common Monte-Carlo cluster geometry routines.

Utilizing the SSCS routine, a highly debated topic in gas-phase chemistry was investigated, does electrospray ionization (ESI) sample gas phase or solution phase structures? This topic was investigated in Chapter 4, using deprotonated para-hydroxybenzoic acid and examined the solution phase (carboxylate deprotonated) and gas phase (phenoxide deprotonated) preferred tautomers. Numerous studies have argued for and against tautomer preference, while they missed an important underlying factor, do ESI spray conditions favour one or the other. Six solvents were selected to showcase the transition from the gas phase to the solution phase for one to five solvent molecules. This examination found that both protic and aprotic solvents showed a steady transition to 'solution phase' conditions at room temperature. Varying ESI spray conditions found an increase in temperature to result in reduced solution phase preference, with this effect being more drastic for some solvents than others. Thus, the importance of comparing ESI spray conditions is highlighted by this study wherein, electrospray ionization samples structures based off the energy available to the system on-route to the ion trap.

In Chapter 5 and 6, all-cis hexafluorocyclohexane, all-cis pentafluorocyclohexanol, and all-cis hexa-trifluoromethyl-cyclohexane, were studied for their unique ability to bind both cationic and anionic species. It was found that these molecules possess significant dipole moments resulting in substantial propensity for binding ionic species and allowing for the formation of homogeneous dipole bound dimers. These dipole bound dimers were found to readily interact with both cationic and anionic species expanding the number of available binding motifs. These various features lend to a number of novel binding modes with ionic species in the gas phase.

Lastly, Chapter 7 examines the cation-π interactions of inverse Sandwich Cyclopentadienyl Complexes of Sodium in the Gas Phase. This system was found to readily undergo cation-π interactions, with monomer, dimer, and trimer interactions all being found experimentally. The vibrational modes of these systems required a study of anharmonic vibrational modes due to their unconventional nature. Computational investigation found that as the inverse sandwich complexes grew in size, so too did the favourability for binding additional sandwich subunits. Computational limitations prevented the ability to determine at what size the system would no longer readily bind additional subunits.

Acknowledgements

I am proud of what I have accomplished and am grateful to everyone who has helped me over the years. First, I would like to thank my supervisor, Dr. Terry McMahon, for giving me a chance and allowing me to continue working in his research lab since 2014. From this, I have developed a wealth of knowledge for coding and ion chemistry which has been invaluable. I also greatly appreciate him bringing me to both the Netherlands and France to participate in infrared multiple photon dissociation experiments. Aside from fostering my endeavours to explore new potential areas of ion chemistry, he has been a patient mentor and a friend. I have always enjoyed our time together and am sad it is coming to a close.

Second, I would like to thank Dr. W. Scott Hopkins, for providing the inspiration for many coding projects over the years. He also provided me the opportunity to explore differential mobility spectrometry and the possibilities to combine it with computational techniques to develop potential drug candidates. Though this was frustrating at times, it was always rewarding. He has been an excellent mentor for developing my understanding of the finer details behind the processes of gas phase ion chemistry in both his reading and theory courses.

I would like to thank a number of staff at the university for the various opportunities they have provided me. Heartfelt thanks to Dr. Rick Marta who first introduced me to the McMahon lab. I doubt I would have come this far otherwise. Dr. Marcel Nooijen provided excellent support to me in his special topics course while I was developing my new routine. Dr. P. N. Roy provided excellent feedback which helped me to improve and better analyze the various computational projects I investigated. Finally, I would like to thank Stacey Lavery for the very rewarding and enjoyable teaching assistant experiences which have allowed me to connect with so many students in a positive environment.

Numerous colleagues also deserve thanks. Dr. Pat Carr was a significant help during my comprehensive exam studies, I could always rely on him to walk me through a problem. I thoroughly enjoyed working with Mike Lecours on the Basin Hopping algorithm and have been sure to comment on my code ever since. Christian Ieritano has been a great help for a number of computational projects over the years and always been willing to answer my questions. Zack Bowman was an excellent study partner; while I do not miss spending hours cursing questions with solutions explained in obscure textbooks, I am glad it was time spent together.

Lastly, I would like to thank my family and friends who supported me despite that I was an insufferable grouch, who disappeared for a year to spend my every waking moment coding, and complained relentlessly. Special thanks to Catherine, Daniel, Margaret, and Bill.

Table of Contents

List of Tables

List of Figures

Acronyms

β-Ala β-Alaine. 31

ωB97X-D Modified Becke 97 exchange-dipole moment. ix, xii, 5, 38, 41, 43, 44, 47, 51, 56, 60

B3LYP Becke, 3-parameter, Lee–Yang–Parr. xiii, 4, 5, 51, 54–56, 60

BH Basin Hopping. 2, 14, 15, 31, 33–36, 102

BSE basis set exchange. 52, 77

C Coulombic. 17, 18, 20, 22, 27, 29

CLIO Centre de Laser Infrarouge d'Orsay. xi, 10, 13, 50, 76

Cp cyclopentadienyl. 91–94, 97, 100

DFT density functional theory. xi, 4, 5, 23, 26–29, 35, 38, 51, 52, 54, 56, 73, 76

DMS differential mobility spectrometry. 2

DMSO Dimethyl sulfoxide. 42

ESI electrospray ionisation. vii, 2, 9, 11, 21, 37–41, 45, 48, 50, 57, 68, 71, 73, 76, 87, 93, 99, 102

FEL free electron laser. xi, 10–12, 50, 51, 76, 93

FELIX Free Electron Lasers for Infrared eXperiments. 10

FT-ICR Fourier transform ion cyclotron resonance. 11

GD3 Grimme Dispersion 3. ix, x, 51, 56, 70, 76, 80, 84, 88

GD3BJ Grimme Dispersion 3 with Becke-Johnson damping. xii, 32

Gly Glycine. 31

HF Hartree-Fock. 4, 29, 31

HF-3c Grimme's 3-correct Hatree-Fock method. ix, 23, 24, 29

HFCH all-cis 1,2,3,4,5,6-hexafluorocyclohexane. ix, xii, xiii, 3, 49–55, 57, 59–69, 71–75, 77, 80, 88, 90, 103

HTFMCH all-cis 1,2,3,4,5,6-hexa-trifluoromethyl-cyclohexane. x, xiii, xiv, 3, 74, 75, 87–90, 103

ICR ion cyclotron resonance. 37

IR infrared. 93

IRMPD infrared multiple photon dissociation. xi, xiii, xiv, 1, 3, 10, 11, 13, 50–52, 59, 61–63, 67, 69, 72, 73, 76, 93, 95, 96, 98, 101, 103

IRPD infrared predissociation. 31

IVR intramolecular vibrational energy redistribution. xi, 12, 13

M06-2X Minnesota 06-2X. ix, x, 4, 51, 56, 60, 70, 76, 77, 80, 84, 88

MC Monte Carlo. 2, 14, 15

MP2 Møller–Plesset perturbation theory second order. 4, 51, 56, 60, 76

MS mass spectrometry. 1, 87

NBO6 natural bond orbital 6th edition. xiv, 75, 77

NIST National Institute of Standards and Technology. 52

PCM Polarizable Continuum Model. 38

PES potential energy surface. xii, 14, 15, 21, 33, 35, 49, 50

PFCHOL all-cis 1,2,3,4,5,6-pentafluorocyclohexanol. ix, xiii, xiv, 3, 74, 76–78, 80–88, 90, 103

PHBA para-hydroxybenzoic acid. vii, xii, 2, 23, 25, 37–39, 41–44, 46, 102

RMSD root mean square difference. 52, 76

SCRF solvent cavity reaction field. 38

SSCS systematic sampling of cluster surfaces. vii, xi, xii, 2, 5, 15, 16, 21, 24, 26, 29–36, 38, 102

TAS tris(dimethylamino)sulfonium. 92

Trp tryptophan. 33, 34

UFF universal force field. ix, 15, 18–23, 26

VdW van der Waals. xi, 18, 20, 23, 27–29

ZPVE zero-point vibrational energy. 52, 76

Chapter 1

Introduction

The study of biologically relevant cyclic species provides an opportunity to further our understanding of the non-covalent interactions that enable life to exist. Nucleic acids, the genetic material required for all life, are entirely composed of cyclic motifs.[1,2] Cyclic species also encompass constituent cyclic amino acids found in the proteins encoding genetic material which enable proteins to adopt conformations that enable life to exist.[3–5] Most biologically relevant cyclic species are aromatic, which facilitate the formation of stacked π motifs, as seen in base pair stacking of the double helix of nucleic acids.[6–8] π systems are a result of conjugated cyclic species, which is a system of connected p orbitals with delocalized electrons throughout the ring, resulting in a density of electrons above and below the ring.[9,10] Assessing the configurations accessible to clusters containing cyclic elements with computational and experimental techniques provides a foundation for understanding these systems. The work described herein, assists in defining model chemistries to study cyclic species highlighting strengths and uncovering deficiencies, and thereby assisting theoreticians in their efforts to improvement upon current models.

In this thesis, a number of substituted cyclic species will be studied to examine the gas phase clustering of hydrogen bonding, charge dipole, and cation-π bound species. Research on these species will be done using a tandem experimental and theoretical approach. Cluster species have been studied experimentally using mass spectrometry (MS) in tandem with infrared multiple photon dissociation (IRMPD) and interpreted using quantum chemical calculations as outlined in Chapter 2. These calculations are supplemented with a new methodology used in the discovery of cluster geometries to allow for a thorough investigation of experimental gas phase clusters. Through these studies, a deeper understanding of experimental conditions and how they might influence cluster populations, can be realized to improve the precision of future experiments.

In Chapter 3, a new method is described to enable the study of microsolvated cyclic species in the gas phase. It should be noted that this method is equally applicable to non-cyclic species.

The methodology serves as a more efficient means of sampling the potential energy landscape of microsolvated clusters, which is beneficial to the field of differential mobility spectrometry (DMS).[11–14] The systematic sampling of cluster surfaces (SSCS) routine, introduced herein, is a computational technique that identifies cluster geometries by examining subsequent additions of secondary molecules along the surface of a core cluster. The surface of a cluster refers to the areas where a secondary molecule may interact, governed by the electrostatic potential of the ion core. By coupling the charge density of the ion core with the electrostatic potential of a secondary molecule, time can be saved by removing redundant locations of study on a cluster's surface. For example, when clustering with an anion, it can be concluded that areas of negative charge density on the cluster surface are pointless to examine due to repulsive forces. This technique is advantageous over classical discovery methods such as Monte Carlo (MC) and Basin Hopping (BH), which randomly distort cluster geometries to discover local minima geometries, resulting in redundant local minima being sampled multiple times by random optimization within the Boltzmann window.[15–17]

Chapter 4 addresses a highly debated topic in gas-phase chemistry: does electrospray ionisation (ESI) sample gas phase or solution phase structures? To evaluate this question, a model cyclic species with well-characterized biological significance was chosen.[18–22] Specifically, deprotonated para-hydroxybenzoic acid (PHBA) acid was selected for its wealth of debate in this very topic as seen in literature. In the solution phase, the carboxylate tautomer is stabilized by formation of extended solvent networks at the site of deprotonation. However, intramolecular stabilizing interactions take precedence in the absence of solvent, shifting the population distribution of the system towards the charge delocalized phenoxide tautomer. Experimental study by a number of research groups have reached contradictory conclusions to the sampling of ESI, some stating that the solvent type determines phase selection and others stating one or the other solvent type is always preferred.[23–26] However, these experiments failed to evaluate the effect ESI spray conditions have on droplet formation and the resulting populations for each tautomer. This brings about two interesting questions: are tautomeric equilibria solvent dependent and what degree of microsolvation is required to shift the phenoxide tautomer to the carboxylate tautomer in the gas phase? To remedy this, a theoretical evaluation of various protic and aprotic solvents at varying temperatures was conducted to simulate various ESI spray conditions. Solvent

clusters were determined using the routine described in Chapter 3, and evaluated at various temperatures by employing the population analysis described in Chapter 2.

Another curious cyclic species is all-cis 1,2,3,4,5,6-hexafluorocyclohexane (HFCH), which exhibits a large propensity for binding ionic species, with binding enthalpies for cationic species rivalling those of substantially larger crown ethers.[27–29] This molecule, as discussed in Chapter 5, is a substituted cyclohexane species which possesses a facial polarization arising from the contrast between the C-H and C-F bonds on the opposite faces, resulting in a significant dipole moment. Substitutions to the fluorine face, as shown in Chapter 6 for all-cis 1,2,3,4,5,6-pentafluorocyclohexanol (PFCHOL) and all-cis 1,2,3,4,5,6-hexa-trifluoromethyl-cyclohexane (HTFMCH), result in a weakened dipole moment, but an increase in the complexity of binding motifs. In addition, it was found that these substituted cyclohexanes readily undergo interactions with other molecules, including themselves, resulting in the formation of dipole bound dimers. These dipole bound dimers were also found to readily undergo interactions with anionic and cationic species, showing the potential for a number of several binding modes in the gas phase that have yet to be reported in the literature.

Lastly, Chapter 7 examines the novel binding interactions of cation-π systems in cyclic species. Cation-π interactions are of high importance for study as they can serve to stabilize protein structures and it has reported that over one-fourth of all tryptophans in the Protein Data Bank undergo energetically significant cation-π interactions.[30–32] This study evaluated the cation-π interactions of inverse Sandwich Cyclopentadienyl Complexes of Sodium in the Gas Phase. This system was selected due to the limited number of ion chemistry studies on metallocene complexes.[33–39] Evaluation of the system experimentally showed a substantial propensity in the formation of cation-π complexes, readily forming monomer, dimers, and trimers, with evidence of larger clusters existing, albeit in populations too low for study by IRMPD.

In summary, this thesis uses a number of cyclic systems to explain and expand on the knowledge of binding motifs in gas phase ion chemistry. It introduces a new methodology for determining candidate geometries for use in tandem study with experiment, and tackles concepts highly debated in literature. This work demonstrates that cyclic species suggests that there is a wealth of information waiting to be discovered.

Chapter 2

Methods

2.1 Computational

2.1.1 Density Functional Theory

Due to constant development, density functional theory (DFT) methods are an extremely useful tool for achieving accuracy comparable to that of higher levels of theory, such as Møller–Plesset perturbation theory second order (MP2), with a fraction of the computational cost. The speed of such methods is a result of treating the spatially dependent electron density, rather than treating each electron independently. In its most basic form the electron density approximation of Kohn and Sham can be defined by the summation of the kinetic energy, electron-nuclear interaction energy, Coulomb energy, and the exchange/correlation energy.[40] Modifications and inclusion of additional terms have led to a number of unique DFT methods that each have their own strengths and weaknesses.[41–44]

One of the most common DFT methods, due to its speed and accuracy, is the Becke, 3-parameter, Lee–Yang–Parr (B3LYP) method. This hybrid functional method is the combination of Hartree-Fock (HF) theory with the electron density approximation.[45–47] It has been used extensively for a significant number of years showing excellent performance across a large range of chemical systems.[29,48–50]

Rather than use B3LYP in all cases, a more targeted method can be used to increase the accuracy when deemed necessary. One such targeted method is the Minnesota 06-2X (M06-2X) method, selected for its accuracy with simple fluorocarbon species.[51–54] This method shows a significant increase in accuracy when calculating the binding energies of fluorocarbon species, without requiring the assistance of high levels of theory to account for electron approximations.

More recently, functionals that include nonlocal correlations have been used to improve on

the accuracy of DFT methods. One such method, Modified Becke 97 exchange-dipole moment (ωB97X-D), was found to be one of the most accurate methods for calculating energies as found by Mardirossian and Head-Gordon in a comparison of 200 DFT methods comparing 5000 data points.[52,55] While this method has shown high accuracy, it was found to be insufficient in sampling the ionic species with a large number of electrons in Chapter 5, failing to correctly account for effective core potentials. Thus, when examining simple organic systems containing row one through three elements the ωB97X-D method was selected, while the M06-2X method was used in all other cases.

Where appropriate, this method was found to be more effective than B3LYP for determining infrared vibrational spectra.

Initial structures for analysis by DFT were determined by chemical intuition where appropriate or the systematic sampling of cluster surfaces (SSCS) algorithm introduced in chapter 3. It is beneficial to provide DFT methods with a reasonable initial guess structure to reduce the likelihood of optimizing to a transition state or high energy minimum structure.

2.1.2 Population analysis and thermodynamic quantities of gas phase isomers

A number of chapters in this thesis examine clusters that have a number of possible isomers at a given size, resulting in a population of isomers at a given temperature. As the temperature of a system changes, so too does the relative population of each isomer in the system. Thus, the need to develop a routine to examine the isomers of a cluster was required to properly examine populations at a given temperature.

While most of this process can be performed by calling a Gaussian link to execute a change in temperature for thermochemistry, it becomes unreasonable when a population contains a significant number of isomers. Utilizing the Gaussian link results in a file for each temperature specified, meaning an isomer could have upwards of 50 to 100 files depending on the temperature range and increment specified. Therefore, a routine was developed both to determine thermochemical values at various temperatures and determine relative populations for isomers in a cluster.

The thermodynamic quantites of a system are a sum of contributions from translational motion,

electronic motion, rotational motion, and vibrational motion. The thermodynamic quantities consist of entropy (S), internal thermal energy (E), and heat capacity (C).[56–58] These quantities can be calculated using the respective partition function of each motion. Additionally, where used, the ideal gas constant (R) is in units of $J*K^{-1}*mol^{-1}$.

The translational contribution is calculated using the mass, temperature, and pressure the system is experiencing. The translational entropy (S_t) is calculated using the translation partition function (q_t), found in equation (2.1). In their simplest forms the contributions to internal thermal energy (E_t) and heat capacity (C_t) are $\frac{3}{2}$RT and $\frac{3}{2}$R respectively.

$$\begin{aligned} q_t &= \left(\frac{2\pi m k_B T}{h^2}\right)^{\frac{3}{2}} \left(\frac{k_B T}{P}\right) \\ S_t &= R\left(ln(q_t e) + T\left(\frac{3}{2T}\right)\right) \\ &= R(ln(q_t) + 2.5) \end{aligned} \tag{2.1}$$

The electronic contribution is calculated using the spin multiplicity of the system with no reliance on temperature. This assumption is made as excited states are assumed to be inaccessible at any temperature due to k_BT being significantly smaller than the first electronic excitation energy.[56–58] This means that the derivatives for the electronic partition function with respect to temperature are both zero for the electronic heat capacity and internal thermal energy. The entropy (S_e) is calculated in simplest terms via equation (2.2).

$$S_e = R(ln(\omega_\theta)) \tag{2.2}$$

The rotational and vibrational contributions require rotational and vibrational temperatures respectively. While these values can be manually calculated they are easily accessible in the output of a Gaussian frequency calculation. For all intents and purposes, these values have been determined at a temperature of 298.15 K and a pressure of 1 atm for calculations seen throughout this thesis.

The contribution from rotational motion posed the largest obstacle as its contribution is depen-

dent on the moment of inertia of the system. In the case of a single atom there is no moment of inertia, in the sense that a single atom does not act like a rigid rotor, meaning the rotational contribution from rotational temperatures for a single atom is zero for all thermodynamic quantities. The next case was that of linear molecules, which possess a single moment of inertia, and therefore a single rotational temperature. This rotational temperature (Θ_r) is calculated by Gaussian as described in equation (2.3), where it is then applied to the rotational partition function (q_r) and finally used to solve for entropy (S_r). In their simplest forms the contributions to internal thermal energy (E_r) and heat capacity (C_r) are RT and R, respectively.

$$\begin{aligned} \Theta_r &= \frac{h^2}{8\pi^2 I k_B} \\ q_r &= \frac{1}{\sigma_r}\frac{T}{\Theta_r} \\ S_r &= R(ln(q_r)+1) \end{aligned} \tag{2.3}$$

For non-linear systems the partition function is significantly more complex, containing rotational temperatures for the x ($\Theta_{r,x}$), y ($\Theta_{r,y}$), and z ($\Theta_{r,z}$) axes. The calculation of the rotational partition function (q_r) and entropy (S_r) for a non-linear system is described in equation (2.4). In their simplest forms the contributions to internal thermal energy (E_r) and heat capacity (C_r) are $\frac{3}{2}$RT and $\frac{3}{2}$R respectively.

$$\begin{aligned} q_r &= \frac{\pi^{\frac{1}{2}}}{\sigma_r}\left(\frac{T^{\frac{3}{2}}}{(\Theta_{r,x}\Theta_{r,y}\Theta_{r,z})^{\frac{1}{2}}}\right) \\ S_r &= R(ln(q_r)+\frac{3}{2}) \end{aligned} \tag{2.4}$$

Lastly, the contribution by vibrational motion is determined by the summation of vibrational temperatures ($\Theta_{v,K}$) in the system. When calculating the vibrational temperatures, Gaussian ignores imaginary frequencies and only reports the real vibrational modes of a system.[58] Additionally, Gaussian chooses the zero reference point as the bottom of the internuclear potential energy well, or the first vibrational level. The vibrational entropy (S_v) in the simplest

form is calculated using equation (2.5).

$$S_v = R\sum_K \left(\frac{\Theta_{v,K}/T}{e^{\Theta_{v,K}/T}-1} - ln(1-e^{-\Theta_{v,K}/T}) \right) \tag{2.5}$$

The calculation for the vibrational motion contribution to the internal electronic energy (E_v) and heat capacity (C_v) are rather complex when compared to the other motions. The calculation for the two can be seen in equation (2.6).

$$\begin{aligned} E_v &= R\sum_K \Theta_{v,K}\left(\frac{1}{2}+\frac{1}{e^{\Theta_{v,K}/T}-1}\right) \\ C_v &= R\sum_K e^{\Theta_{v,K}/T}\left(\frac{\Theta_{v,K}/T}{e^{-\Theta_{v,K}/T}-1}\right)^2 \end{aligned} \tag{2.6}$$

Once the contribution from each motion has been determined the total electronic energy, correction to enthalpy, and correction to Gibbs energy can be determined. These values are determined using the equations as seen in equation (2.7).

$$\begin{aligned} E_{tot} &= E_t + E_r + E_v \\ S_{tot} &= S_t + S_r + S_e + S_v \\ H_{corr} &= E_{tot} + RT \\ G_{corr} &= H_{corr} - TS_{tot} \end{aligned} \tag{2.7}$$

By calculating these thermodynamic quantities, the change in population for a group of isomers at each respective temperature can be determined. The change in population is determined by a comparison of the weighted free energy of each isomer at a given temperature. This is done by taking the relative energy of each isomer (ΔG^i_{rel}), applying a Boltzmann weighting factor (G^i_{BW}), and dividing by the total weight of the population (G^k_{BW}) to determine an isomer's weighted population (ρ^i), as seen in equation (2.8).

$$\begin{aligned} \Delta G^i_{rel} &= G^i - G^{min} \\ G^i_{BW} &= e^{-\Delta G^i_{rel}/RT} \\ \rho^i(T) &= \frac{G^i_{BW}}{G^k_{BW}} \end{aligned} \tag{2.8}$$

This process can then be expanded to compare cluster populations ($\rho_n^{(k)}(T)$) of different sizes (n), which include all isomers (k), at a given temperature (T), by comparing the weighted free energy of formation for each cluster size ($G_n^{(k)}(T)$), as seen in equation (2.9).

$$\begin{aligned} G^{(k)}_n(T) &= \sum_i \rho^i_n(T) \cdot G^i_n \\ \rho^{(k)}_n(T) &= \frac{e^{(-G^{(k)}_n(T)/RT)}}{\sum_n e^{(-G^{(k)}_n(T)/RT)}} \end{aligned} \tag{2.9}$$

2.2 Experimental

2.2.1 Electrospray Ionization

Ionic complexes are generated in the gas phase by creating an aerosol from a solution through a process known as electrospray ionisation (ESI). Analytes are first prepared in a volatile solution to promote flow, reduce surface tension, and increase evaporation.[59] The solution is then pumped through a charged capillary with a voltage between 2-6 kV resulting in a fine spray of charged droplets.[60] The spray is the result of reaching a threshold voltage on the capillary inducing the formation of a Taylor cone in the solution. A Taylor cone is an inversion of the surface tension on the rounded tip of a solution into a jet of liquid.[61] This process produces droplets that have a 1 µm to 10 µm diameter containing $\sim$ 150,000 analyte molecules per 1 µm diameter.[61,62] The droplets composed of analyte and solvent then travel through an evaporation chamber containing a nebulizing gas, typically N_2, and high temperature (350 - 500 K) to induce thermal evaporation.[60,63] The droplets shrink via evaporation until a critical threshold known as the Rayleigh stability limit is met.[64,65] At this limit the repulsive force of the analyte ions

exceed the strength of the surface tension of the droplet resulting in a Coulombic explosion.[64,65] This explosion occurs via the formation of a Taylor cone expelling ions to create a smaller highly charged droplet.[66,67] This process continues until the droplets become sufficiently small or reach the counter-electrode where they then continue through to the rest of the instrument.

This process is outlined in **Figure 2.1**, where cationic species are being selected for analysis. By applying a positive charge to the capillary negative ions will be drawn out of solution via electrochemical discharge towards the walls of the capillary and positive species will be pushed towards the center of the stream.[59] A negative charge applied to the counter-electrode is used to guide cationic species towards the outlet for delivery to the rest of the instrumental set-up.

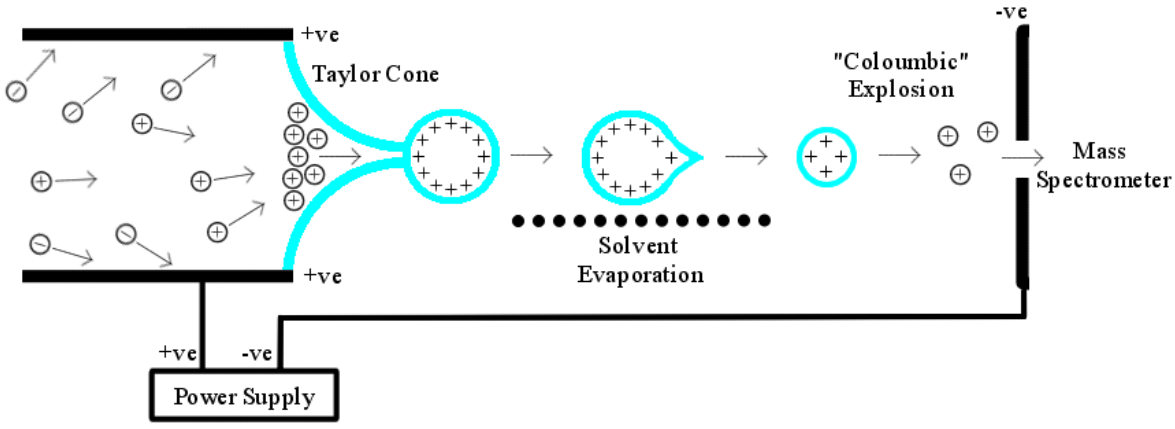

Figure 2.1: An example of selecting for positive ions using electrospray ionization. Spraying the solution into an aerosol allows for the evaporation of solvent and separation of charge by use of a high voltage plates attracting or repelling charge.

2.2.2 Infrared Multiple Photon Dissociation

infrared multiple photon dissociation (IRMPD) is a technique used to measure the vibrational fingerprint of a gas-phase ion. This vibration fingerprint is a distinct set of vibrational modes that can be observed throughout the 600 - 2000 cm^{-1} region.[68–71] IRMPD has been used to study a wide variety of molecular ions and has been described in great detail in literature.[29,50,72–78] This technique was selected due to its ability to elucidate ionic structures when used in tandem with simulations. The vibrational spectra presented in this thesis were collected at the following free electron laser (FEL) facilities: the Centre de Laser Infrarouge d'Orsay (CLIO) facility in Orsay, France and the Free Electron Lasers for Infrared eXperiments

(FELIX) facility in Nijmegen, Netherlands.[79–81]

Studying the vibrational spectrum of an ionic species requires multiple photons pumping vibrational energy into the species eventually leading to fragmentation when a dissociation threshold is met. These high energy photons can be produced using synchrotron radiation emitted by a FEL beam line. Initially, a beam of electrons is accelerated by 10 - 50 MeV before entering the undulator. The undulator is composed of a series of magnets that have alternating poles. When the electron beam enters the undulator, the beam undergoes a sinusoidal wiggling motion and emits radiation. This radiation is captured in an optical cavity allowing electron bunches that wiggle in the undulator to form coherent radition, otherwise known as photons.[71] The wavelength of these photons can be adjusted by changing the spacing between the magnets in the undulator resulting in a spectral range of 6.6 to 3500 cm^{-1}. Although the photons can occupy a large wavelength range, the power of the beam is normally insufficient for the process of IRMPD outside of the 600 - 2000 cm^{-1} region. These photons are trapped within an optical cavity by mirrors situated on both ends of the undulator and then redirected to an instrument for use in experiments. The process for generating high energy photons using the FEL beam line is outlined in **Figure 2.2**.

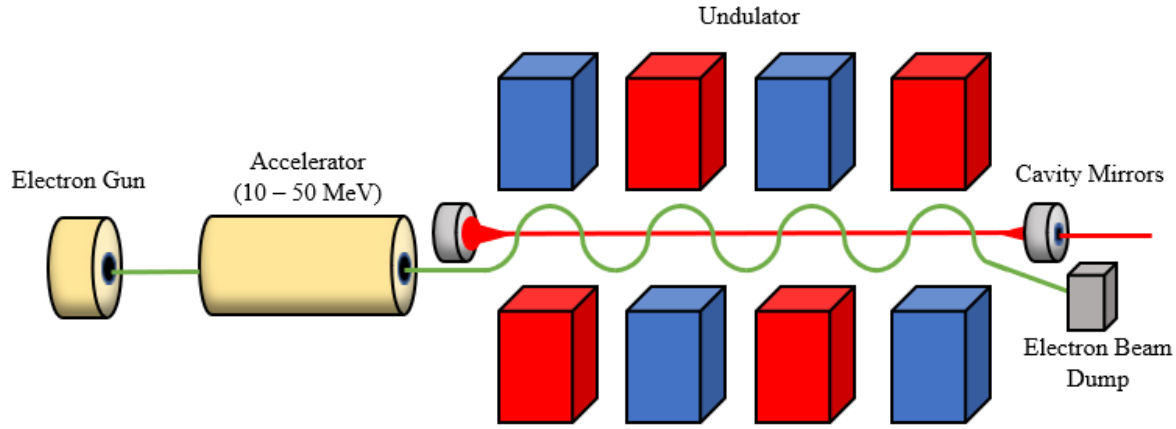

Figure 2.2: Diagram illustrating the generation of high energy photons using synchrotron radiation in an FEL.

The high energy photons generated by the FEL are then directed to one of two locations to examine the vibrational modes of an ionic species. In experiments that do not require high accuracy in mass to charge ratio, a Bruker Esquire 3000+ mass spectrometer can be used for analysis. In experiments requiring high accuracy in mass to charge ratio an Fourier transform ion cyclotron resonance (FT-ICR) can be used.[69,70] The Esquire is the preferred mass spectrometer

used in analysis because the scan speed is roughly five times that of the FT-ICR.

The first step in IRMPD is generating ions through the process of ESI, where a voltage of 5 kV is applied to the ESI capillary at a temperature of 478 K. These ions then pass into the mass spectrometer where they are held in the trap and subjected to high energy photons. To reduce the potential for non-IRMPD chemical reactions occurring inside the ion trap the temperature is set to 323 K and the pressure set to $\sim$ 1 - 10^{-3} Torr.[82,83] Ideally, this removes energy and the number of ionic collisions possible when ions are isolated in the ion trap.

When an ion trapped in the cell is subjected to a high energy photon the ion may be excited to a higher energy state (v = 1). The energy from the excited state can then be passed to the 'quasi-continuum' coupled vibrational energy levels known as bath states.[71] The process of energy redistribution into the bath states is known as intramolecular vibrational energy redistribution (IVR). When the energy is redistributed via IVR the excited mode of the ion returns to the ground state (v = 0). This then allows the ion to absorb the energy of another photon. This process continues until a thermodynamic threshold is reached and the ion fragments, as outlined in **Figure 2.3**.

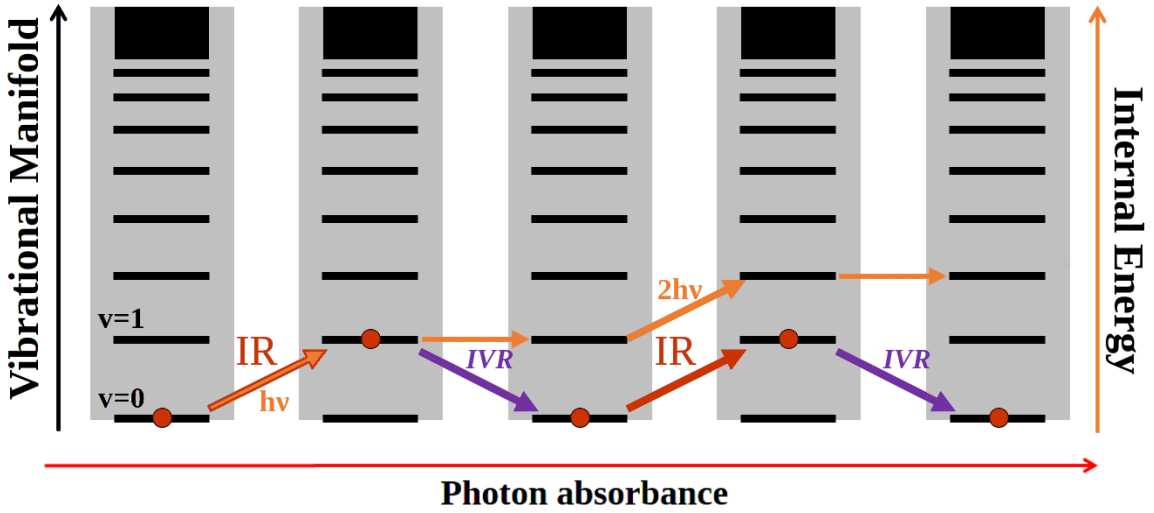

Figure 2.3: The cyclic nature of the IVR process. A high energy photon excites a normal mode to an excited state (v = 1). In this excited state the energy is redistributed to the bath states of the ion, illustrated by the red line, returning the normal mode to the ground state (v = 0). This cycle continues until a thermodynamic threshold is reached.

The process of IVR is induced at FEL facilities via pulsed photon bursts, as seen in **Figure 2.4**.

The ion of interest is bombarded by photons for 10 µs at a set wavelength, each burst is 1 ps and occurs every 16 ns, resulting in a total of 625 bursts. The ion is then given the remaining time to react to the energy distributed in the bath states before another cycle occurs.[79,80] These cycles occur approximately ten times per wavelength and step in sizes of 2.5 - 3.0 cm^{-1}.

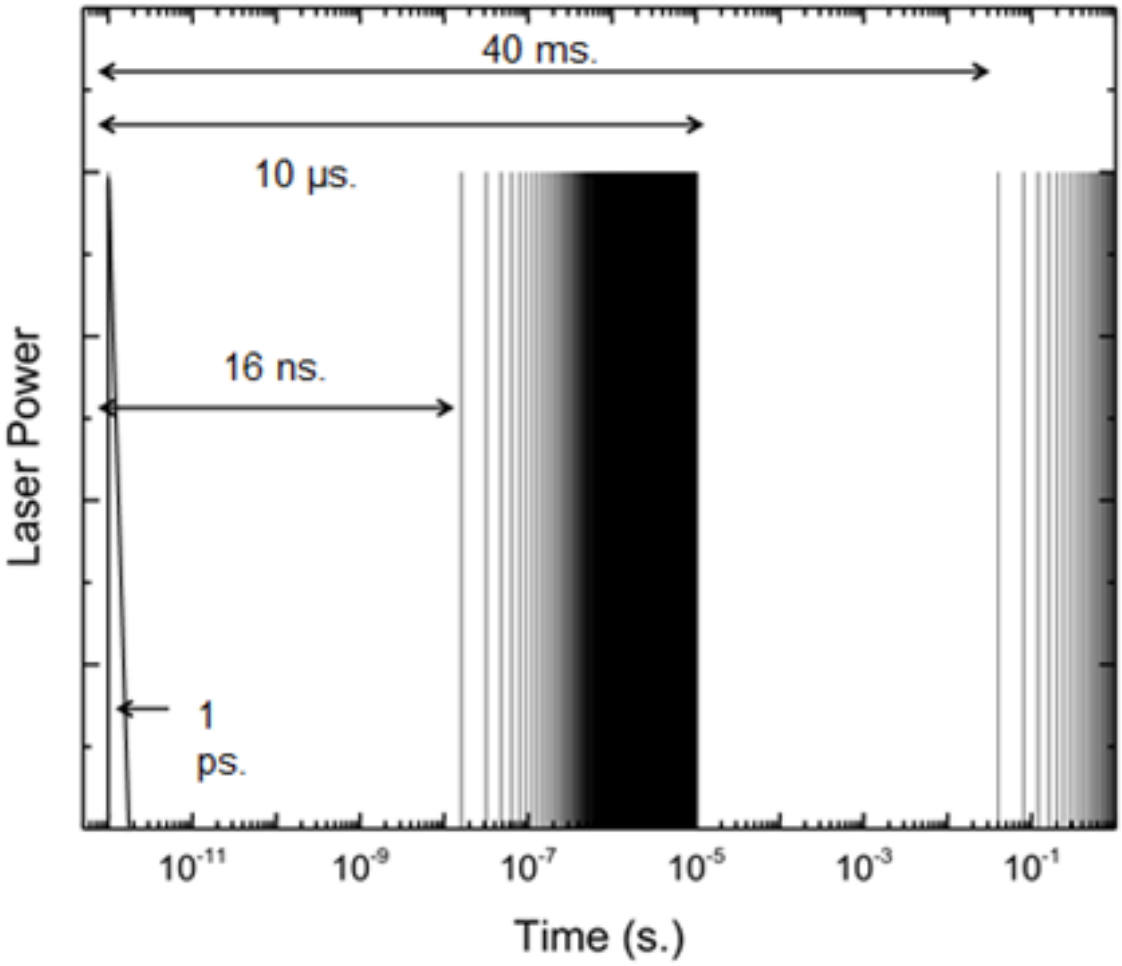

Figure 2.4: IRMPD pulse train produced at the CLIO laser facility.[84] The process of IVR is induced by pulsing the laser for 1 ps every 16 ns. This cycling continues for 10 µs *before shifting to another wavelength.*

Tracking the intensity of the ion allows one to observe its depletion upon exposure to multiple high energy photons. The ion may fragment into smaller ions observable in the mass spectrometer or may produce ions outside of the observable mass window. The efficiency of fragmentation is determined by the logarithmic ratio of fragment ions to parent ions, as seen in equation (2.10), recorded as a function of the wavelength of the photons.[71,75]

$$F_{eff} = -ln(\frac{\sum I_{par}}{\sum I_{par} + \sum I_{frag}}) \tag{2.10}$$

Chapter 3

Elucidation of Microsolvation Environments via systematic sampling of cluster surfaces

3.1 Introduction

The determination of minimum energy molecular geometries of clusters for comparison to experimental vibrational spectra is generally a difficult task, owing largely to the vast number of orientational permutations that must be explored in systems with numerous accessible degrees of freedom. However, at room temperature, as has been shown for enzymes and proteins, the number of such energetically accessible structures may be manageably finite.[85] Considerable effort has been expended more recently to determine methods for their elucidation that are both accurate and efficient.[15] One of the most common protocols to determine such cluster orientations involves sampling a significant number of possible orientations and comparing their relative energies, most commonly via Monte Carlo (MC) algorithms. These algorithms employ a global optimization routine to identify a series of local minimum energy geometries on the potential energy surface (PES) of the cluster.[86,87] They also apply purely random distortions to a cluster geometry in the search for lower energy cluster configurations and ideally the global minimum conformation. Basin Hopping (BH) builds on MC algorithms using an iterative approach with acceptance and rejection criteria to guide random distortions of a cluster to map the PES in a sequential fashion.[15,88,89] Subsequent steps of a BH routine are steered towards lower energy conformations, which is often thought of as a guided walk along the PES. Both MC and BH techniques have demonstrated an ability to map the PES successfully and to produce credible candidate cluster geometries. However, both techniques suffer from the time required to probe all possible orientations in order to ensure that all important local and global minima are found. Therefore, a technique that bypasses this requirement to sample all possible orientations to map the PES would significantly improve the efficiency in which local and global minima are determined.

Advances in parallel processing allow for the mapping of the physical surface of a pre-existing cluster geometry in place of traditional PES mapping. Such a protocol would remove the dependence on subsequent PES searches as a result of the systematic placement of clusters in predetermined orientations. This simultaneous determination of energies for cluster geometries then allows for multiple computer core processing, known as multi-threading. This is significantly more efficient than MC and BH algorithms, which examine an indeterminate number of indistinct cluster geometries, whereas this process examines a finite number of predetermined distinct cluster orientations. Thus, the systematic sampling of cluster surfaces (SSCS) algorithm was designed to implement new techniques to explore configurations of molecular and microsolvated species, which are of interest in numerous facets of gas phase ion chemistry.[90–93] Algorithm efficiency and accuracy have also been evaluated on numerous systems, which is the focus of the new protocol described herein.

3.2 Methods

The focus when designing this algorithm was to examine organic and metal complexes commonly found in experimental mass and vibrational spectra. To probe candidate cluster orientations more efficiently, the physical surface of the cluster is evaluated through a new protocol designated as the SSCS algorithm. The procedure of the algorithm is found in **Figure 3.1**, wherein the surface of a core molecule or cluster is investigated using a tandem Coloumb pairwise and universal force field (UFF)[94] energy evaluation. Following this evaluation, candidate geometries are sorted and optimized before evaluation by cosine similarities to determine unique geometries.

This procedure identifies areas for cluster growth by examining the surface charges of atoms. An assumption is made that atoms with close to zero partial charge will show little to no potential for interaction when selecting areas for cluster growth. The partial charge of atoms identifies pockets of positive and negative charge along the surface of the core cluster which are favourable cites for cluster growth. These partial charges are determined prior to analysis using a ChelpG[95] partition scheme and ported into the SSCS workflow.

Intermolecular interactions within clusters are determined by generating a sphere of points with a 10 Å radius about the centre of mass of the primary species, generated using Lebedev quadra-

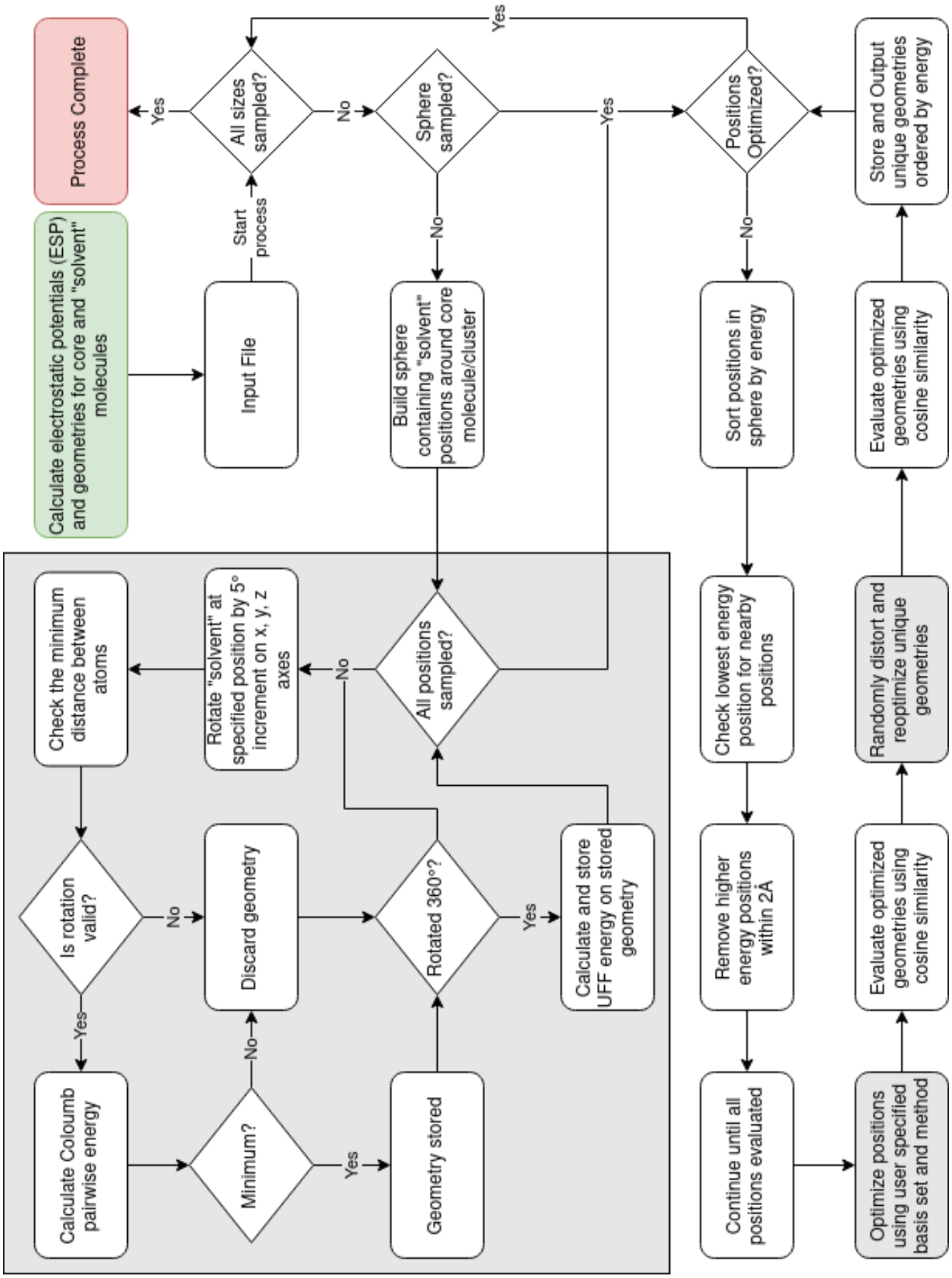

Figure 3.1: The general procedure of the SSCS algorithm. The start and end of the procedure are highlight in green and red respectively. Any part of the algorithm that is multi-threaded has been highlighted using a grey background. A number of steps have been simplified and are explained in greater detail following this figure.

ture.[96] Each point in this sphere represents a position where a molecule in the cluster is placed in sampling the interaction potential with the core molecule. Points are then "pruned" from the sphere if their distance to a partial charge centre is greater than 4.0 Å. Beyond this distance, intermolecular interactions, especially hydrogen bonding, will be sufficiently weak, that inclusion of points beyond this distance is unnecessary as they add no additional insight into the energetics of a cluster structure.[97] The partial charge centres are determined by examining the system for the most significantly charged atoms and excluding those that are not within 10% of the minima and maxima. An example of a pruned sphere containing 284 points is shown in **Figure 3.2**.

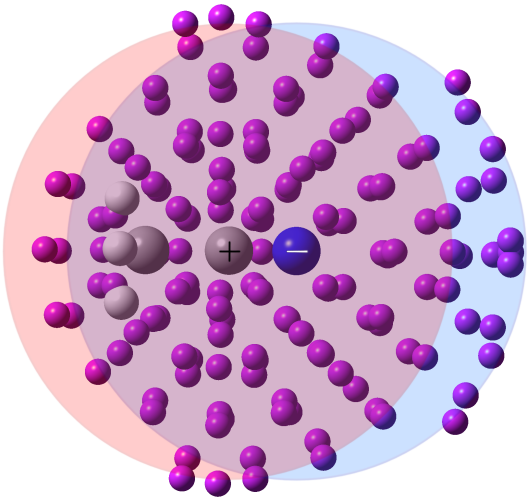

Figure 3.2: An example of a sphere generated for an acetonitrile molecule with an initial radius of 10.0 Å. Each purple dot represents a possible location for the positioning of a cluster molecule. The points in the sphere correspond to a distance of 4.0 Å to either the most negatively (blue) or most positively (red) charged atoms in the acetonitrile.

The energy of each individual point in the sphere can be evaluated using a Coulombic (C) description of intermolecular interactions. This energy is determined by placing the 'solvent' molecule of the cluster at each point. As an example, consider the serial solvation of an acetonitrile molecule as shown in **Figure 3.2**. An acetonitrile molecule is placed at each point in the grid to create an acetonitrile dimer. The second acetonitrile species is then rotated in space about its x, y and z principle axes until the lowest energy is determined as defined in Equation (3.1).

$$Energy = \frac{q_i q_j}{R_{ij}} \tag{3.1}$$

In equation (3.1), the q terms represent the partial charge at each atom and the R_{ij} term

represents the distance between atoms. Through benchmarking, it was found that only atoms with a large negative or positive partial charge had a dramatic effect on orientation. As such, a cut-off was introduced to examine the atoms in the system that were within 25 % of either the minimum or maximum partial charge. R_{IJ} is limited by a default value of 0.70 Å, being sufficiently smaller than the shortest covalent bond length found experimentally of 0.74 Å.[98] The cluster geometry being evaluated is discarded should any interaction be shorter than the minimum R_{IJ} value specified.

Once the lowest energy rotation is found, a secondary evaluation using a modified UFF calculation is performed that accounts for intramolecular and intermolecular energy terms as defined in Equation (3.2).

$$E_{total} = \sum_{bonds} K_r(r - r_{eq})^2 + \sum_{angles} K_\theta(\theta - \theta_{eq})^2 + \sum_{dihedrals} \frac{V_n}{2}[1 + \cos(n\theta - \gamma)] + \sum_{i<j}[\frac{A_{ij}}{R_{ij}^{12}} - \frac{B_{ij}}{R_{ij}^{6}} + \frac{q_i q_j}{\in R_{ij}}] \quad (3.2)$$

The UFF protocol is composed of both bonding and non-bonding contributions where the bonding interactions involve optimization of bond distances, angles and dihedrals and the non-bonding interactions are based on C and van der Waals (VdW) interactions.

This process of calculating the energy at each position is then repeated until all 284 points in **Figure 3.2** have been sampled. These points are then sorted by energy and, with a threshold energy criterion imposed, unique areas of low energy are determined. The geometries at the surviving points are then optimized at a user specified level of theory to provide the individual local minimum geometries.

Unique geometries from optimization steps are identified using two similarity functions. The first evaluation examines mass weighted cosine similarities[15,99,100], where the Euclidean distance ($\vec{R}$) between the centre of mass ($\vec{R}_{COM}$) and each atom position ($\vec{r}$) is evaluated and multiplied by the respective atom mass, as shown in Equation (3.3).

$$R_i = m_i |\vec{r}_i - \vec{R}_{COM}| \quad (3.3)$$

After determining $\vec{R}_i$ for all atoms in a geometry ($\vec{R_A}$), a comparison to other geometries ($\vec{R_B}$) can be done to determine their cosine similarity (d($\vec{R_A}, \vec{R_B}$)), as shown in Equation (3.4).

$$d(\vec{R}_A,\vec{R}_B) = \frac{cos^{-1}\left(\frac{\vec{R}_A \cdot \vec{R}_B}{|\vec{R}_A||\vec{R}_B|}\right)}{\pi} \tag{3.4}$$

The second evaluation compares the Euclidean distances (D) of each atom to atom distance, where a vector ($\vec{r}$) represents an atom position, as shown in Equation (3.5).

$$D_{ij} = |\vec{r}_i - \vec{r}_j| \tag{3.5}$$

After determining D_{ij} for all atoms in a geometry (D_A), a comparison to other geometries (D_B) can be done to determine their similarity ($d(D_A, D_B)$), as shown in Equation (3.6).

$$d(D_A,D_B) = \sum i,j>i \, |D_{A,ij} - D_{B,ij}| \tag{3.6}$$

Before comparing cosine similarities, $\vec{R}$ is sorted by smallest to largest distance from the centre to allow for a comparison of low symmetry species. Due to the nature of this comparison, it will fail to distinguish highly symmetrical species[15], such as square planar and tetrahedral spcies, in which case the second evaluation is used as a sanity check. This allows for the pruning of candidate geometries based on a threshold of similarity, while considering both low and high symmetry species.

These candidate geometries are further refined by a random distortion step to capture alternative configurations of each identified minimum. Each component in a cluster is randomly translated by $\pm$ 2.0 Å in increments of 0.25 Å and then rotated to the lowest energy orientations using Equation (3.1). These modified cluster orientations are sampled using UFF; the lowest energy orientations are then optimized and evaluated to determine if new minima have been found.

The UFF forcefield employed contains modifications that favour traditional cluster growth mechanisms and rearrangement of these species to form highly ordered geometric cages. To achieve this, the base equations found in the open-source Babel chemical toolkit were used as reference.[101] Conventional UFF calculations do not usually include C interactions because their parameters are determined without partial charges.[94] However, their inclusion is essential to elu-

cidate hydrogen bonded cluster geometries, as found through benchmarking systems. Scaling factors applied to the VdW and C contributions were arrived at through rigorous testing using both neutral and protonated methanol clusters containing four to nine molecules as seen in the results section. After evaluating all rotations using this modified UFF code, the lowest energy rotations are compared and stored to determine areas of low energy minima in the sampling sphere.

When evaluating clusters containing more than two molecules, subsequent analyses are performed to establish the interactions between pairs of molecules in the cluster. This is shown for the acetonitrile dimer in **Figure 3.3**, where an acetonitrile 'solvent' molecule is interacting with the 'core' acetonitrile molecule. An additional sphere has been generated around the second acetonitrile molecule. This is done to survey the interaction potential of molecules with the core 'cluster'.

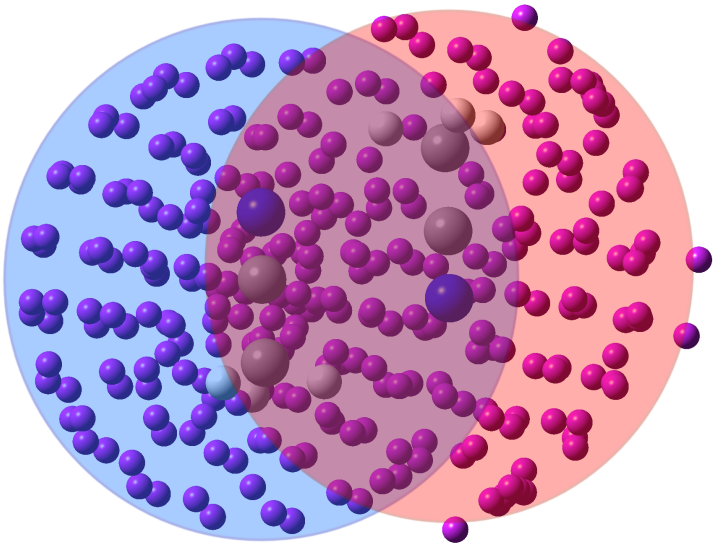

Figure 3.3: An example of the 4 Å spheres generated for two acetonitrile molecules. The blue sphere represents the initial pruned acetonitrile sphere, while the red sphere represents the sphere generated for the second acetonitrile molecule.

This methodology of subsequently building solvation spheres allows the algorithm to explore mixed solvent systems. This only requires building the ensuing spheres such that all orders of addition are considered. For example, one could envision a common electrospray ionisation (ESI) solvent solution of 50:50 water and methanol. When the solution interacts with the core molecule there is nothing controlling which solvent molecule is the first to interact. This results in a dynamic solvation environment where numerous H_2O and MeOH constructs interact in

no determinate order with the core species meaning no static solvent core is observed. Hence, the need arises to create multiple processes to examine the build up of these unique solvent systems. Such a system containing these two solvent molecules for the SSCS algorithm would therefore examine the following processes: Core·$[MeOH]_2$, Core·H_2O·MeOH, Core·MeOH·H_2O, Core·$[H_2O]_2$. This ensures that core-solvent interactions are not missed by the addition of molecules in an arbitrary order.

3.3 Benchmarking

3.3.1 Determination of Optimal Energy Sampling Methods

Throughout the development of SSCS, one problem which was continually present was the accuracy of single point energies for positions in the spheres. This was an extremely important issue as the positioning of groups around the core molecule hinged on these energies. As mentioned in the Methods section, the solution to this problem was to include scaling factors to the UFF method in order to more accurately predict cluster orientations. This solution was a requirement because of the lag-time in calling other computational packages. Other packages were found to have limitations of two to sixteen calls per second. This meant that both software suites were limited to calculating approximately a maximum of 30 single points per second when utilizing a semi-empirical technique. For example, in a relatively small system (21 atoms) containing 100,000 sphere positions or 3,700,000 calculations it would take approximately 27 hours to sample all positions, with runtimes scaling poorly with cluster size increasing to 33 hours for relatively large systems (83 atoms). Thus, a new method for sphere sampling was required.

Testing various methods illustrated that the molecular mechanics methods would be the quickest but would have very poor accuracy. When the UFF method was initially tested it showed strong disagreement with other algorithms that searched the PES of clusters. Additionally, it was only approximately two and a half times faster than semi-empirical methods while showing significantly poorer results. However, when examining equation (3.2) for UFF, as previously mentioned in the Methods section, it was determined that the C term was not being utilized in conventional calculations.

Upon inclusion of this C term, it was found that UFF showed good agreement with the

semi-empirical method while maintaining its relative speed increase, showing the importance of including both terms accounting for inter-molecular interactions. It was then established that, to fully utilize the electrostatic portion, the method would have to be rewritten in order to control scaling factors for the UFF method.

The method was rewritten in a Python library and the final result was found to be approximately 23 times faster than that of calculations found in other computational suites. On average, a Python calculation was found to have taken 8.6 ms whereas other computational suites were found to take approximately 200 ms. Python was also able to apply all available resources when determining energies, removing the limitation of 16 active processes at a time. Another factor that further improved the speed of the method was the removal of intramolecular interactions. These interactions were consistent in each orientation and thus the energy of the bonds, angles, and dihedrals did not change. When these interactions were removed the calculation dropped to approximately 3.6 ms on average, making it 55 times faster than other computational suites. Incorporation of the new method can be seen in **Table 3.1** where the dramatic increase in speed can be observed. Runtimes were determined by dividing 3,700,000 by the respective calculations per second which were 5 per second for other computational suites, 116 per second for Python using all interactions, and 278 per second for only inter-molecular interactions, with each value multiplied by the number of CPUs used.

Table 3.1: Comparisons of UFF runtimes for sampling 100,000 sphere positions for a system containing 30 atoms.

Method	CPUs	Time
Other Suites	16	13h
Python (all-interactions)	16	33m
Python (all-interactions)	64	8m
Python (inter-molecular)	16	14m
Python (inter-molecular)	64	4m

While Python is slower than other coding languages, such as C/C++ or fortran, for large mathematical problems, the simplicity of the calculations performed found minimal speed improvement while greatly hampering the ease of use and installation of the algorithm for the end user. A potential speed increase would be to incorporate C/C++ through ctypes bindings into the algorithm to manage calculations resulting in faster calculations while maintaining

ease of use and installation.

3.3.2 Determination of Optimal Optimization Methods

For every solvent molecule added to a system the number of candidate geometries increases due to an increase in the degrees of freedom. Thus, an attempt was made to increase the speed of the optimization routine by examining different methods found in the semi-empirical method. The MNDO, AM1, PM3, and PM7 methods were evaluated for their speeds and accuracies. The Grimme's 3-correct Hatree-Fock method (HF-3c) method was also evaluated as it corrects for dispersion and short-range basis incompleteness, while also being relatively fast. PM7 was selected as the reference due to its ability to reproduce density functional theory (DFT) geometries fairly accurately, as found in work previously carried out in the literature.[102–105] To evaluate the methods, a system containing the deprotonated carboxylate para-hydroxybenzoic acid (PHBA) tautomer, as shown in Chapter 4, with two waters was examined using 11 different water orientations. The optimized geometries were evaluated by comparing the Euclidean distances of each geometry. The distance similarity is the average difference when compared against the PM7 optimized geometry. The averaged results can be seen in **Table 3.2**.

Table 3.2: A comparison of the optimized geometries of semi-empirical methods and the HF-3c method.

Basis Set	Optimized Structure Similarity	Time
PM7	100.00	52 seconds
MNDO	87.03	2 minutes 21 seconds
AM1	95.47	59 seconds
PM3	97.59	1 minute 27 seconds
HF-3c	99.5	12 minutes 32 seconds

As seen in **Table 3.2** none of the other methods were as accurate nor as fast as those seen by PM7. While the structures produced by HF-3c were more accurate than PM7 when compared to pure solvent clusters, they took 12 times longer, and when optimized at the next level of theory both converged to identical structures. This, unfortunately, meant that no speed improvements could be made regarding the optimization portion of the SSCS algorithm. However, it should be noted that HF-3c did not produce systematic error when examining polygonal systems or those containing numerous hydrogen bonds, as touched on when examining clusters of neutral and protonated methanol.

3.3.3 Variability in Sphere Positions

It is important to note the way in which clusters are interrogated using this method. For a system such as that described in **Figure 3.2** with 226 possible positions for a cluster, the number of possible configurations is given by (3.7).

$$x = \frac{n!}{r!(n-r)!} \tag{3.7}$$

For n possible positions and r solvent molecules, if n=226 and r =1 there are 226 configurations for the first water molecule addition. However, simply expanding the system to three water molecules results in 1,898,400 configurations. In this example, using eight processing cores, it took the algorithm seven seconds to determine the energies for the 226 possible configurations, while expanding this to the random configurations for three water molecules would require sixteen hours to sample the entire system. However, using the method in which clusters are subsequently built off of one another, **Figure 3.3**, reduces this time to one minute and nineteen seconds given that there are now only 2664 positions to evaluate.

Another consideration for the algorithm was the ability to examine multiple solvents in the same system. To examine all possible orientations, the algorithm must examine the build up of the system using each solvent as a starting point. The construction of such a system is best illustrated in **Table 3.3**, where the beginning steps can be observed for the construction of a system containing five water molecules and five methanol molecules around a core molecule. Initially, H_2O (A) or MeOH (B), will be added to the core molecule and evaluated in individual runs of the SSCS algorithm. Upon the second addition the algorithm will split into four separate processes to manage the four possible additions to the core molecule. Separation of these processes continues until all solvent molecules have been added.

Table 3.3: Sample construction of a system containing both water (A) and methanol (B) solvent molecules. As the system grows in size cluster types are binned to reduce post-processing. Processes containing the same solvents, such as AB and BA, are binned, such that identical core-solvent conformations are not sampled multiple times.

Additions	Water Process	Methanol Process	Binned Processes
First	A	B	A,B
Second	AA,AB	BB,BA	AA,AB,BB
Third	AAA,AAB,ABA,ABB	BBB,BBA,BAB,BAA	AAA,AAB,ABB,BBB

When a solvent molecule is added in the H_2O process it is entirely possible that cluster arrangement has already been sampled in the MeOH process and vice versa. Referring again to the deprotonated PHBA system seen in Chapter 4, there are two possible sites for solvent interaction, being either the phenoxide or carboxylate. When water is first added it will interact with either site, for example it may interact with the carboxylate (C_{H2O}). That then suggests that when a methanol is added it will interact with the water ($C_{H2O\cdots MeOH}$) or phenoxide site (C_{H2O}, P_{MeOH}). Shifting back to the methanol process, the first methanol may be added to the phenoxide site (P_{MeOH}), addition of the water molecule would then see interaction with either the methanol ($P_{MeOH\cdots H2O}$) or the carboxylate (C_{H2O}, P_{MeOH}). Thus, it can be observed that both processes contain (C_{H2O}, P_{MeOH}), showing the need to bin the processes to prevent sampling the same conformation multiple times.

Another reason that binned processes are important is for ease of analysis by the end user. With each addition (a) of solvent, the number of permutations for each addition grows as a factor of the number of solvents (n): $p = a^n$. Looking at a simple two solvent model, with each increase in a, p doubles, having 252 possible additions when a = 10. However, there is only one binned process, this is a result of creating binned processes as the systems grows in size. When a = 6, there are no longer any pure solvent clusters, as in AAAAA or BBBBB for n = 5, there now exists only mixed solvent clusters (AAAAAB/BBBBBA). These mixed solvent types would then be binned with combinations such as ABAAAA, AABAAA, etc, resulting in fewer binned processes for n = 6 than n = 5. When looking at a system of n = 9, there exist two possible processes, either AAAAABBBB or BBBBBAAAA. The number of permutations and possible binned process combinations is shown in **Table 3.4**, to help illustrate the number of permutations and combinations per addition.

Table 3.4: Total number of possible permutations and combinations for a system containing five water molecules and five methanol molecules.

Additions	Permutations	Combinations
First	2	2
Second	4	3
Third	8	4
Fourth	16	5
Fifth	32	6
Sixth	62	5
Seventh	112	4
Eighth	182	3
Ninth	252	2
Tenth	252	1

3.3.4 Determination of Scaling Factors

The efficacy of the SSCS algorithm was evaluated using neutral and protonated clusters of water and methanol, for which a plethora of experimental and computational data exist.[16,17,106–110] Using this data, the accuracy of the algorithm was improved by applying scaling factors to the intermolecular terms found in the UFF equation, as shown in Equation (3.8).

$$E_{total} = \sum_{intramolcular} + \sum_{i<j} [(\frac{A_{ij}}{R_{ij}^{12}} - \frac{B_{ij}}{R_{ij}^{6}}) * X + (\frac{q_i q_j}{\in R_{ij}}) * Y] \tag{3.8}$$

To evaluate these scaling factors, a sub-routine of the SSCS algorithm was employed to examine modifications on specific cluster orientations of size = 4 - 9 of protonated methanol clusters. This was done to remove any potential run-to-run variability in clusters of size = n, such that each set of factors examined identical geometries for each cluster size. These clusters were examined due to the simplicity of the hydrogen bonding networks, especially those assuming linear and polygonal shapes. Thus, to simplify this process, clusters were examined using the global minimum geometry at size = n for each shape found in the literature.[111] Using the optimized DFT geometries at each cluster size, each molecule in the cluster was randomly rotated and translated, and then the energy and geometry of the isomer were compared back to the initial DFT structure. This process was repeated 25,000 times for each polygon in an attempt to ensure each run sampled identical isomers. Only isomers that were within 150 kJ mol^{-1} of the minimum were considered for similarity analysis in order to eliminate structures that would be pruned by the energy thresh-

old in the algorithm. The energy threshold was selected based on repeated runs until sufficient accuracy to DFT was achieved, while limiting the number of isomers to be examined.

Initially, the influence of each factor was examined by setting the other variable to zero and determining the similarity to the DFT minima structures. This was done using the similarity functions outlined in the methods. To ensure that the analyses were not subject to variations the process was carried out ten times and averaged to minimize run-to-run variation, with results summarized as a plot as seen in **Figure 3.4**.

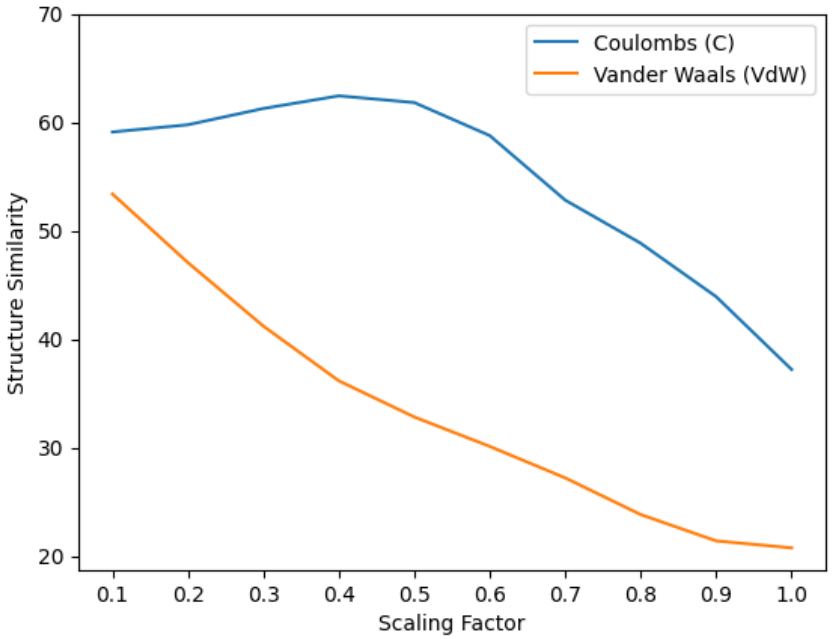

Figure 3.4: Analysing the effect of variable scaling factors on cluster similarities for protonated methanol clusters of sizes n = 4 - 9, when setting the other factor to 0. This plot is the average of ten runs to minimize the effect run-to-run variations.

This comparison clearly illustrates that inclusion of the C factor has a larger impact than that of the conventional analysis using only the VdW factor. It was interesting to note that in both cases the accuracy of the lowest energy isomers decreased as each respective factor approached one. However, unlike VdW, C showed an increase in accuracy towards 0.4 before decreasing. These factors were then mixed to determine what combination resulted in the highest accuracy, as shown in **Figure 3.5**.

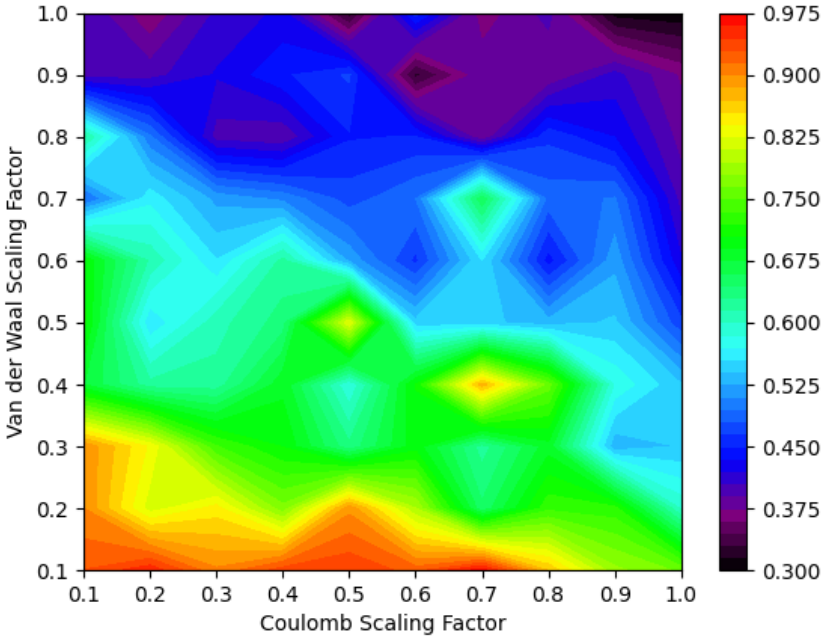

Figure 3.5: Analysing the effect of variable scaling factors on cluster similarities for protonated methanol clusters of sizes four to nine. The contour plot represents the average similarity for each cluster size at those specific scaling factors. It can be observed that any amount of VdW scaling results in reduced accuracy when compared to DFT.

One weakness encountered in these comparisons was the accuracy of polygonal species of both methanol cluster types when optimizing geometries using low levels of theory such as the PM7 method.[102] The PM7 method prefers non-planar structures, leading to an additive error as cluster geometries grow in size as seen in the methanol pentamer in **Figure 3.6**.

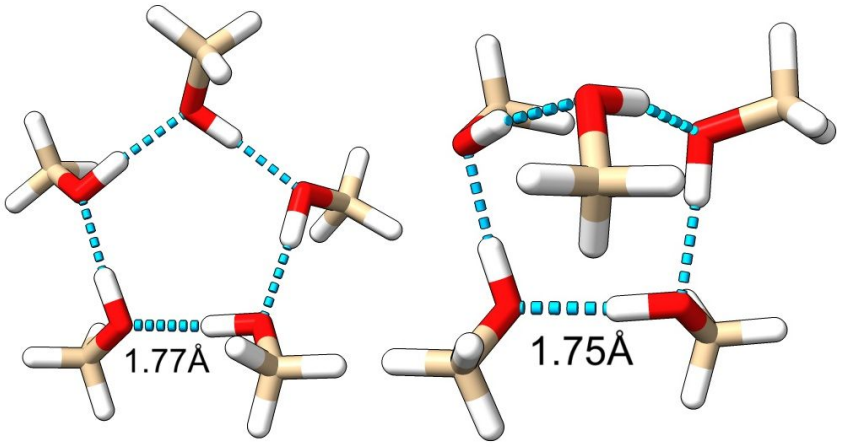

Figure 3.6: Global minimum pentamer methanol cluster from Kazachenko et al. found using B3LYP-D3 (left) and the SSCS algorithm global minimum found using pm7 (right).[111]

The additive error encountered using PM7 can be alleviated through the use of a higher level of theory. HF-3c from the ORCA computational suite and the traditional Hartree-Fock (HF) method were both found to reduce this error but at the cost of increased computational time.[112,113] A tradeoff exists between computational time and accuracy, as higher level methods took (on average) eight times longer in real-time relative to an SSCS run using PM7. Therefore, the importance of these planar structures should be considered on a case by case basis when running the SSCS method.

3.3.5 Algorithm Evaluation

Comparison of neutral and protonated MeOH clusters generated by the SSCS workflow to the literature[111,114–117] showed excellent agreement using the scaling factors found in **Figure 3.5**. The highest similarity to DFT structures was found when the VdW factor is set to 0.1 and the C factor is set to 0.7. As noted in **Figure 3.4**, the C factor without any amount of VdW scaling only amounts to approximately 62.5 % accuracy compared to 97.5 % when VdW is set to 0.1.

With optimized scaling factors determined from methanol solvent clusters, the validity of a system was verified with markedly different hydrogen bonding behaviour. The two donor two acceptor nature of water clusters allows for intricate cluster geometries, even for small cluster sizes. Application of the SSCS protocol yields nearly identical cluster orientations with those determined in the literature, as shown in **Figure 3.7**.[118–120] Structures were found using PM7 and determined minima in the same order for each cluster size, albeit with larger gaps in relative energy compared to that of the DFT minima structures from literature. All relevant structures were found to be within 20 kJ mol^{-1} of the computed global minimum structure.

Using the same scaling factors, the ability of SSCS to model protonated water clusters was evaluated. Analysis of the structures generated at higher levels of theory for protonated water clusters showed excellent agreement in addition to the elucidation of new low-lying energy structures in comparison to the literature.[121–123] Following the methodology employed by Likholyot et al., candidate geometries for four to seven water molecules were analysed and those clusters containing six or seven waters were found to possess new low energy conformations.[123] For $H_3O^+ \cdot (H_2O)_6$, a comparison to the previous lowest energy conformation found

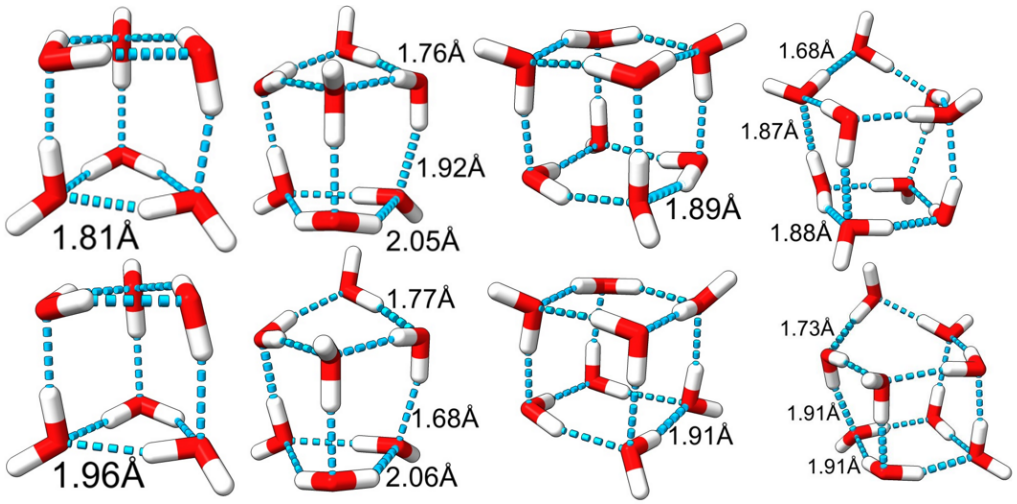

Figure 3.7: Lowest energy water clusters for six to nine molecules from Shields et al. (top) and the SSCS algorithm (bottom).[120]

in literature showed the new conformation to be 1.63 kJ mol^{-1} more favourable. Similarly, for $H_3O^+ \cdot (H_2O)_7$, a comparison to the previous lowest energy conformation in the literature showed the new conformation to be 13.24 kJ mol^{-1} more favourable. The SSCS isomers are shown in **Figure 3.8**. In addition to these new low energy conformations, several additional higher energy isomers were also identified for all cluster sizes.

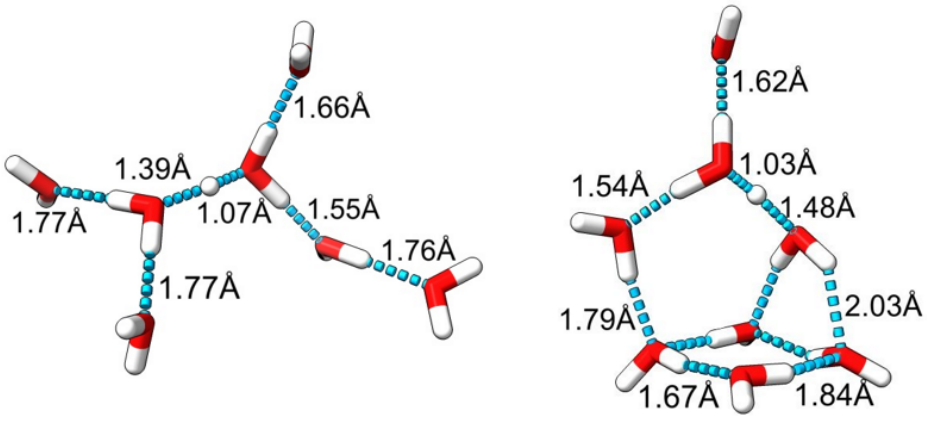

Figure 3.8: Lowest energy clusters for $H_3O^+ \cdot (H_2O)_6$ and $H_3O^+ \cdot (H_2O)_7$ found using the SSCS algorithm.

These simple solvent cases have shown the efficacy of the SSCS algorithm; however, more complex systems can be examined, containing ionic species or larger molecules. An example case is the cluster containing 19 water molecules with one hydronium ion of Yu and Bowman.[124] In that work, a many-body potential energy and dipole moment surface method was proposed that could accurately determine the binding energies, dynamics, and vibrational spectra of aqueous

clusters. The SSCS algorithm may thus prove useful in such a study in the determination of additional candidate orientations for analysis by their technique. However, larger molecular species are often the target of computational evaluations when examining cluster properties, for which SSCS would easily provide a significant advantage. Additionally, clusters that are composed of predominantly hydrogen bonding interactions should be treated with at least the HF level of theory to increase accuracy by removal of poorly organized hydrogen bonding networks.

3.4 Results and Discussion

3.4.1 Evaluating Solvated Structures of Protonated Glycine and β-Alanine

In order to demonstrate the power of the SSCS suite, water solvated species of protonated Glycine (Gly) and β-Alaine (β-Ala) were generated. Understanding the stability of the protonated species and their structural evolution in microsolvated environments may allow for an understanding of how these functions may be interrupted from normal function.[125–128] The generated species were directly compared to those found by Fischer et al. using the BH algorithm.[129] In this study, the objective was to determine the effect of solvation on the length of the intramolecular hydrogen bond in protonated Gly and β-Ala, which could be elucidated from the gas-phase infrared predissociation (IRPD) spectra as detailed in a previous publication by the group.[130]

To fully evaluate the cluster surface, four input structures were generated for each species with the objective to examine the effect of dihedral rotation about the carboxylic acid moiety. Dihedral rotation in 60° increments was found to be sufficient to sample the cluster's surface. The eight runs were conducted at the HF/3-21g level of theory, which was found to be efficient for cluster growth mechanisms driven by hydrogen bonding. Following the methodology used by Fischer et al. for post analysis of candidate geometries, it was found that the SSCS algorithm elucidated global minimum structures for both protonated amino acids identical to those from the BH algorithm.[129] Additional isomers were not identified for Gly clusters but a new candidate was identified for β-Ala with five water molecules. The newly identified isomer, β-V-SSCS, shown in **Figure 3.9** was 1.67 kJ mol^{-1} higher in energy than the global minimum structure. β-V-SSCS showed agreement with a weak water feature found at 3222 cm^{-1} in the

experimental spectrum. This mode was absent from the two previously identified isomers when probing the system with N_2 seeded with H_2O or D_2O to examine solvent spectral features, since the mode for that peak in isomer D, as shown in **Figure 3.9**, is the result of an N-H stretch from the ion core.[129] The correlation of this mode with the experimental spectrum suggests this isomer is present in the probed gas-phase ensemble. However, a population analysis employed by Fischer et al. found this structure to be relatively insignificant, but nonetheless highlights the ability for the SSCS to accurately map the surface of positively charged species.[129]

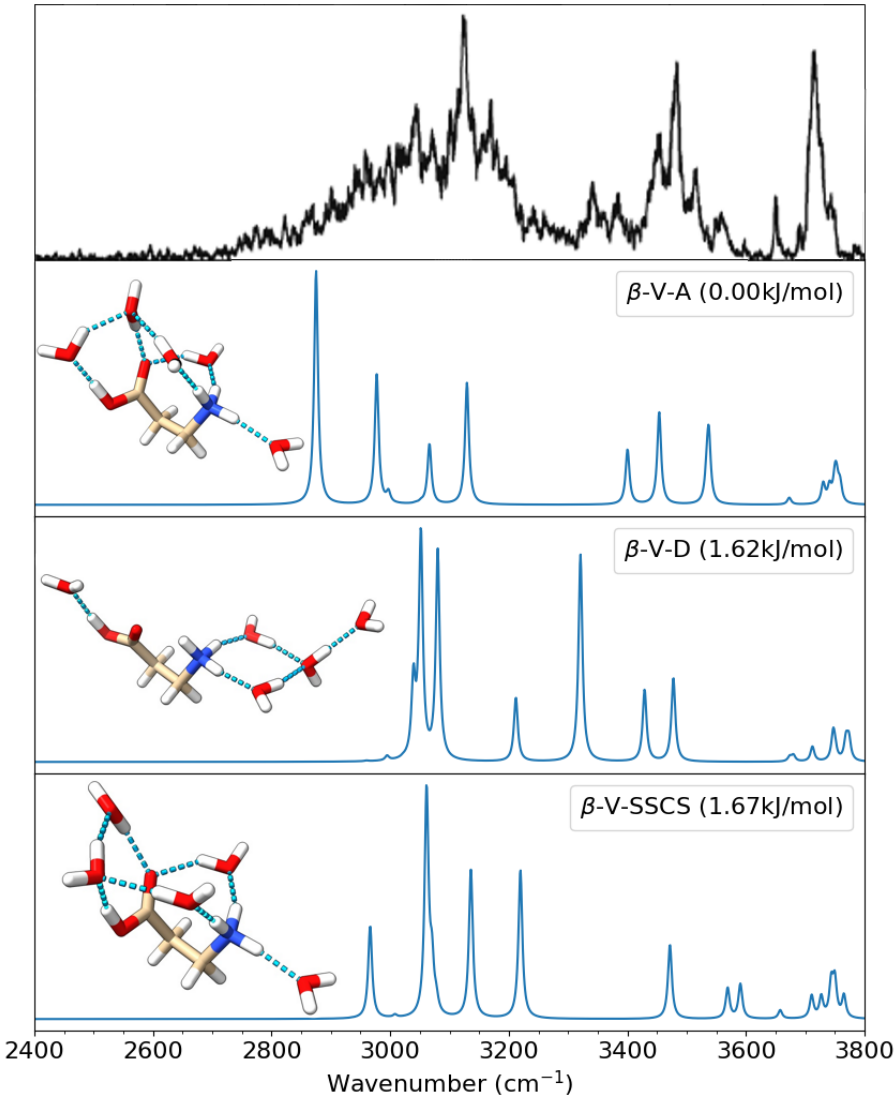

Figure 3.9: Lowest energy clusters for β-alanine with five water molecules found by Fischer et al. and SSCS.[129] The experimental infrared predissociation spectrum (black) was obtained by Fischer et al. using a home-built dual-trap cryogenic ion mass spectrometer.[129] The energies provided are relative energies calculated at the MP2/def2TZVP level of theory with Grimme Dispersion 3 with Becke-Johnson damping (GD3BJ) and counterpoise corrections.

3.4.2 Anionic Tryptophan Chloride Complexes

The SSCS algorithm also excels in the investigation of anionic clusters, such as the investigation of biologically relevant tryptophan (Trp) complexes by Ieritano et al.[131] In this study, the PES of $[Trp_n]^-$ and $[Trp_n\cdots Cl]^-$ were sampled using the BH algorithm. These species are ideal candidates for examination via the physical surface of the Trp rather than that of the PES, since the interaction potential of the Trp core is localized at the backbone amine and carboxylate/carboxylic acid, as well as the indole side chain.

A direct comparison to the $[Trp_n\cdots Cl]^-$ monomer and dimer species was carried out to test the ability of SSCS to investigate negatively charged species. The monomer system was first examined by rotating the dihedral angle between the α and β carbons of the backbone in increments of 120° and the carboxlic acid by 180°. This generated a total of six input structures to be clustered with the chloride anion, taking one to three minutes to sample each surface using eight processing cores and PM7. Post analysis of the output structures generated found an identical global minimum structure to that of the BH algorithm, shown in **Figure 3.10**, as well as eleven other low-lying isomers.

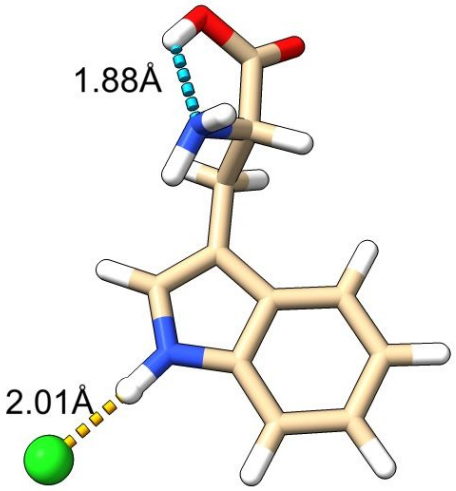

Figure 3.10: Lowest energy cluster for a tryptophan complexed with a chloride anion found by Ieritano et al. and the SSCS algorithm.[131] O-H and N-H bonds are highlighted in blue and Cl-H bonds are highlighted in yellow.

Examination of the dimeric species was carried out by combining the twelve isomers for $[Trp_n\cdots Cl]^-$ with the six bare Trp isomers. This was done by specifying one of the twelve

isomers as the primary molecule and the six bare Trp isomers as secondary molecules. The algorithm would then examine the combination of one primary and one secondary molecule until all secondary molecules had been examined. Each combination took nine to fourteen minutes to sample using eight processing cores and PM7, for a total of approximately one hour in real-time per primary molecule. Post analysis of the output structures revealed an identical global minimum structure to that of the BH algorithm, shown in **Figure 3.11**, as well as an additional low-lying isomer ($\sim$ 14.34 kJ mol^{-1}).

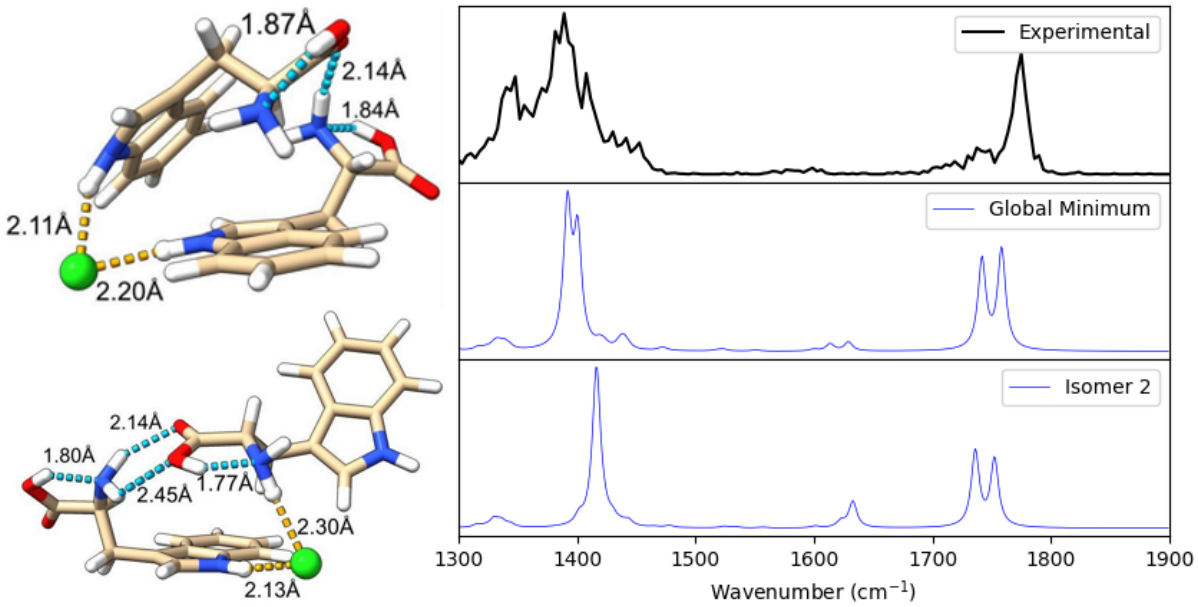

Figure 3.11: Global minimum cluster (top) with new 14.34 kJ mol^{-1} candidate cluster (bottom). O-H and N-H bonds are highlighted in blue and Cl-H bonds are highlighted in yellow. Comparison to experimental spectrum obtained by Ieritano et al. shows excellent agreement for isomer 2.[131]

It was surprising to see the significant improvement in speed between the two algorithms. For the monomer system, a 32-fold improvement in speed with the SSCS algorithm was observed compared to the BH algorithm; the SSCS process took a mere 30 minutes of real-time to complete. For the dimer system, SSCS took a total of twelve hours of real-time, which was a dramatic improvement over the BH method, which required about four days to complete. Another important improvement was the reduction in candidate geometries identified by each algorithm. Ieritano et al. documented that they had identified 500 candidates for post analysis study using BH[131], whereas SSCS produced a total of 21 isomers for the monomer, six of which were duplicates and immediately removed. This analysis highlights the ability of SSCS to examine small

biological systems as well as negatively charged species in a fast and efficient manner.

3.4.3 Shortfalls of the SSCS Workflow

While the SSCS workflow has demonstrated an excellent ability to elucidate cluster geometries, there are ultimately some shortfalls to the technique. In systems containing a significant number of dihedral rotations, there exists a nearly infinite number of dihedral configurations. In cases such as these, the SSCS workflow is not efficacious as it would take an infinite amount of time to map the surface of such a cluster. However, SSCS can be run on predetermined local minima of a core cluster to accelerate cluster discovery.

Another pitfall of the SSCS workflow is the difficulty that arises in exploring conformations of large clusters. This caveat is one which affects all algorithms, since the number of possible isomers increases exponentially with the degrees of freedom of the system. Through the various analyses presented here it has been found that the workflow slows considerably as the workflow approached 10 microsolvated species. However, this slow down is highly dependent upon the core molecule, the threshold for similarity, and the method being used to optimize candidate geometries.

To remedy these shortfalls, a joint project with the authors of the BH algorithm is being explored to accelerate the process scanning the PES. The ideal result of this collaboration would be exploration of the PES to find the local minimum energy orientations and surface scanning the minima to quickly explore the wells of the PES surrounding the minima structures.

3.5 Conclusion

Factors and parameters used by the SSCS algorithm were rigorously tested through several replicate runs using 100,000 distorted geometries of protonated methanol clusters. These factors saw a resulting similarity of 97 % compared to DFT optimized geometries, significantly reducing the time required for post analysis optimizations. The validity of these factors was then tested using neutral and protonated clusters of water and methanol, which yielded identical cluster orientations to those found in literature.

Through the analysis of various cluster types, the efficacy of the SSCS algorithm has been

established. Post analysis in all systems were successful in producing global minimum structures found using other techniques while significantly reducing the time required to search for these minima by approximately an order of magnitude in most cases. Not only was the overall time to identify structures reduced, the number of candidate isomers for post analysis was also significantly reduced. Literature for BH commonly reports selecting the lowest 300-500 energy isomers for analysis[15,89,131], potentially missing structures outside of this range that optimize to minima at higher levels of theory, whereas SSCS commonly produced 10-150 candidate isomers in total for post analysis in these tests. Thus, improvements presented here allow for ease of use by reduction in run-times and the elimination of guess work in the selection of isomers, while maintaining the same level of accuracy as other algorithms.

Chapter 4

An Examination of deprotonated p-Hydroxybenzoic Acid Clusters in the gas phase

4.1 Introduction

Para-hydroxybenzoic acid (PHBA) has been studied numerous times to determine the site of deprotonation in gas and liquid phases.[23–26,132–134] From previous studies utilizing proton-transfer reactions in ion cyclotron resonance (ICR) mass spectrometry and electrospray ionisation (ESI) mass spectrometry it has been found that the phenoxide is the preferred gas phase site while the carboxylate is the preferred solution phase site.[132–134] Additionally, in the gas phase the solvent used was found to play a role in tautomer preference, with aprotic solvents showing a preference for phenoxide and protic solvents showing a preference for carboxylate.[23–26]

In 1976, McMahon and coworkers explained that the reasoning behind this preference of monosubstituted benzoic acids in the gas phase can be explained by the localization of charge in each tautomer. The carboxylate has charge density localized about the carboxylate oxygens while the phenoxide has charge delocalized throughout the system.[133,135] Thus, the localization of charge in the carboxylate provides a more favourable situation for the formation of hydrogen bonding networks. This supports the notion that protic solvents in the gas phase favour carboxylate as they form 'solvent' conditions when compared to aprotic solvents.

Experimental research into the effects of solvent by Tian and Kass showed that they could easily undergo decarboxylation and hydrogen/deuterium exchange in aprotic solvents such as acetonitrile whereas in protic solvents such as methanol and water this was not observed.[23] Additionally, it was found that the concentration of the benzoic acid and the pH of solution was also found to have an effect on the preference of tautomer.[26]

To complement the experimental results, a theoretical study can be undertaken to illustrate the

solvation required, or lack thereof, for the transition of tautomers. It can be hypothesized that this disparity between results may be a result of experimental apparatus conditions, solvent conditions, or a combination of the two. An examination of ESI compatible solvents, such as methanol, ethanol, water, acetonitrile, and acetone, clustering with PHBA under 'gas phase' and 'liquid phase' conditions may yield insight into which phase is truly being sampled.

4.2 Methods

Gas phase conditions were simulated by examining clusters of PHBA tautomers with one to five solvent molecules. Solvent interactions were studied using the systematic sampling of cluster surfaces (SSCS) algorithm, interfaced with Gaussian 16 C.01, to produce initial candidate geometries.[95] This algorithm examines and sequentially builds a cluster system by determining interaction potentials on the cluster surface. In this case, the PHBA molecule is probed for interaction potentials by moving a solvent molecule to points in a 10Å sphere centred about the PHBA. The interaction potential is calculated using the partial charges of the molecules determined by the Merz-Singh-Kollmann partition scheme[136,137] calculated using the Modified Becke 97 exchange-dipole moment (ωB97X-D) method and 6-311++G(d,p) basis set.[55,138] The lowest energy candidates were then optimized using the semi-empirical PM7 functional.[102] After the optimization step a sphere of points for both the PHBA and the solvent are generated. This routine was then continued until all solvent molecules had been subsequently examined.

Unique structures identified by SSCS were then optimized at HF/6-31g and evaluated using mass weighted cosine similarities to eliminate analogous structures. Structures were then further optimized at the ωB97X-D/6-311++G(d,p) level of theory and evaluated using normal mode analysis. The ωB97X-D functional was selected as it was found to be one of the most accurate when compared to 200 other popular density functional theory (DFT) functionals.[52,55] Structure graphics were generated using the ChimeraX package.[139,140]

Solution phase conditions for each PHBA tautomer were simulated using the solvent cavity reaction field (SCRF). Solvents were selected via the Polarizable Continuum Model (PCM) and optimized at the ωB97X-D/6-311++G(d,p) level of theory.[141,142]

Both gas phase and solution phase clusters were evaluated using a population analysis of the

normal modes at temperatures of 300 - 700 K in 10 K increments at 1 atm. The population (ρ) of a cluster can be determined by examining the Gibbs energy of all isomers (k) at a certain temperature (T).[143] This process can be expanded to different sizes of a cluster (n) to examine how the number of solvent molecules can effect the relative populations of the two tautomers, see equation 4.1:

$$\rho_n^{(k)}(T) = \frac{exp(G_n^{(k)}(T) \cdot (RT)^{-1})}{\sum_k exp(G_n^{(k)}(T) \cdot (RT)^{-1})} \tag{4.1}$$

In this equation, R is the ideal gas constant and $G_n^{(k)}(T)$ is the Gibbs energy of the k^{th} isomer of the cluster containing n solvent molecules at temperature (T). The Gibbs energy can be evaluated at a given temperature by calculating the thermodynamic contribution of the translational, electronic, rotational, and vibrational motions.[58,95]

4.3 Results and Discussion

4.3.1 'Solution phase' studies of common ESI solvents

An examination of 'solution phase' simulations over a range of temperatures reveals that both protic and aprotic ESI solvents show no clear preference for PHBA tautomers, as seen in **Figure 4.1**. In both solvent types, there were cases of significant or weak preference for the 'solution phase' carboxylate tautomer under these 'solution' conditions. This suggests that rather than the type of solvent, protic or aprotic, being responsible, the solvent selected is the deciding factor behind the preference of the tautomer.

A range of temperatures were examined due to a number of studies using thermometer ions showing that altering the ESI cone voltage changed the effective temperature of ions en route to the ion trap.[144–146] This is important because no two experimental apparatus are identical and a variation in the cone voltage may be responsible for the preference of one tautomer over the other. It was found that for both solvent types, increasing the temperature increased the population of the phenoxide relative to the carboxylate.

Surprisingly, two commonly used ESI solvents, methanol and acetonitrile, displayed some of the

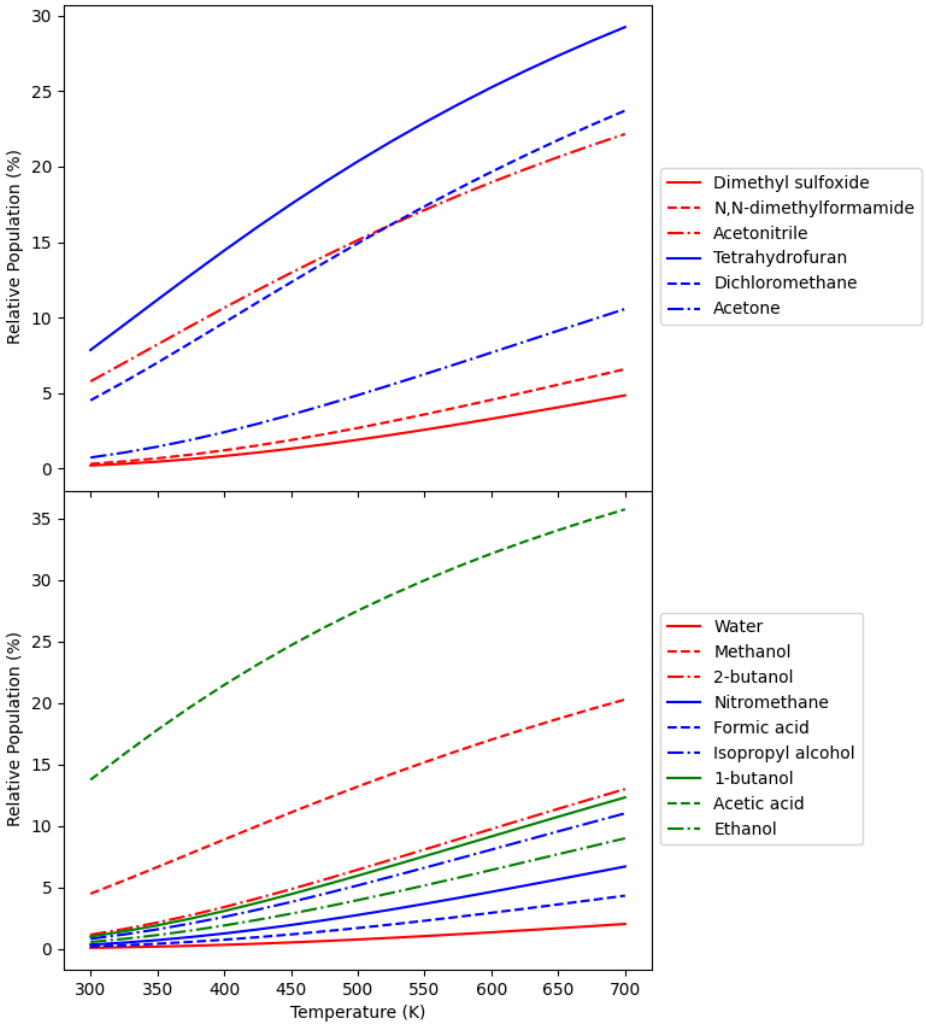

Figure 4.1: Relative population of the phenoxide tautomer under 'solution phase' conditions at varying temperatures.

weakest preference for the 'solution phase' carboxylate tautomer under these 'solution phase' simulations, as seen in **Figure 4.1**. This was surprising because methanol and acetonitrile are relatively small compared to the other protic and aprotic solvents, reducing steric effects. In turn, it was assumed there would be a benefit to forming strong hydrogen bonding networks for methanol, however this appears to have had the opposite effect. Similarly, it was assumed acetonitrile would form strong interactions as it possesses one of the strongest dipole moments of the aprotic solvents examined, as seen in **Table 4.1**. This is significant as methanol and acetonitrile are commonly mixed with other ESI solvents to increase spray efficiency. In the event that methanol and acetonitrile are mixed together, the user may experience one of the worst 'solution phase' spray conditions possible, yielding potential bias towards the 'gas

phase' tautomer. Both of these scenarios are exacerbated by the influence of the effective ion temperature experienced under ESI conditions.

Table 4.1: Dipole moments of aprotic solvents calculated at ωB97X-D\6-311++D(d,p).

Solvent	Dipole moment (D)
Tetrahydrofuran	1.81
Dichloromethane	1.91
Acetone	3.23
Acetonitrile	4.11
N,N-dimethylformamide	4.30
Dimethyl sulfoxide	4.50

4.3.2 Microsolvated geometries and energies of [PHBA]⁻ with protic and aprotic solvents

An examination of 'gas phase' simulations revealed that both protic and aprotic solvents show a strong preference for clustering towards the 'solution phase' tautomer, as seen in **Figure 4.2**. Initially, when completely isolated from solvent molecules, the Gibbs energy of the phenoxide is roughly 21.5 kJ/mol more favourable than the carboxylate tautomer. Addition of the first solvent molecule shows a significant shift to the relative populations towards the carboxylate tautomer. Subsequent additions show this trend increase with both solvent types showing preference for the carboxylate after the addition of the fifth solvent molecule at room temperature (298 K).

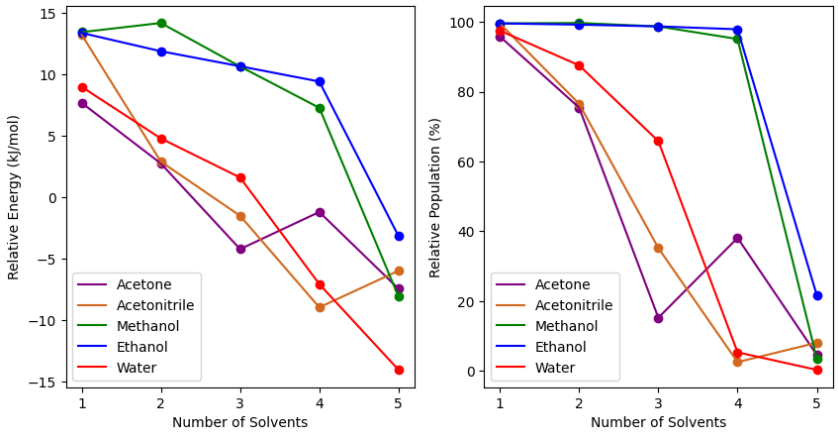

Figure 4.2: Relative Energies (left) and relative population (right) of the phenoxide tautomer in presence of a varying number of solvent molecules at 298 K.

As briefly touched upon in the 'solution phase' simulation, water displayed the strongest affinity for the carboxylate tautomer, followed by Dimethyl sulfoxide (DMSO); however, as seen in **Figure 4.2**, aprotic solvents initially display a stronger preference for the 'solution phase' tautomer. This behaviour is not unexpected if the binding motifs of the two solvent types are considered, as seen in **Figure 4.3**. The protic solvents were found to slowly build hydrogen bonding networks, slowly increasing the favourability of the carboxylate tautomer, while the aprotic solvents were found to have significant dipole interactions with the bare carboxylic acid of the carboxylate tautomer. Unsurprisingly then, as the clusters become more saturated, the impact of complex hydrogen bonding networks is more significant than dipole dipole interactions for influencing tautomer preference.

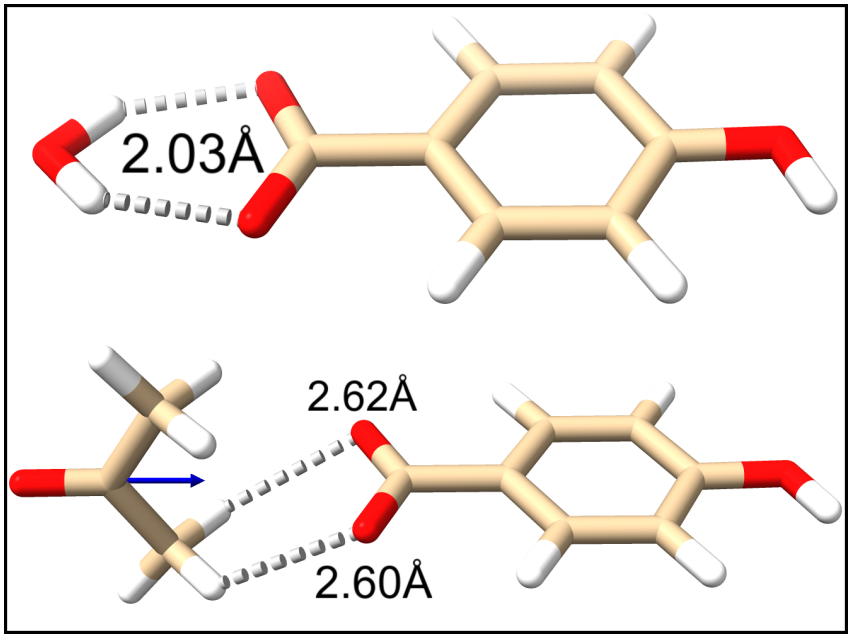

Figure 4.3: A comparison of water (top) and acetone (bottom) interactions with the carboxylate tautomer. The dipole moment of acetone is indicated by the blue arrow. The top two interactions for acetone were hidden to better illustrate the dipole moment.

The favourability of one tautomer over the other is best explained by examining the global minimum structures of each solvent. Beginning with the protic solvents, there is an initial distribution of solvent about the phenoxide charge site, as seen in **Figure 4.4**. Up to n = 3, solvent readily interacts with this site; however, as n increases the network becomes constrained, favouring conformations with more points of contact for hydrogen bonding with the PHBA tautomers. The bridging network of the carboxylate tautomer is observed for n = 3 but provides less points of interac-

tion with the charge site as compared to structures observed in the phenoxide tautomer.

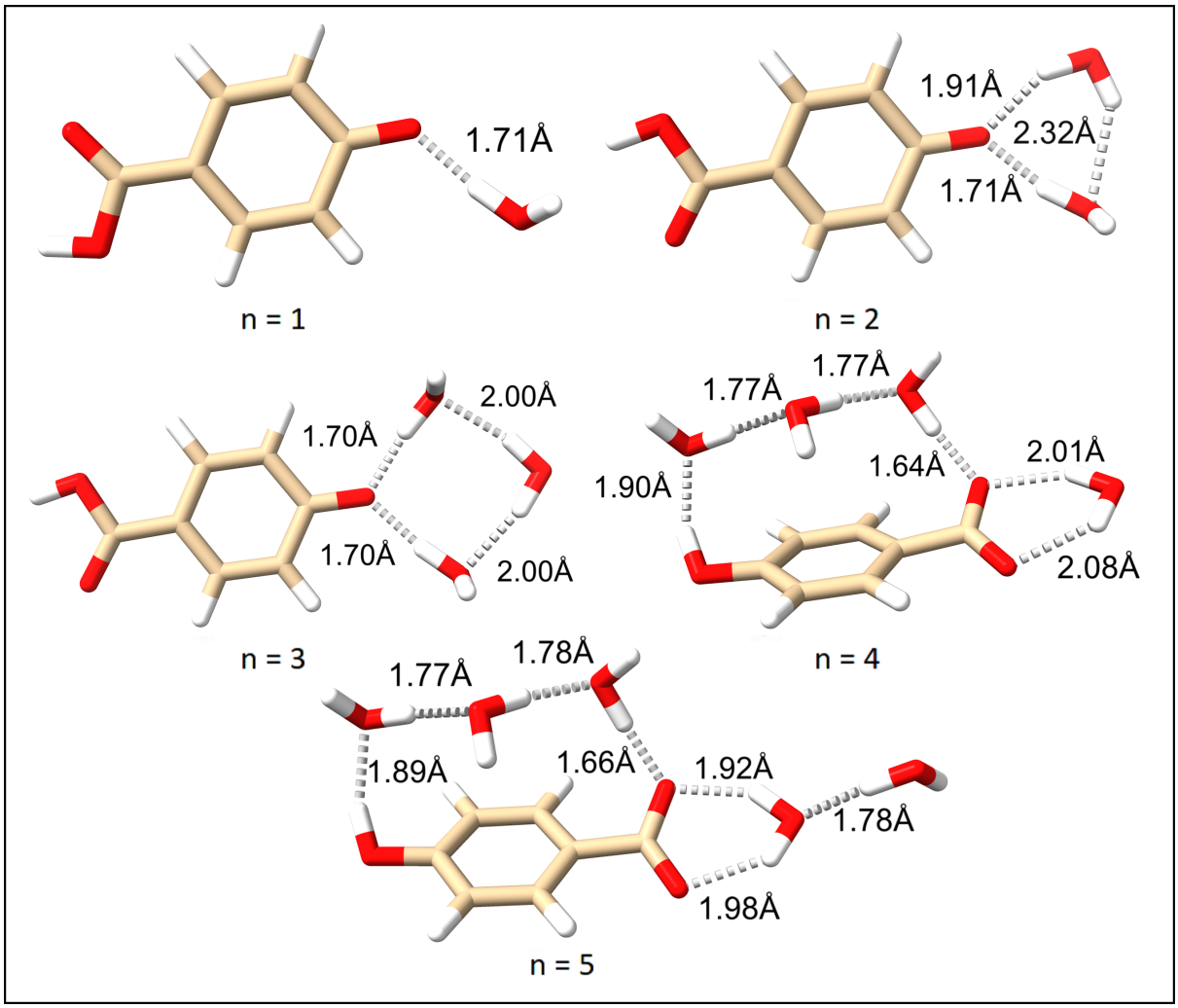

Figure 4.4: Global minimum conformations of $[PHBA\cdots(H_2O)_n]^-$ (n = 1 - 5) at 298 K determined by mp2(full)\6-311++D(d,p) single point energies with ωB97X-D\6-311++D(d,p) thermochemical corrections.

This effect has a significantly smaller impact on the alcohol clusters as the networks are less complex due to the limitation of a single hydrogen bond per molecule. This contributes to the bridging structure being less relevant until n = 5 where it becomes most favourable due to a reduction in steric effects as compared to those interactions favouring charge sites.

Taking a closer look at the global minimum structures for acetone reveals a strong preference for the tautomer that allows for the largest number of charge site interactions. For n =1 and n =2 the phenoxide is the perferred tautomer due to the reduced sterics of the acetone interacting with this site versus the carboxylic acid of the carboxylate. Upon the addition of the third acetone there is a shift to the carboxylate due to the steric hindrance of placing

another acetone on the phenoxide. As the cluster reaches n = 5 the global minimum includes the first dipole dipole interaction rather than a direct interaction with the charge site of the PHBA. Comparison of these clusters illustrates the ability of protic solvents to form highly ordered networks, while the aprotic form weakly bond dipole dipole clusters.

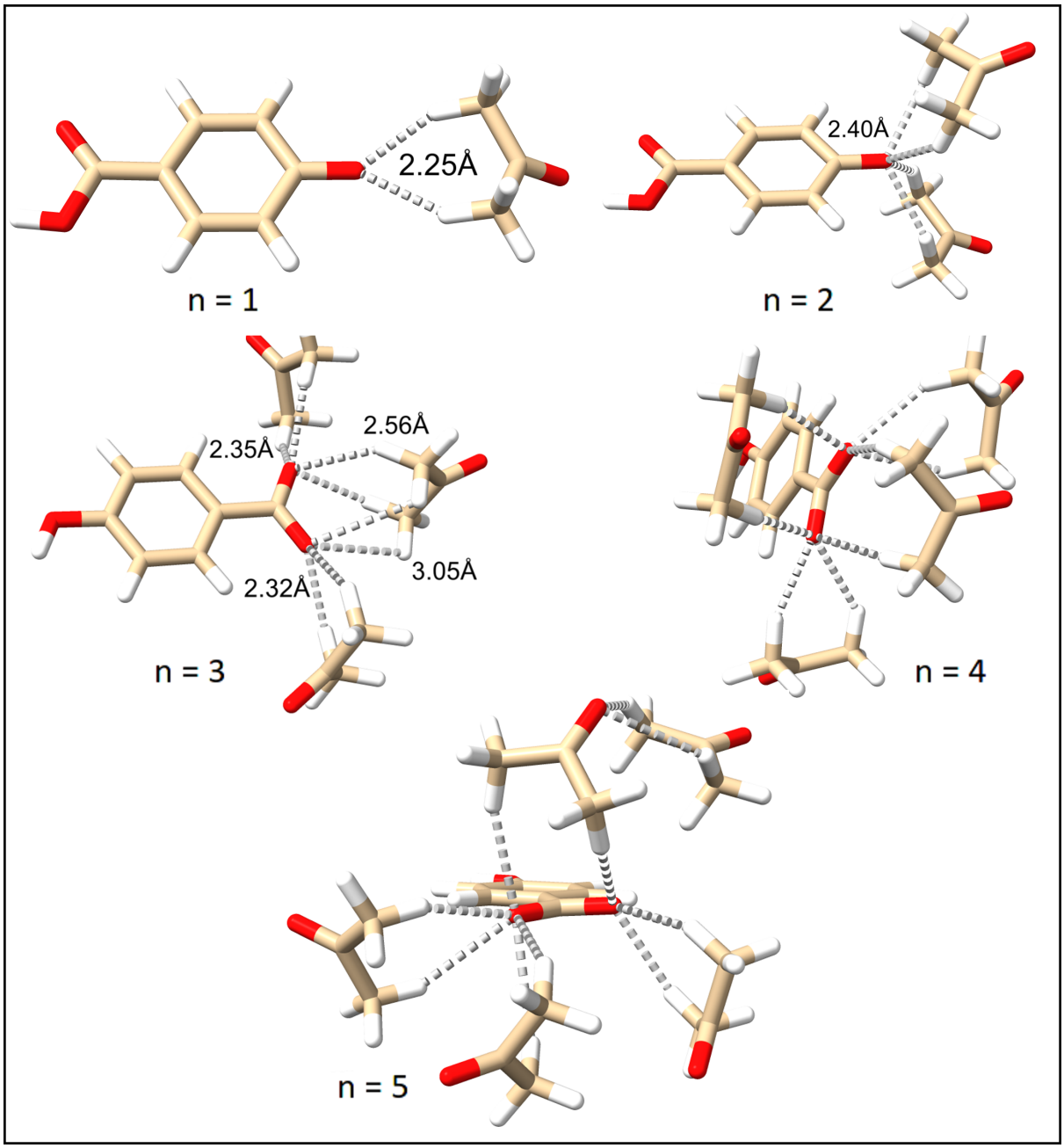

Figure 4.5: Global minimum conformations of [PHBA···(Acetone)$_n$]$^-$ (n = 1 - 5) at 298 K determined by mp2(full)\6-311++D(d,p) single point energies with ωB97X-D\6-311++D(d,p) thermochemical corrections.

4.3.3 Microsolvation studies of common ESI solvents at varying temperature

Examination of the relative population for the phenoxide tautomer as a function of temperature highlighted the effect temperature has on specific solvents rather than solvent types. An increase in temperature was shown to have little to no effect on water clusters, meanwhile ethanol saw its relative population return to almost completely 'gas phase' conditions at 450 K, as seen in **Figure 4.6**.

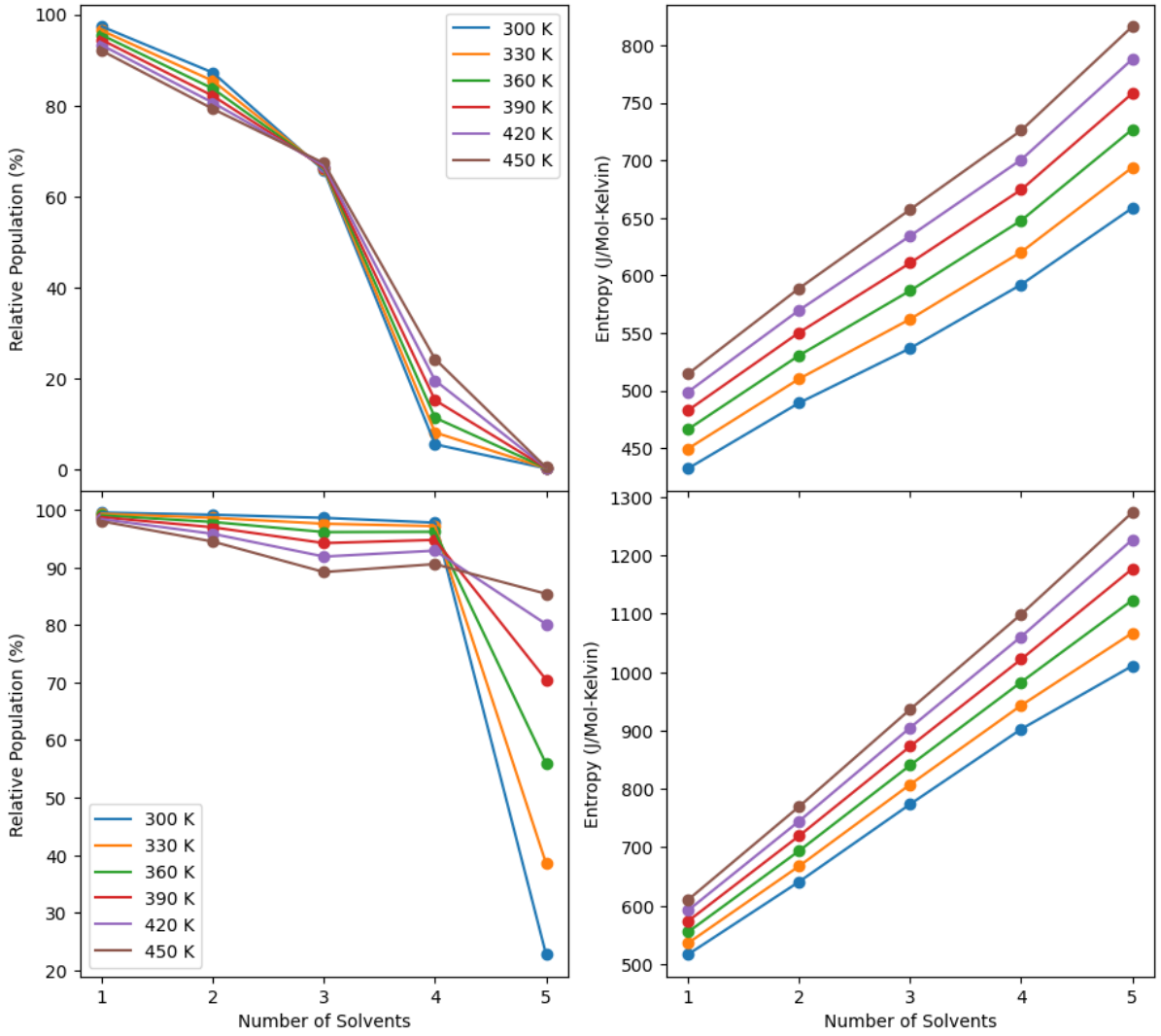

Figure 4.6: A comparison of the relative population for the phenoxide tautomer and weighted system entropy for water (top) and ethanol (bottom) . The temperature range examined was selected to highlight the effect a small increase in effective ion temperature has on tautomer population.

It can be observed in both cases that an increase in temperature generally resulted in a decrease to the population when its contribution was above 50 % or an increase to population when its

contribution was less than 50 %. However, this trend was not always observed, such as in the case of three and five water molecules, where the rigidity of hydrogen bonding networks were sufficient to prevent degradation by temperature. This was not observed in the other protic solvents because of the previously mentioned single hydrogen bonding nature of the alcohols. This coupled with the additional size of the alcohol molecules readily explained the shift back to 'gas phase' conditions that was observed for ethanol in **Figure 4.6**, due to the inability to overcome the effects of entropy. A comparison of the hydrogen bonding networks for n = 3 and n = 5 of water and ethanol, **Figure 4.7**, illustrates the difference between the networks, wherein ethanol has higher degrees of freedom, which are easily influenced by entropic effects, allowing for an easier breakdown of the system.

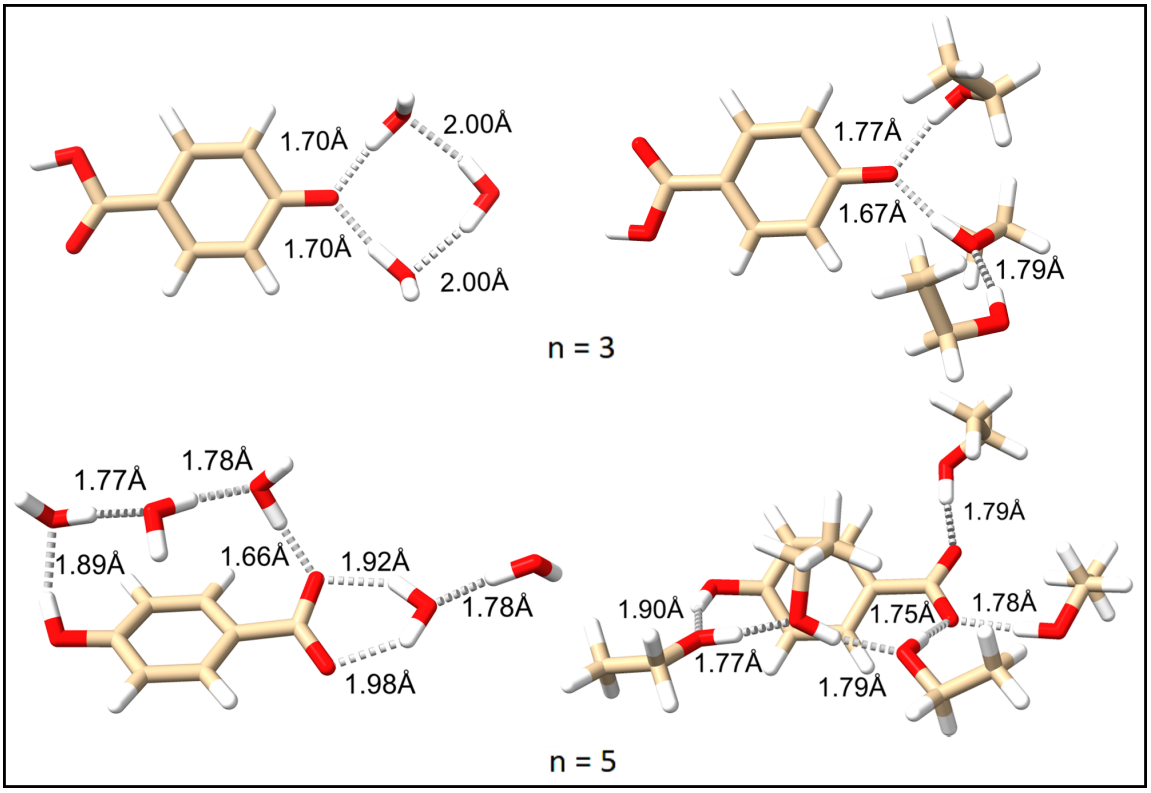

Figure 4.7: A comparison of the global minimum geometries for water (left) and ethanol (right) PHBA clusters for n = 3 and n = 5. The difference between the hydrogen bonding networks of the two protic solvents is quite apparently, wherein ethanol has a number of dangling hydrogen bonds in its global minimum geometries.

By examining the free energy of formation the effective population of each cluster size can be determined. Taking a look at the free energy of formations at 300 K, as seen in **Table 4.2**, the preferred tautomer can be estimated by examining the most favourable cluster size (n =

Table 4.2: Free energy of formation for various solvents calculated at 298 K using mp2(full)\6-311++D(d,p) single point energies with ωB97X-D\6-311++D(d,p) thermochemical corrections.

Cluster	**Acetone**	**Acetonitrile**	**Methanol**	**Ethanol**	**Water**
M + S = MS	−0.16	−8.48	−44.74	−17.07	−40.43
MS + S = MS_2	−7.25	−16.40	−66.30	−35.34	−52.01
MS_2 + S = MS_3	−33.58	−26.68	−78.84	−48.79	−62.72
MS_3 + S = MS_4	−30.80	−11.51	−87.14	−59.70	−58.00
MS_4 + S = MS_5	−27.51	−9.89	−79.37	−50.87	−70.45

5 for water) and comparing it back to **Figure 4.2**.

Expanding this process to include a range of temperatures up to 700 K, as seen in **Figure 4.8**, shows how these cluster populations change as a function of temperature. The increase in temperature reduces the population of large clusters, with 100% of the population consisting of single solvent clusters at 700 K.

Looking at the relative populations reveals interesting trends amongst the different solvents. Looking at the water populations the n = 4 cluster has no significant population, referring back to **Table 4.2**, we see that the addition of the fourth water is not as spontaneous as the other 3rd and 5th addition, suggesting that the n = 4 cluster serves as an intermediate to the formation of the n = 5 cluster.

Both aprotic solvents showed a varying degree of preference of n = 3, suggesting that the carboxylate is the prefered tautomer at room temperature. Interesting, unlike all other solvents, acetone was found to display an increase in the carboxylate tautomer approaching 400 K, whereas all other solvents quickly transitioned towards the phenoxide with an increase in temperature.

Therefore, by returning to **Figure 4.2** to compare the results of **Figure 4.8** it can be concluded that all solvents would display phenoxide tautomer preference at temperatures of 700 K and above. Use of these two plots in tandem allows for an estimation of the preferred tautomer at a given temperature, providing a potential explanation for the variable preference of tautomers seen between experiments.

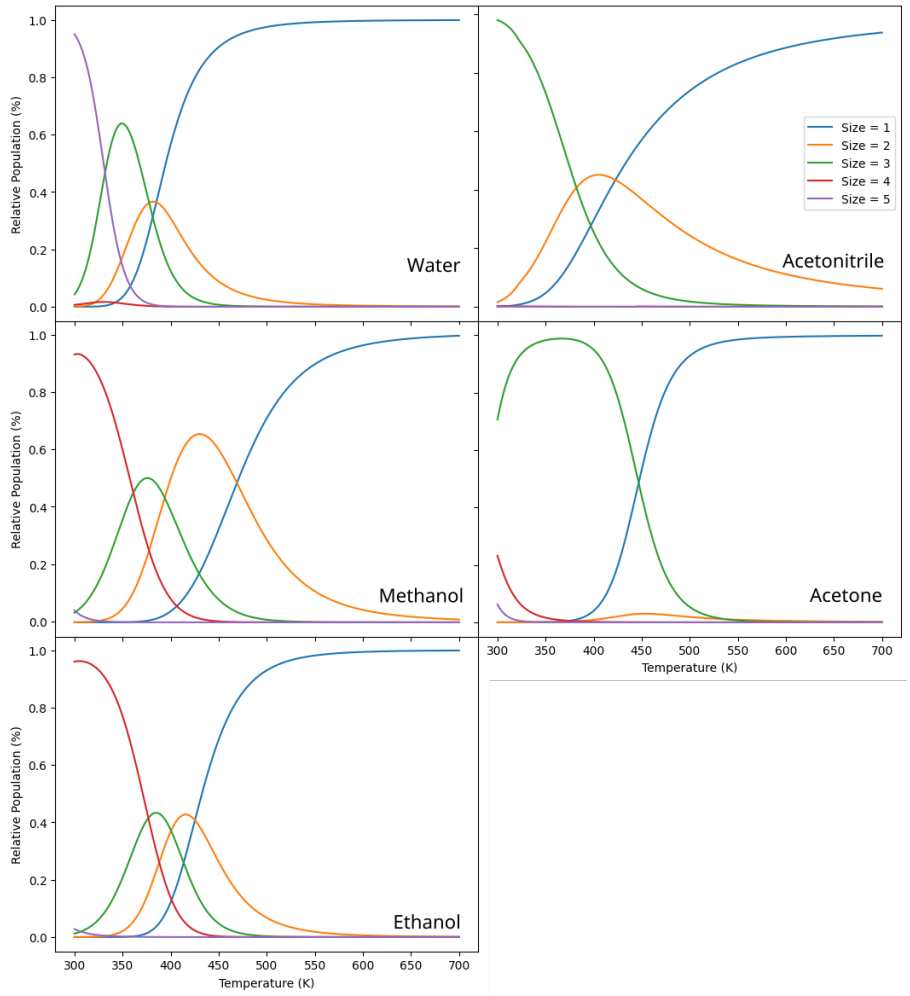

Figure 4.8: A comparison of the relative population for solvent size = n clusters. Low temperatures favour the formation of the most exothermic cluster sizes while an increase in temperature reduces cluster sizes.

4.4 Conclusion

In conclusion, the examination of solvation by theoretical study greatly complements experimental results. In agreement with IM-MS, water was found to be the solvent that most prefers the carboxylate tautomer under 'solution phase' conditions; however, it was also found that there was no bias for tautomer preference dependent on solvent type. Examination of the effective ion temperature resulting from ESI spray conditions revealed a significant impact on the relative populations of the tautomers. This study highlights the importance of understanding the effects of ESI conditions and how they might influence isomer preference experimentally.

Chapter 5

The structure and properties of ionic all-cis 1,2,3,4,5,6-hexafluorocyclohexane complexes

5.1 Introduction

all-cis 1,2,3,4,5,6-hexafluorocyclohexane (HFCH), first synthesized in 2014 by the O'Hagan group at the University of St. Andrews in the United Kingdom, is a novel molecule that has been shown to be able to bind both cationic and anionic species.[147] This property arises due to the facial polarization of the molecule with strong capability to bind both positive and negative ions as a result of the large dipole moment of 6.2 to 7.4 Debye.[29,147] HFCH has been shown to have a pronounced propensity to bind both cations and anions with binding enthalpies of large magnitude which are exceeded only by appreciably larger cyclic polyethers such as crown ethers and other cryptands.[27–29]

Previous research on cyclohexane has shown that two conformations, chair and twist-boat, have been observable in the gas-phase with the cyclohexane chair being lower in energy by approximately 20-24 kJ/mol, and a barrier to conformational change of approximately 45kJ/mol.[148,149] Examination of the analogous potential energy surface (PES) has shown that, similarly to cyclohexane, HFCH can assume both chair and twist-boat conformations, with the chair being approximately 34 kJ/mol lower in energy, as shown in **Figure 5.1**. The increased energy difference between these two conformations, as well as the increase in barrier height to approximately 66kJ/mol, may explain the apparent lack of twist-boat conformer seen in the experimental spectra as described in the preliminary report of the unique character of HFCH.[29]

The minimum energy chair structure of HFCH lends itself to facial polarization and the strong dipole moment observed for the molecule. This appreciable dipole arises due to the presence of the six C-F bonds oriented all outward on a single face, which is a result of the fact that

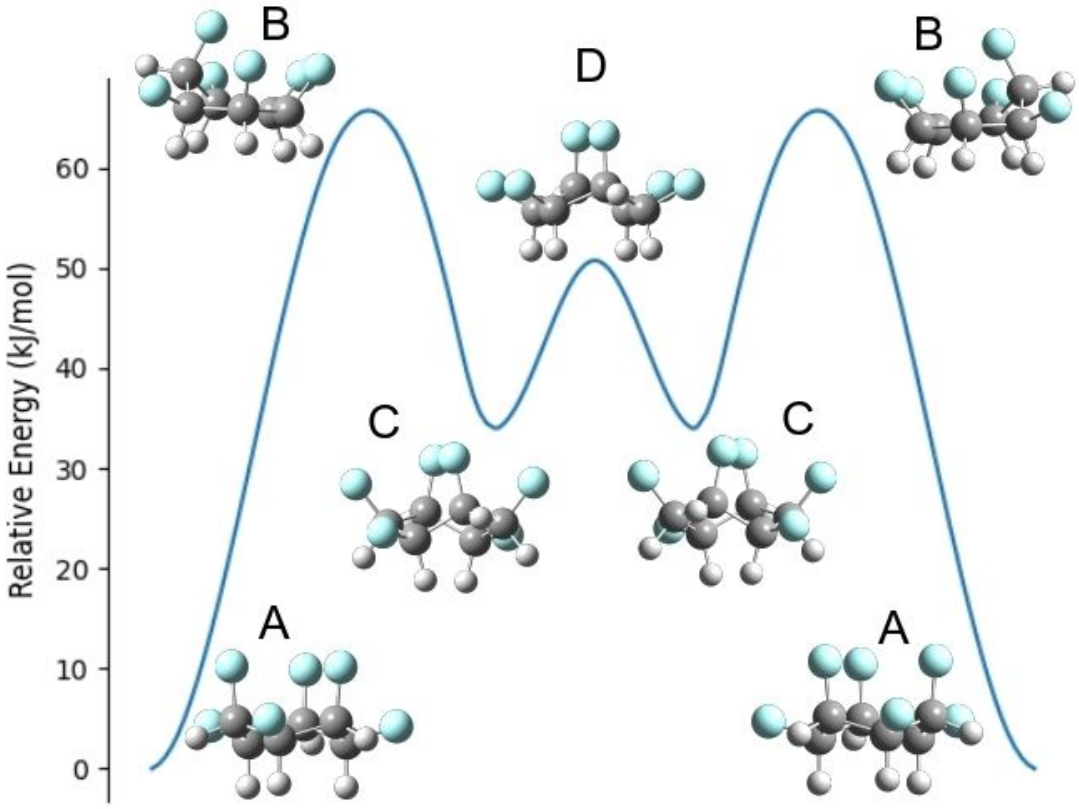

Figure 5.1: The PES of HFCH, showing a transition between the many conformation of HFCH being: the chair (A),the half-chair (B), the twist-boat (C), and the Boat (D) conformations.

the C-F bond is the most polarized bond in organic chemistry due to fluorine being the most electronegative element.[150] This stark contrast to the presence of six C-H bonds on the opposite face results in a strong dipole moment in the direction of the hydrogen face. These unique characteristics also give rise to the possibility of forming neutral dimer species in the presence of ions as will be shown experimentally, and possibly higher order species, giving unique experimental gas phase spectra in the presence of ions.

5.2 Experimental

All infrared multiple photon dissociation (IRMPD) spectra were acquired at the Centre de Laser Infrarouge d'Orsay (CLIO) free electron laser (FEL) facility at the university of Paris XI.[81,151] Ionic clusters of HFCH were generated by use of electrospray ionisation (ESI) where 100 μM solutions of HFCH in water/methanol (50/50 vol%) containing ratios of 1:5 to 1:3 of ionic salts to HFCH. A Bruker Esquire 3000+ ion trap mass spectrometer was used to mass

select ionic clusters which were subsequently irradiated by the wavelength tunable output of the FEL. The clusters were examined across the 850-1800 cm^{-1} range at 5 cm^{-1} intervals for 400 ms. This produced a series of vibrational spectra obtained as fragmentation efficiency of depletion of the ionic HFCH cluster species as a function of wavenumber. Additional details of the experimental apparatus and IRMPD process have been previously described.[49,152]

5.3 Computational methods

In order to obtain accurate thermochemical data for ionic complexes of HFCH a number of density functional theory (DFT) methods were examined together with the Møller–Plesset perturbation theory second order (MP2) level of theory. This was based on the results of recent publications which have shown that the Minnesota 06-2X (M06-2X) and Modified Becke 97 exchange-dipole moment (ωB97X-D) methods are significantly more accurate compared to that of the Becke, 3-parameter, Lee–Yang–Parr (B3LYP) method. In addition, they have similar accuracy to the MP2 level of theory.[52,153–157] However, the dipole moment of HFCH is significantly stronger than the majority of molecules studied in these benchmarks. Therefore, each DFT method, as well as MP2, was benchmarked to determine if these claims hold true in the case of ionic complexes of HFCH.

Each method outlined was selected due to a strength in a specific area when calculating the energies of molecular species. B3LYP is one of the most commonly used DFT methods due to the speed with which accurate geometries and energies can be determined. The M06-2X method, employing a correction for empirical dispersion (Grimme Dispersion 3 (GD3)), was selected for its accuracy with simple fluorocarbon species.[51–54] The ωB97X-D method was selected as it was one of the most accurate methods for calculating energies as found by Mardirossian and Head-Gordon in a comparison of 200 DFT methods comparing 5000 data points.[52,55]

The MP2 level of theory was selected as there are no approximations made to calculate the wavefunction in comparison to the DFT level of theory, making the energy approximation more accurate; however this comes at a significant computational cost.[158–160] Due to the large number of electrons present in the dimer systems studied here the MP2 method utilizing all electrons was not possible due to computational restraints. Thus, a comparison of the MP2

energies was made in the monomer systems to determine the similarity of DFT systems for use in dimer systems.

The Basis sets selected were chosen in an attempt to produce the most computationally reasonable binding energies. All carbon and hydrogen atoms were subjected to the def2-tzvp basis set for optimizations and vibrational frequencies as it had previously provided good agreement with experimental spectra, while being relatively computationally inexpensive.[129,161,162] This protocol was expanded to include fluroine atoms, with the exception of the fluoride anion, to reduce the overall computational runtime. The sodium and lithium cationic species were treated using the aug-cc-pCVTZ basis set due to accuracy in both energetics and agreement seen in previous comparisons to IRMPD.[50,163,164] All other ionic species were run using the def2-tzvppd basis set to minimize the root mean square difference (RMSD) of the zero-point vibrational energy (ZPVE).[165] Basis set data for def2-tzvppd was obtained from the basis set exchange (BSE) and all calculations were run using the Gaussian 16 revision C.01 computational suite.[95,166] Thermochemical scaling factors were found to be significantly variable with multiple sources reporting scaling factors in the range of 0.92-0.97%.[165,167,168] All structure graphics were generated using the ChimeraX package.[139,140]

5.4 Results and Discussion

Expanding on the results of Ziegler et al.[29] to include all alkali and halide ions resulted in the discovery of an unusual trend in the experimental IRMPD spectra.It was found that the vibrational modes of ionic HFCH complexes seemed to become more blueshifted with increasing ionic size, as seen in **Figure 5.2**. This is likely the result of the decreasing magnitude of the ion-dipole interaction of the complexes as ion size increases. Previously, it had been shown that this interaction between HFCH and sodium and chloride ions was among the strongest reported in the National Institute of Standards and Technology (NIST) database.[29]

In the experimental spectra obtained in 2015, it was observed that there was an absence of the fluoride monomer. The monomer species was not detected in the ion trap, with isolation of the fluoride dimer and fragmentation by IRMPD being the only viable method to form this species. This may be explained by sufficient energy being provided to the system allowing for the fluoride

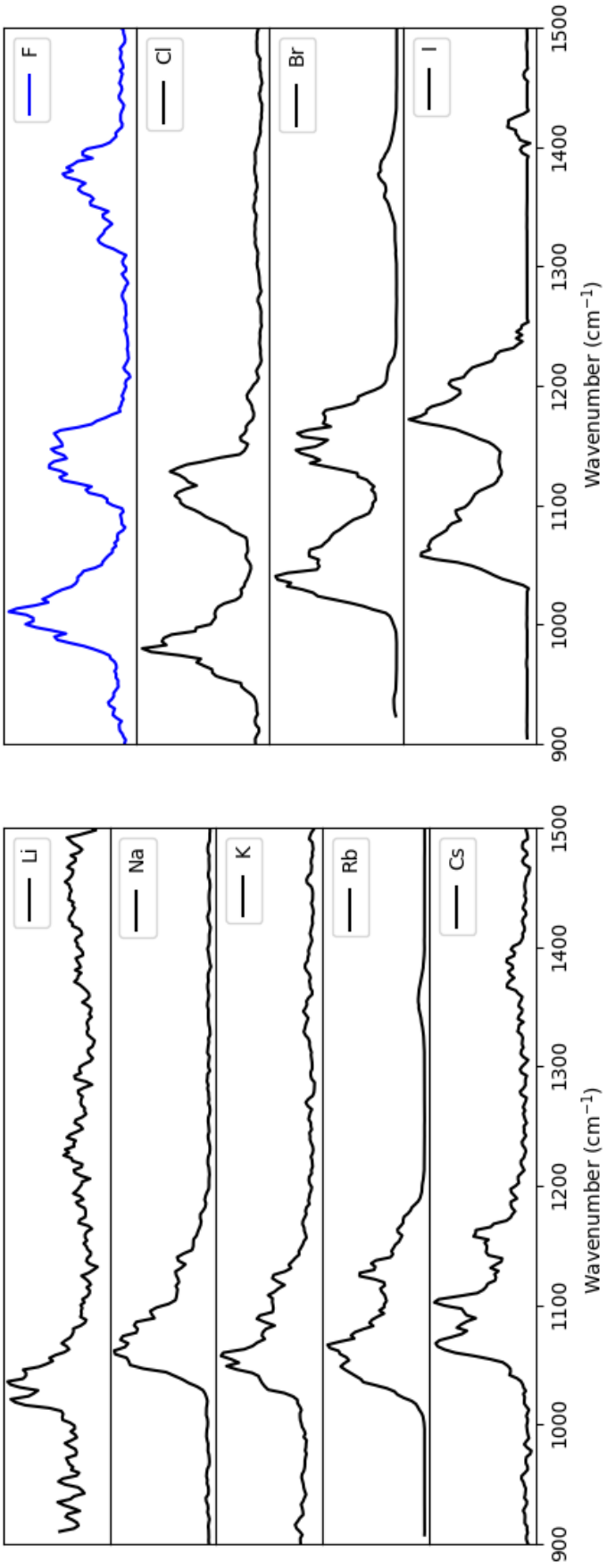

Figure 5.2: The experimental monomer ionic complexes of HFCH captured in 2015 (black) and 2018 (blue) using a 3 point smooth. A shift in the C-F/C-H stretch, ~1000 - 1100 cm^{-1}, can be seen as the ions increase in size.

anion to abstract a hydrogen from the HFCH. However, this phenomenon was not observed in spectra captured in 2018, and the monomer species were seen under both monomer and dimer conditions. In addition to the fluoride monomer species, it was noted that the dimer spectra were markedly sharper, which will be discussed in the computational analysis below.

Following the methodology of Ziegler et al.[29] , both alkali and halide ions were studied using B3LYP.The vibrational modes for these ions were calculated and then scaled to account for anharmonic effects. However, when a scaling factor was applied to our analysis and compared to experiment, it was observed that it did not correct for the shift in vibrational modes as ion size increased. Thus, the need to explore other popular methods, outlined in the methods, in an attempt to correct for mode shifting was required.

Comparison to the lithium spectrum, **Figure 5.3**, shows that B3LYP is the best match to the spectrum, while the other methods are blueshifted. This trend follows for potassium and sodium, while the larger rubidium and caesium ions show B3LYP blueshifted in comparison to the other methods, as seen in **Table 5.1**.

The results of this comparison were problematic as none of the methods tested were able to accurately account for the shift of peaks seen between ions of different sizes. While B3LYP produced the spectra that were the most similar to the experiment, it has been noted that it is very inaccurate when used to study the energy of a system.[52] Additionally, anharmonic calculations run using B3LYP displayed no improvement in matching the experiment. Therefore, the DFT method that produced the most accurate binding affinities would be selected for further analysis of the system.

Table 5.1: Average difference between experimental and computational spectra for equitorial and axial C-F stretches in monomer cation HFCH complexes.

Ion	**B3LYP**	**M06-2X**	**WB97XD**	**MP2**
Li	24	66	46	46
Na	5	38	18	18
K	7	47	25	27
Rb	15	23	5	6
Cs	45	6	25	25
Average Error	19	36	24	24

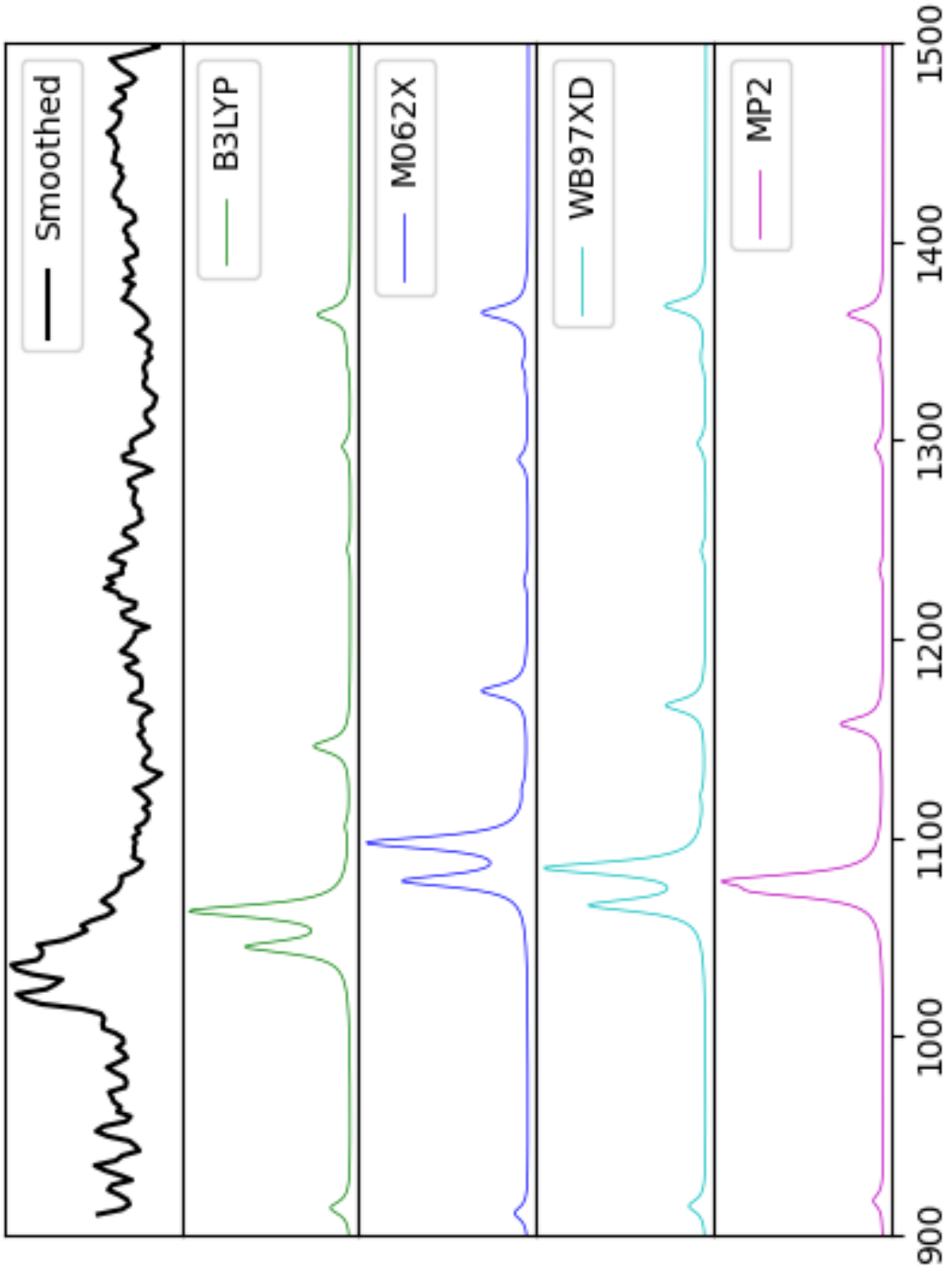

Figure 5.3: The experimental monomer complex of lithium with HFCH. B3LYP shows the most similarity compared to the other methods when corrected for anharmonic factors.

Table 5.2: Calculated free energy (kJ mol^{-1}) values for binding ionic species found using various methods at 298 K.

Ion	B3LYP	M062X	WB97XD	MP2
Li	−204.41	−199.49	−186.60	−198.31
Na	−148.49	−137.82	−128.10	−136.30
K	−110.82	−99.53	−90.70	−96.95
Rb	−100.19	−88.81	−80.74	−88.03
Cs	−89.83	−79.78	−90.99	−77.05
Cl	−114.48	−116.61	−109.79	−114.14
Br	−103.19	−103.21	−98.84	−106.24
I	−89.40	−89.86	−85.63	−93.08

Examination of the free energy of formation for each method, as seen in **Table 5.2**, demonstrated the strengths of selecting DFT functionals for a specific use case. As mentioned above, M06-2X was selected due to it's accuracy in calculating fluorocarbon species, which is quite apparent in the comparison to the MP2 method, showing a maximum difference of 3.22 kJ mol^{-1}.[51–54] B3LYP and ωB97X-D both produced significant deviations of approximately 10 kJ mol^{-1} on average. ωB97X-D was unable to properly utilize effective core potentials found in the caesium cluster showing an increase in affinity over the rubidium. B3LYP and ωB97X-D were seemingly unable to sufficiently approximate the effect of the dipole-ion interaction either over approximating or under approximating respectively. M06-2X was therefore selected as the method of choice for analysis due to it's similarity to MP2, with thermochemistry seen in **Table 5.3**.

Table 5.3: Calculated energies (kJ mol^{-1}) for binding ionic species using M06-2X with GD3 dispersion corrections at 298 K.

Ions	Electronic	Enthalpy	Free Energy	Entropy (J/Mol-Kelvin)
Li	−233.53	−236.01	−199.49	−122.50
Na	−170.37	−172.85	−137.82	−117.47
K	−130.66	−133.14	−99.53	−112.74
Rb	−118.63	−121.11	−88.81	−108.35
Cs	−108.50	−110.97	−79.78	−104.63
F	−220.35	−222.83	−191.73	−104.30
Cl	−142.80	−145.28	−116.61	−96.19
Br	−129.30	−131.78	−103.21	−95.84
I	−114.81	−117.29	−89.86	−92.00

With the selected method of analysis, the effect of the ion-dipole interaction could be investi-

gated. As previously mentioned, as the ion increased in size the vibrational modes blueshifted. To study this effect, species were optimized and then examined with a dummy atom placed at the ring centroid of HFCH to determine bond distances, as seen in **Figure 5.4**. The optimized geometries produced a linear relationship between the HFCH centroid distance and Van der Waals ion radius, as seen in **Figure 5.5**. Similar to previous studies, it was found that as the ion size increased there was an asymptotic diminishing effect on binding affinity.[164,169]

Table 5.4: A comparison of binding affinities (kJ mol^{-1}) for the chair and twist-boat cationic HFCH monomer complexes.

Ions	Chair	Twist-Boat	Difference
Li	−199.49	−190.58	−8.91
Na	−137.82	−131.55	−6.27
K	−99.53	−95.49	−4.04
Rb	−88.81	−84.62	−4.19
Cs	−79.78	−76.43	−3.35
F	−191.73	−183.13	−8.6
Cl	−116.61	−108.46	−8.15
Br	−103.21	−95.83	−7.38
I	−89.86	−82.65	−7.21

In addition to the chair conformation, there exists the possibility of the twist-boat, albeit approximately 34 kJ mol^{-1}higher in energy, as seen in **Figure 5.1**. The twist-boat may be kinetically trapped during the ESI process wherein the solvent droplet is exposed to effective temperatures of 5 - 600 K, providing ample energy to convert between isomers before cooling in the ion trap.[60,63,170] Thus, the need to compare both the twist-boat and chair conformations

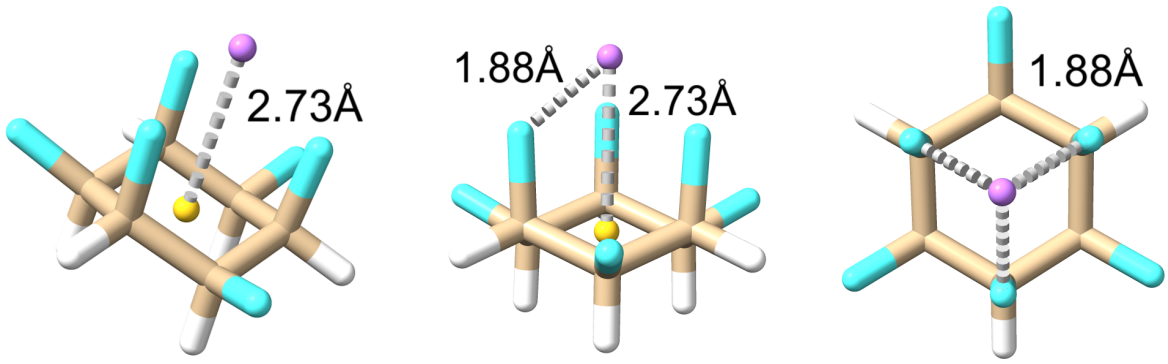

Figure 5.4: The optimized geometry of the lithium monomer, with the ring centroid indicated by a gold dummy atom. The distance to each fluorine on the face was within 0.01Å.

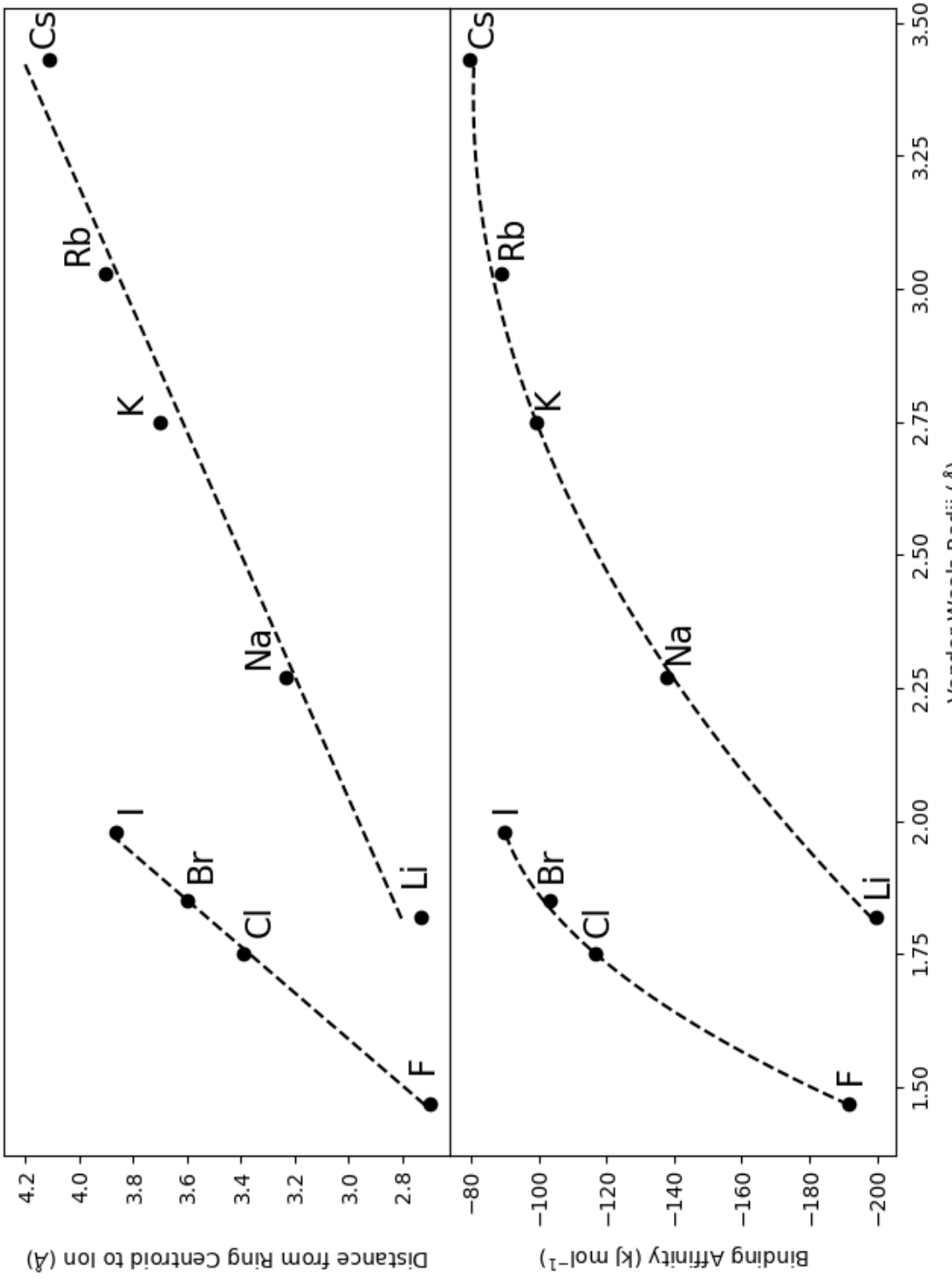

Figure 5.5: The relationship between the distance to the ring centroid relative to Van der Waals radius can be seen on the top. The bottom shows the relationship between the binding affinity and the Van der Waals radius.

to the experimental spectrum was required to account for all possible modes.

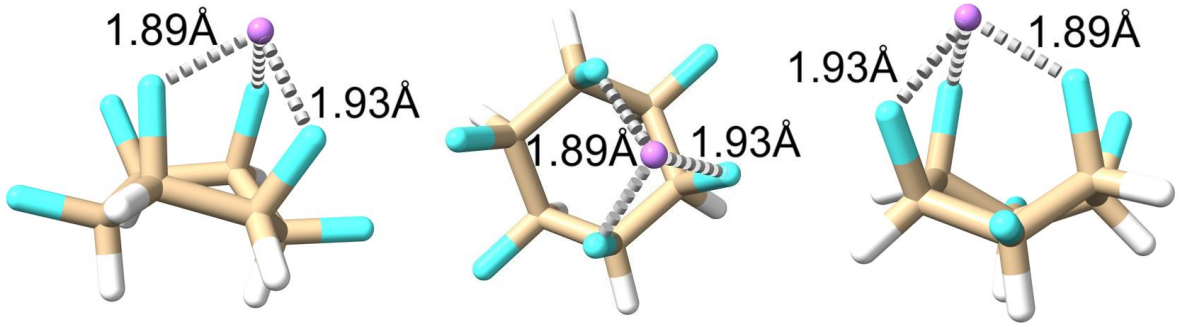

Figure 5.6: The optimized geometry of the lithium twist-boat monomer. Two points of interaction "share" a bond distance while one is slightly elongated.

Comparison of the binding affinity found the twist-boat to be very similar to that of the chair conformation, as seen in **Table 5.4**, with the difference between each conformation shrinking as ionic radius increases. The twist-boat, as seen in figure **Figure 5.6**, has asymmetric interactions with the cationic species, while the chair has symmetric interactions. The length of the symmetrical interactions of the chair become greater than the length of the two point symmetrical interactions of the twist-boat as the ions increase in size, as seen in **Table 5.5**. Additionally, the effect of symmetry on binding affinity is seemingly less significant in the anionic species, likely due to the anions having significantly smaller Van der Waals radii and greater bond distances to the polarized face compared to that of the cationic species.

Table 5.5: A comparison of bond distances (Å) for the chair and twist-boat ionic HFCH monomer complexes. The anionic twist-boat complexes have three unsymmetric bond distances, while the cationic twist-boat complexes has two "symmetrical" bond distances (1&2) while one is slightly elongated (3).

Ions	**Chair**	**Twist-Boat (1)**	**Twist-Boat (2)**	**Twist-Boat (3)**
Li	1.88	1.87	1.89	1.93
Na	2.24	2.22	2.25	2.31
K	2.61	2.58	2.61	2.71
Rb	2.78	2.73	2.77	2.91
Cs	2.95	2.90	2.94	3.08
F	1.95	1.79	1.85	2.55
Cl	2.51	2.39	2.48	2.84
Br	2.69	2.57	2.66	3.00
I	2.92	2.81	2.90	3.17

Experimental IRMPD vibrational frequencies show excellent agreement with both the chair and twist-boat conformations, as seen in **Figure 5.7** for the caesium monomer when scaled by 0.939,

within the bounds of deviation for the optimal scaling factor of 0.945 ± 0.07 as reported in literature.[168] The chair produces a very clean spectrum, with the three major modes being a C−F_{eq} stretch at 1085 cm^{-1}, a C−F_{ax} stretch at 1104 cm^{-1}, and a ring breathing mode at 1165 cm^{-1} respectively. The twist-boat produces a relatively complex spectrum compared to that of the chair with the dominant peak being a combination of both C−F_{eq} and C−F_{ax} stretches at 1135 cm^{-1}. The shoulder peak in the experimental around 1200 cm^{-1} is explained by a weak ring breathing mode at 1211 cm^{-1} in the twist-boat conformation. Although it is a weak feature computationally, it is important to note that computational intensities are not representative of experimental results.[171,172] This is because the calculation for peak intensity is reliant upon the dipole moment of the species, introducing variability dependent upon the method and basis set select. For example, the calculated dipole moment of HFCH showed a variation of 5.94 D, 5.98 D, 5.80 D, and 6.65 D for B3LYP, M06-2X, ωB97X-D and MP2 respectively. The peak around 1350 - 1400 cm^{-1} in the experimental spectrum is the result of a C−H_{wag} in both the chair and twist-boat conformations at 1361 cm^{-1} and 1378 cm^{-1} respectively. Comparison between the other monomer ionic clusters and experimental spectra can be found in Appendix A, where similar results were found using varying scaling factors.

A similar comparison can be made for all ions using the weighted spectrum of the chair and twist-boat isomers to simplify the comparison to the experimental spectra, as seen in **Figure 5.8**. This comparison shows excellent agreement for cationic species; however, comparison in the anionic spectra show very broad peaks in comparison to the cationic species. Peak broadening may result from the anion dipole interaction, in anionic systems the dipole aligns with the anionic species allowing anionic species to more strongly influence the C−H_{ax} and C−H_{eq} stretches of the HFCH.

An examination into the dimer spectra obtained in 2015, as seen in **Figure 5.9**, found identical behaviour to that of the monomer species. Vibrational modes became blueshifted with increasing ionic size, and had relatively broad unresolved peaks. Applying the methodology of the monomer species to the dimer species it became immediately apparent that the broad spectra were not simply explained by the conventional HFCH-ion-HFCH sandwich arrangement. Thus, the need to explore a number of mixed chair and twist-boat conformations was required to

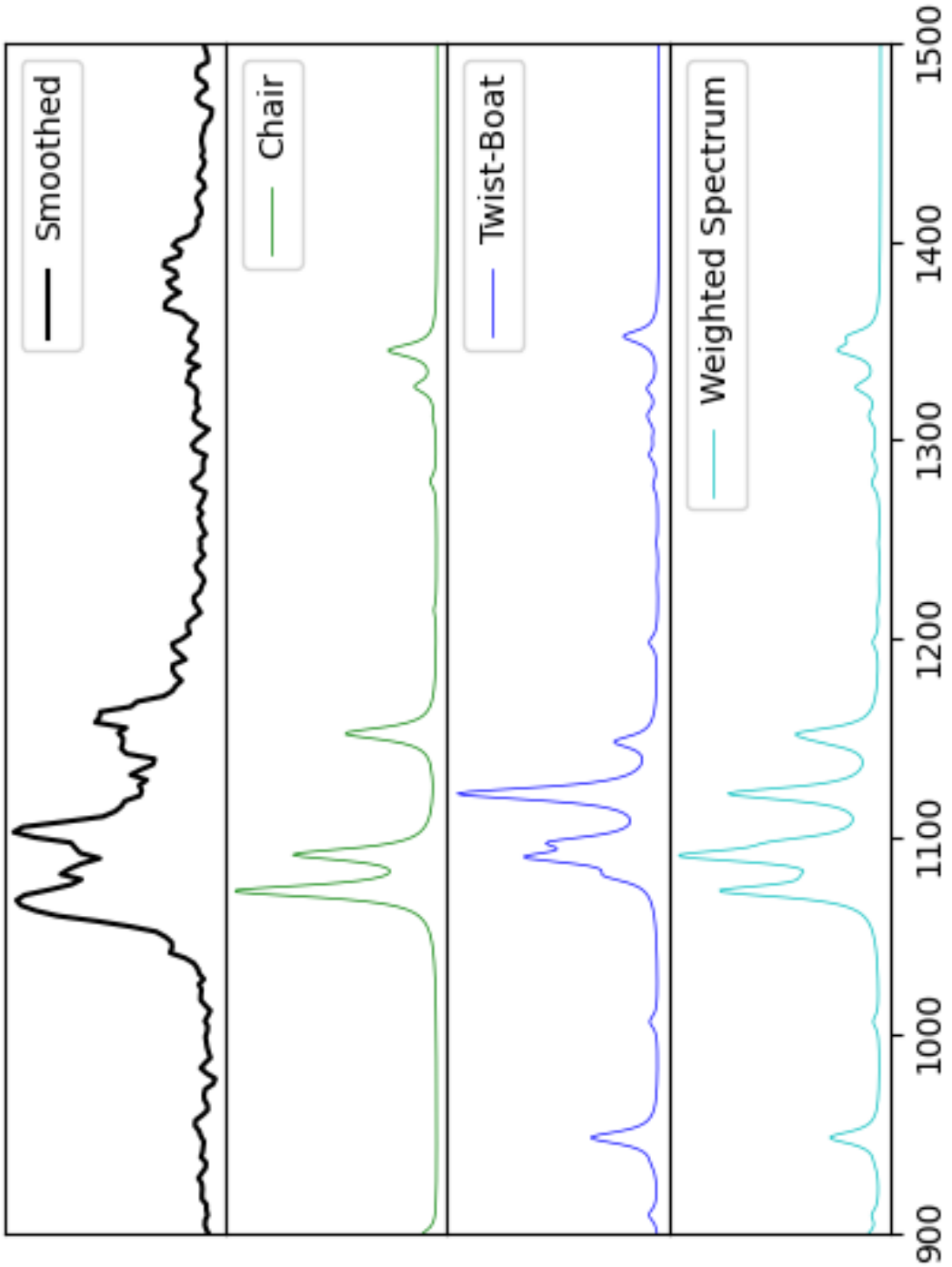

Figure 5.7: A comparison of the experimental smoothed IRMPD spectrum with the chair and twist-boat conformations of HFCH with a caesium ion.

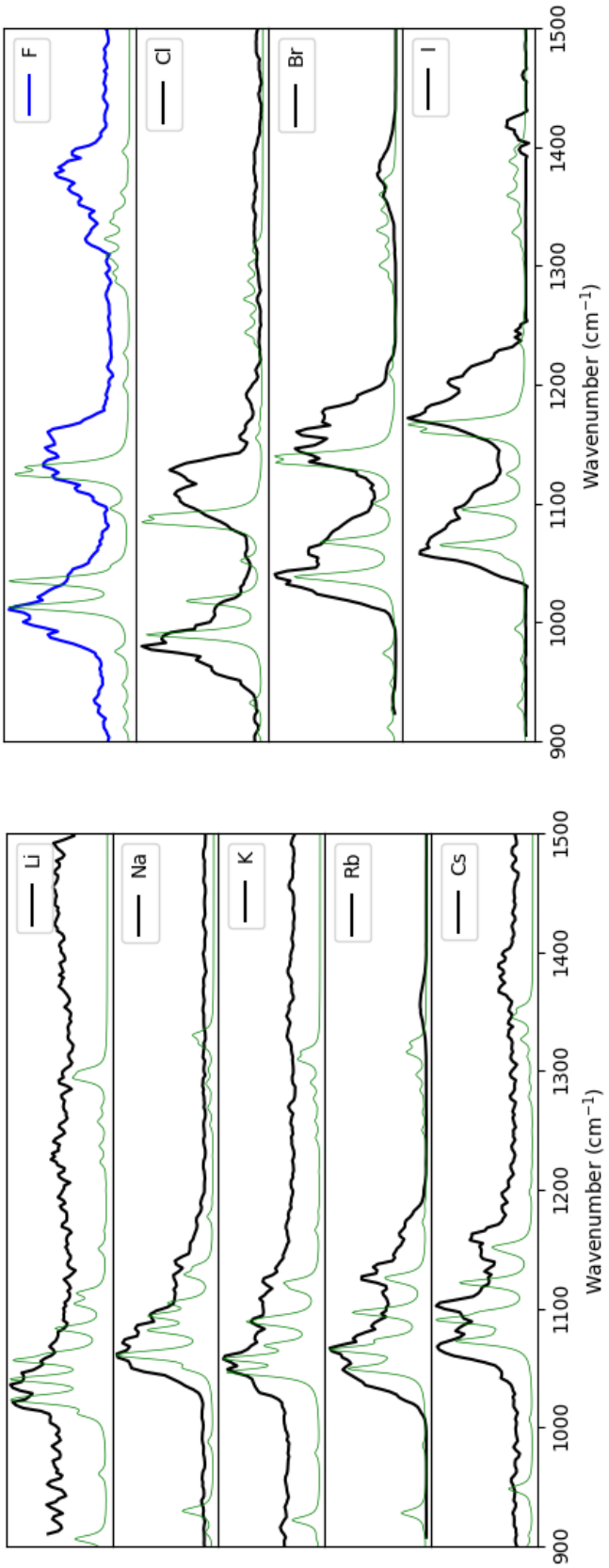

Figure 5.8: A comparison of the experimental smoothed IRMPD spectrum with the weighted computational spectra for the chair and twist-boat conformations of HFCH.

sufficiently explain all vibrational modes found in the experimental IRMPD spectra.

Attempting multiple configurations of the dimer species revealed that the strength of the dipole for HFCH allows it to undergo self dimerization to form a dipole bound dimer, as shown in **Figure 5.10**, with the formation of this species being slightly endothermic (ΔH = $\sim$ 5 kJ mol^{-1}). However, this is significantly lower in energy than the twist-boat isomer which is required to overcome the energy barrier of the half-chair intermediate species (ΔH = $\sim$60 kJ mol^{-1}), making it significantly more likely to be observed experimentally. Similar to that of the monomer unit, the dipole bound dimer can interact quite favourably with both cationic and anionic species. It was also found that mixtures of the chair and twist-boat isomers readily formed dipole bound dimer species.

Optimization of the various dimer species found a total of seven possible configurations for the chair and twist-boat isomers, as seen in **Figure 5.11**. There were four dipole bound isomers in which the mixture of the two isomers could result in either the chair or the twist-boat isomer interacting with the ion of interest. Another interesting feature of the dipole bound dimers was that the homogeneous twist-boat dimer optimized to a twist-boat bound to a boat that has four points of interaction with the ionic species. This was quite interesting as the boat conformation is considered a transition state, as observed in **Figure 5.1**, but this species contained no imaginary vibration modes. The heterogeneous mixture with the twist-boat closest to the ion did not optimize to a stable boat intermediate. The sandwich conformations showed no unique behaviour, with vibrational modes being very reminiscent of the monomer species. Six of the seven dimer isomers maintained consistent bond length for ion interaction in both the heterogeneous and homogeneous mixtures. However, this was not observed in the case of the chair-(twist-boat)-ion, which resulted in the longest bond interactions with ionic species upon conversion to the boat conformation.

Comparing the bond lengths of these dimer systems we can see that, in the presence of an ion, the bond lengths are shortened for the dipole dimers and elongated for the sandwich dimers. In the monomer system it was found that sodium would interact with the chair at a distance of 2.24Å but in the dimer system it would interact at a distance of 2.30Å. A similar trend was

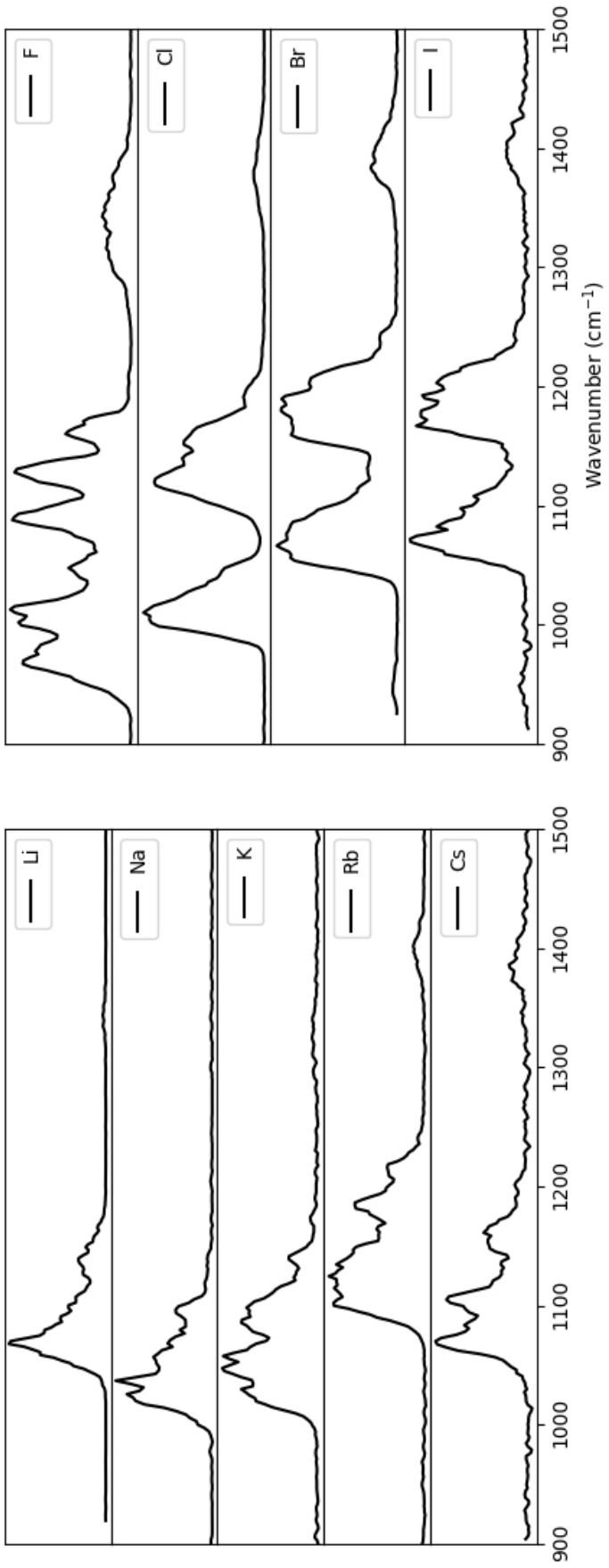

Figure 5.9: The experimental dimer ionic complexes of HFCH captured in 2015. A shift in the C-F/C-H stretch, ~1000 - 1200 cm^{-1}*, can be seen as the ions increase in size, this effect is significantly more apparent for the anionic species.*

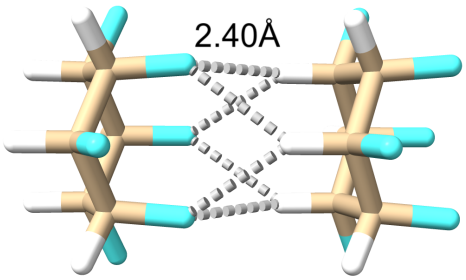

Figure 5.10: The optimized geometry of the dipole dimer species of HFCH. The enthalpy of formation is roughly 5 kJ mol^{-1}.

found in the twist-boat where all bond interactions were found to be elongated by approximately 0.06Å. The exact opposite of this effect was found in the dipole dimers where bond interactions were found to shorten by approximately 0.1Å. This is can be explained by the dipole moments of the sandwich dimers versus the dipole dimers. In the sandwich dimers the dipoles work against each other, competing for dipole ion interactions, whereas in the dipole dimer, while the dipoles are aligned, resulting in a tightening of the interactions. Again, this effect was lessened by the size of the ionic species, with larger radii ions showing a smaller deviation in bond lengths when compared to the monomer species, especially for anionic species.

Examination of the vibrational modes, as seen in **Figure 5.12**, shows possible evidence for the existence of all seven dimer systems in the gas phase. In all species, the peaks around 1350 - 1400cm^{-1} are a result of C-H wags in either or both molecules, resulting in a series of peaks in that region. The broadness of the peak around 1170 cm^{-1} in the experimental spectrum suggest the presence of the computationally weak intensity ring breathing modes in twist-boat containing systems, seen around 1150 cm^{-1} to 1180 cm^{-1}in the various dimers.

Beginning with the T-T-I isomer, the shoulder to the left of 1120 cm^{-1} is a series of C$-$F$_{ax}$ and C$-$F$_{eq}$ stretches in twist-boat furthest from the ion, with the largest mode corresponding to the stretching motion of the two C$-$F$_{eq}$ bonds in the boat. The second largest peak around 1150 cm^{-1} is a result of the stretching motion of the four C$-$F$_{ax}$ bonds in the boat. The peaks to the right of this are a result of ring breathing modes in the boat and twist-boat respectively.

Moving onto the first mixed dimer, T-C-I, we see predictable behaviour of modes resulting from each isomer, with subtle blueshifts due to the presence of the other isomer. The first two peaks at 1080 cm^{-1} and 1100 cm^{-1} are C$-$F$_{eq}$ and C$-$F$_{ax}$ stretches in the chair molecule. The

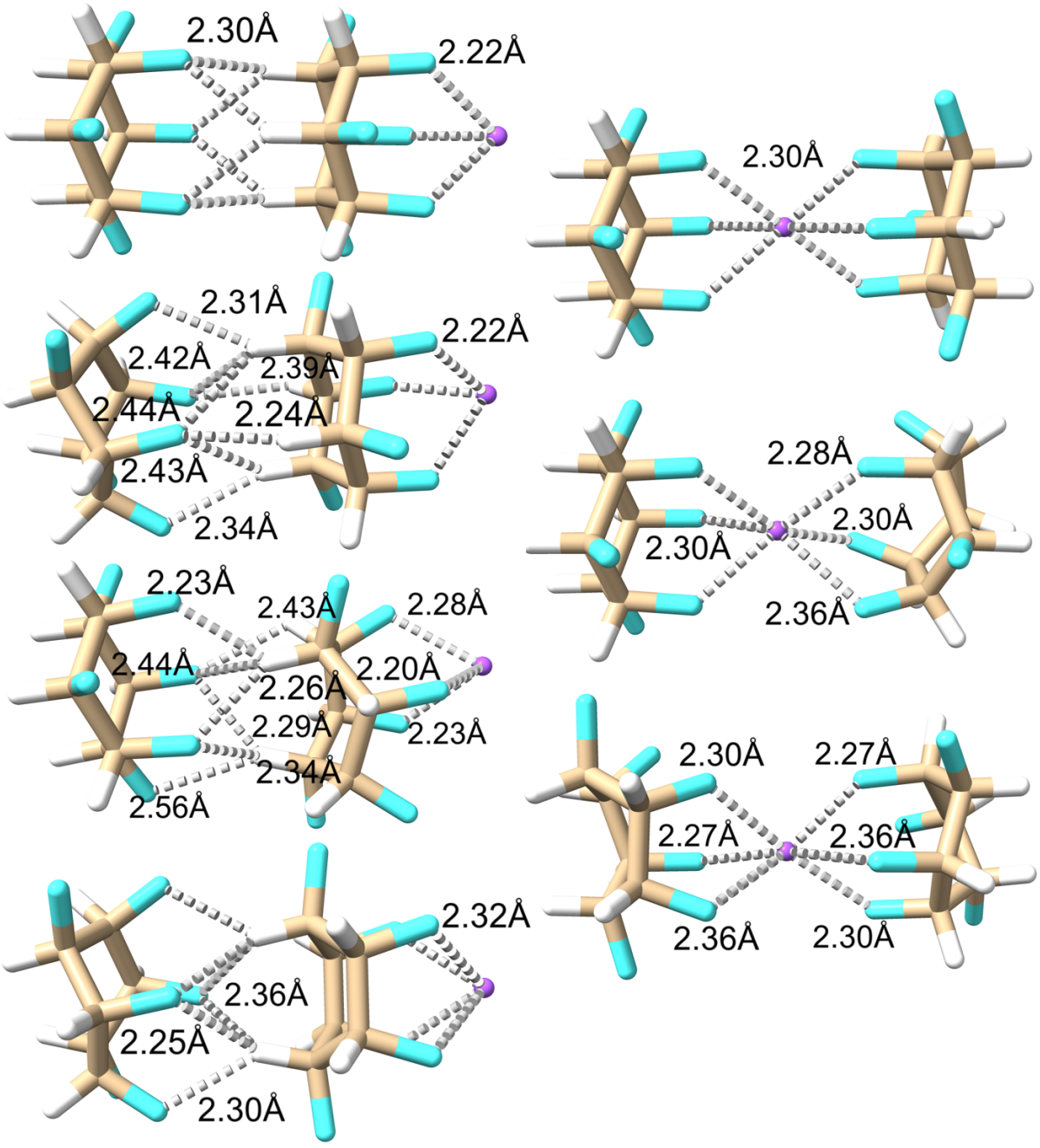

Figure 5.11: Optimized dimer systems for HFCH interacting with a sodium cation. Along the left hand side are the: chair-chair-ion (C-C-I), (twist-boat)-chair-ion (T-C-I), chair-(twist-boat)-ion (C-T-I), and the (twist-boat)-(twist-boat)-ion (T-T-I). Along the right hand side are the: chair-ion-chair (C-I-C), chair-ion-(twist-boat) (C-I-T), and the (twist-boat)-ion-(twist-boat) (T-I-T). It was found that the T-T-I isomer optimized to a (twist-boat)-boat-ion, which did not have imaginary vibrational modes.

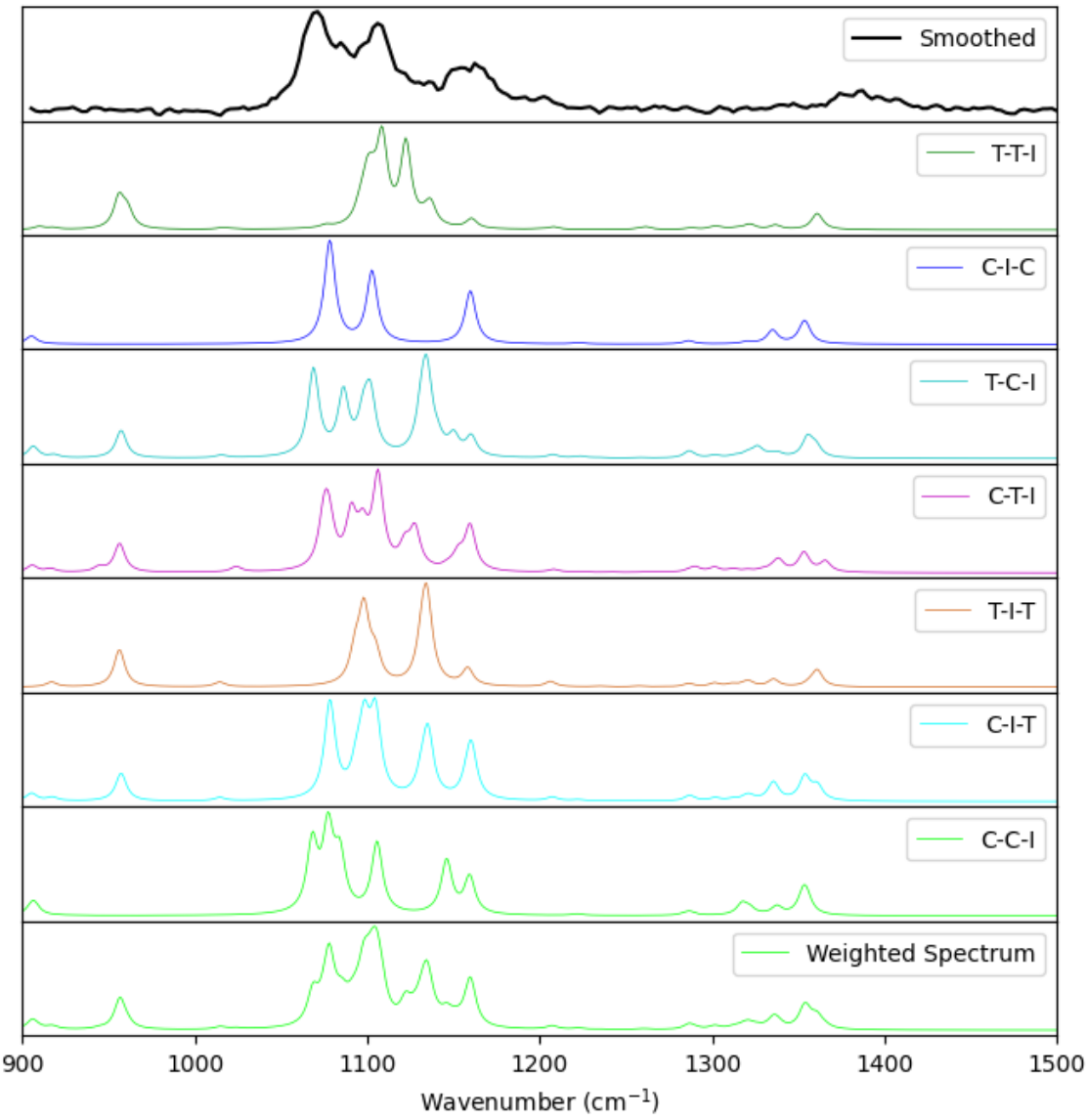

Figure 5.12: A comparison of the experimental smoothed IRMPD spectrum with the chair and twist-boat dimer conformations of HFCH with a caesium ion.

next peak is a combination of both C−F_{eq} and C−F_{ax} stretches at 1115 cm^{-1}corresponding to the twist-boat molecule. The peak at 1150 cm^{-1} is the result of the ring breathing mode in both molecules, followed by a series of peaks resulting from the breathing modes in the chair and twist-boat respectively. In C-T-I we see the opposite of T-C-I, wherein the more pronounced peaks are a result of the twist-boat interacting with the caesium ion, without the presence of blueshifting in the peaks. However, it can be observed that rather than have a combination of breathing modes the intensity is instead split between the twist-boat and chair at 1140 cm^{-1} and 1170 cm^{-1} respectively.

Finally in C-C-I the first peak at 1080 cm^{-1} is an $C-F_{eq}$ stretch of the ion adjacent molecule followed by a $C-F_{eq}$ stretch at 1090 cm^{-1} of the furthest molecule. The shoulder of that peak belongs to the $C-F_{ax}$ stretch of the ion adjacent molecule at 1095 cm^{-1} followed by a $C-F_{ax}$ stretch at 1120 cm^{-1} of the furthest molecule. The last two peaks are ring breathing modes of the ion adjacent molecule and furthest molecule at 1160 cm^{-1} and 1170 cm^{-1} respectively.

In the C-I-C isomer we see vibrational modes identical to that of the monomer chair system. The peaks in the spectrum at 1090 cm^{-1} 1110 cm^{-1} and 1170 cm^{-1} are $C-F_{eq}$, $C-F_{ax}$, and ring breathing modes respectively. T-I-T is similar to C-I-C in that it is a replica of the monomer spectrum with more pronounced modes, being a combination of both $C-F_{eq}$ and $C-F_{ax}$ stretches at 1115 $cm^{-1}$and 1150 cm^{-1}. C-I-T is unsurprisingly a very clean combination of the chair and twist-boat spectra. Each molecule is able to interact with the caesium ion uninterrupted. The peak around 1110 cm^{-1} is a combination of the $C-F_{ax}$ stretches of the chair with the combination stretches of the twist-boat.

Employing the same analysis used on the monomer species, a comparison of the weighted spectrum of all dimer isomers is used to simplify the comparison to the experimental spectra, as seen in **Figure 5.13**. Identical trends to the monomer species are seen in which the cationic species show excellent agreement with the experiment and the peaks of the experimental anion spectra are significantly broader than that of the computational. However, in the fluorine dimer spectrum there is an unexplained peak around 1200 cm^{-1}, which is not readily explained by the dimer species observed for all ions. As previously explained, the ESI conditions increased the effective ion temperatures significantly enough that it is hypothesized that the fluorine monomer was able to undergo a hydrogen abstraction. Taking a closer look at the fragmentation pathways of the fluorine dimer supports this notion in which the observed mass of the one of the fragments is 230.8 u, being the mass of an H-F clustered to a fluoride monomer or $HF\cdots F^{-}\cdots HFCH$.

Examining the energetics shows that the the ionic species readily form a sandwich dimer complex with the chair isomer to form the C-I-C isomer, as seen in **Table 5.6**, . The enthalpy change to form the dimer from the monomer systems is approximately 100 kJ mol^{-1}, showing a strong likelihood that the monomer would react with free HFCH under spray conditions to form dimer complexes.

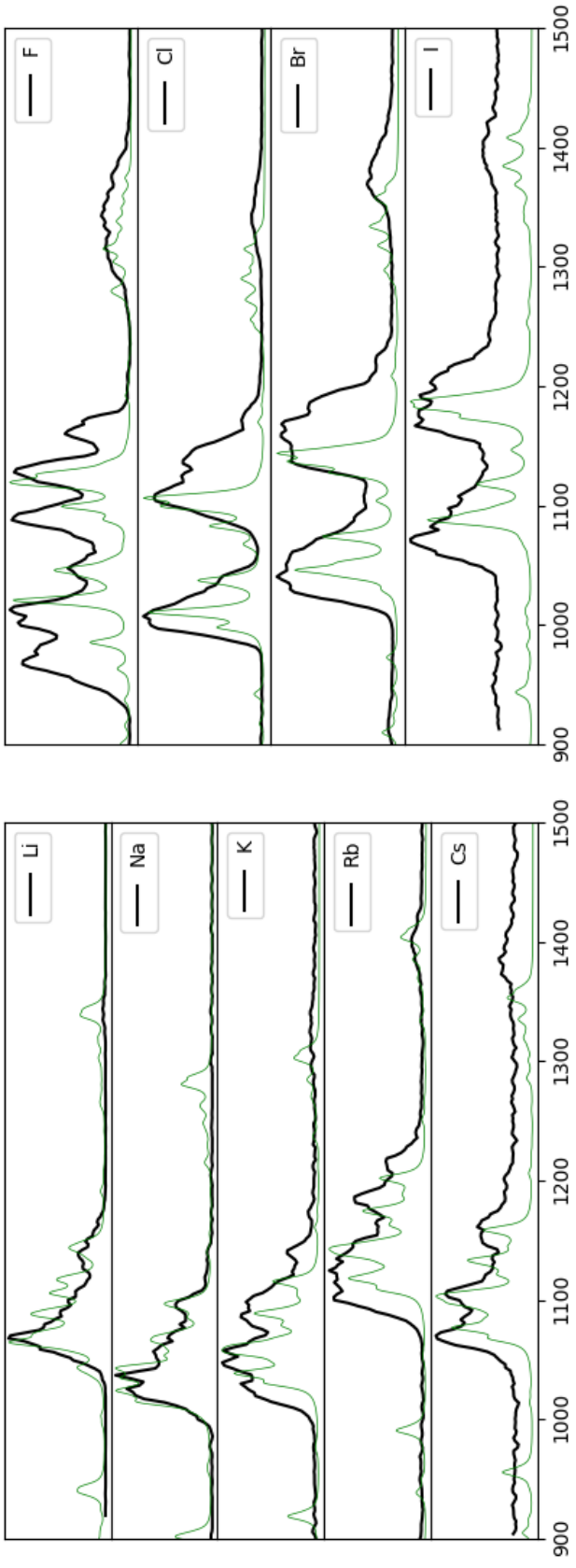

Figure 5.13: A comparison of the experimental smoothed IRMPD spectrum with the weighted computational spectra for all dimer conformations of HFCH.

Table 5.6: Calculated energies (kJ mol^{-1}) for binding ionic species in dimer systems for the lowest energy isomer (C-I-C), using M06-2X with GD3 dispersion corrections at 298 K.

Ion	Electronic	Enthalpy	Free Energy	Entropy (J/Mol-Kelvin)
Li	−384.55	−389.51	−308.65	−271.24
Na	−293.86	−298.82	−228.18	−236.93
K	−229.16	−234.13	−163.18	−237.96
Rb	−208.05	−213.01	−148.69	−215.74
Cs	−189.88	−194.84	−126.51	−229.21
F	−362.12	−367.09	−299.26	−227.50
Cl	−243.91	−248.88	−186.12	−210.50
Br	−222.64	−227.60	−165.17	−209.41
I	−198.51	−203.47	−146.19	−192.12

While not as significant as the sandwich dimer systems, the lowest energy dipole dimer system, C-C-I, still has a significant binding affinity for ionic species, as seen in **Table 5.7**. However, the enthalpy of formation is significantly higher for these systems, being approximately 200 kJ mol^{-1}. This suggests that there should be some population of the C-C-I isomer experimentally under conditions permitting the initial formation of the dipole dimer, which would result in broad peaks in experimental spectra for dimer systems.

Table 5.7: Calculated energies (kJ mol^{-1}) for binding ionic species in dipole dimer systems for the lowest energy isomer (C-C-I), using M06-2X with GD3 dispersion corrections at 298 K.

Ion	Electronic	Enthalpy	Free Energy	Entropy
Li	−326.72	−331.68	−248.29	−279.68
Na	−255.85	−260.81	−180.62	−268.94
K	−210.1	−215.06	−136.51	−263.47
Rb	−195.69	−200.65	−121.4	−265.81
Cs	−183.97	−188.93	−113.17	−254.11
F	−321.37	−326.33	−249.76	−256.82
Cl	−226.64	−231.60	−156.93	−250.47
Br	−211.06	−216.02	−144.01	−241.55
I	−193.39	−198.35	−125.21	−245.31

While most of the ionic species examined in experimental spectra from 2015 consist of a number of very broad peaks, lithium has a relatively simple spectrum with few peaks in comparison to the others. This can be explained by looking at the relative energies for binding ionic species with the dimer systems, as seen in **Figure 5.14**. As ions increase in ionic radii, the gap in binding affinities for ionic species decreases, increasing the likelihood of these species being seen experimentally. As previously mentioned, exposure to high temperature spray conditions permits the formation

of otherwise energetically unfavourable systems. This highlights the importance of recognising and reporting spray conditions, such that spectra are consistent, as can be seen when looking at a comparison of dimer spectra captured in 2015 and 2018 for fluoride dimer systems.

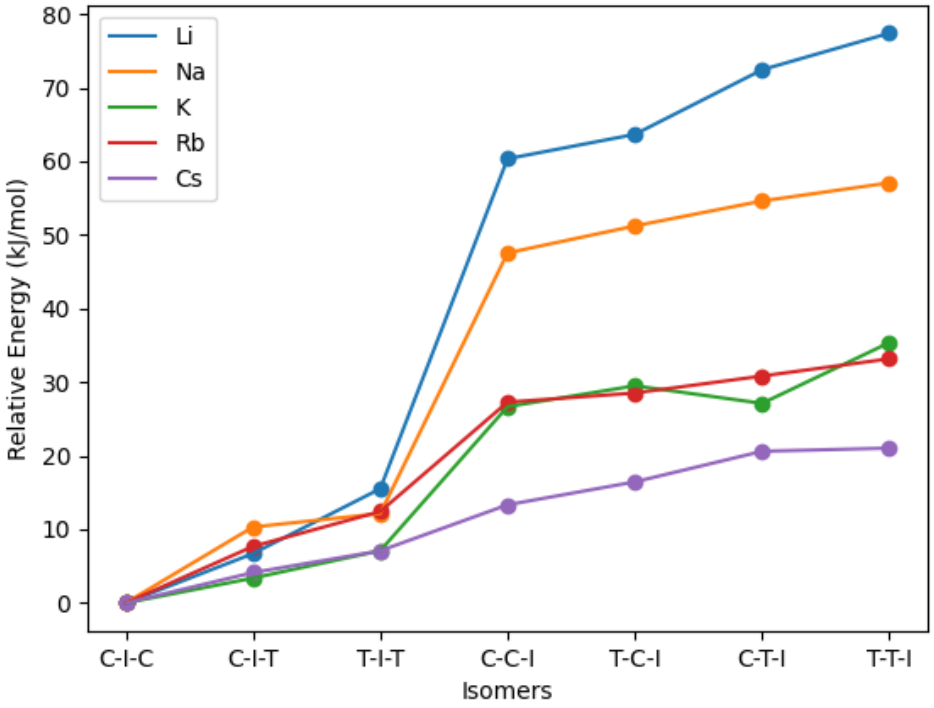

Figure 5.14: A comparison of the binding affinities for the chair and twist-boat dimer conformations of HFCH with a cationic species.

When comparing spectra between years it can be observed that the spectrum for 2018 is considerably less populated than that of 2015. Comparing the computational spectra to the experimental spectrum from 2015, it is quite apparent that the lowest energy dimer systems, as identified in **Figure 5.14**, may all be present, whereas the spectrum from 2018 appears to primarily consist of the C-I-C isomer with some presence of C-I-T and T-I-T in shoulder peaks. This indicates that the spray conditions for 2018 were likely significantly less energetic and thus not readily permitting the transition of chair to twist-boat or formation of dipole bound dimers, producing an environment only permitting lower energy species. This phenomenon would explain the presence of the fluoride monomer system in 2018, where the system was not given sufficient energy from the ESI conditions to abstract a hydrogen atom from the fluoride.

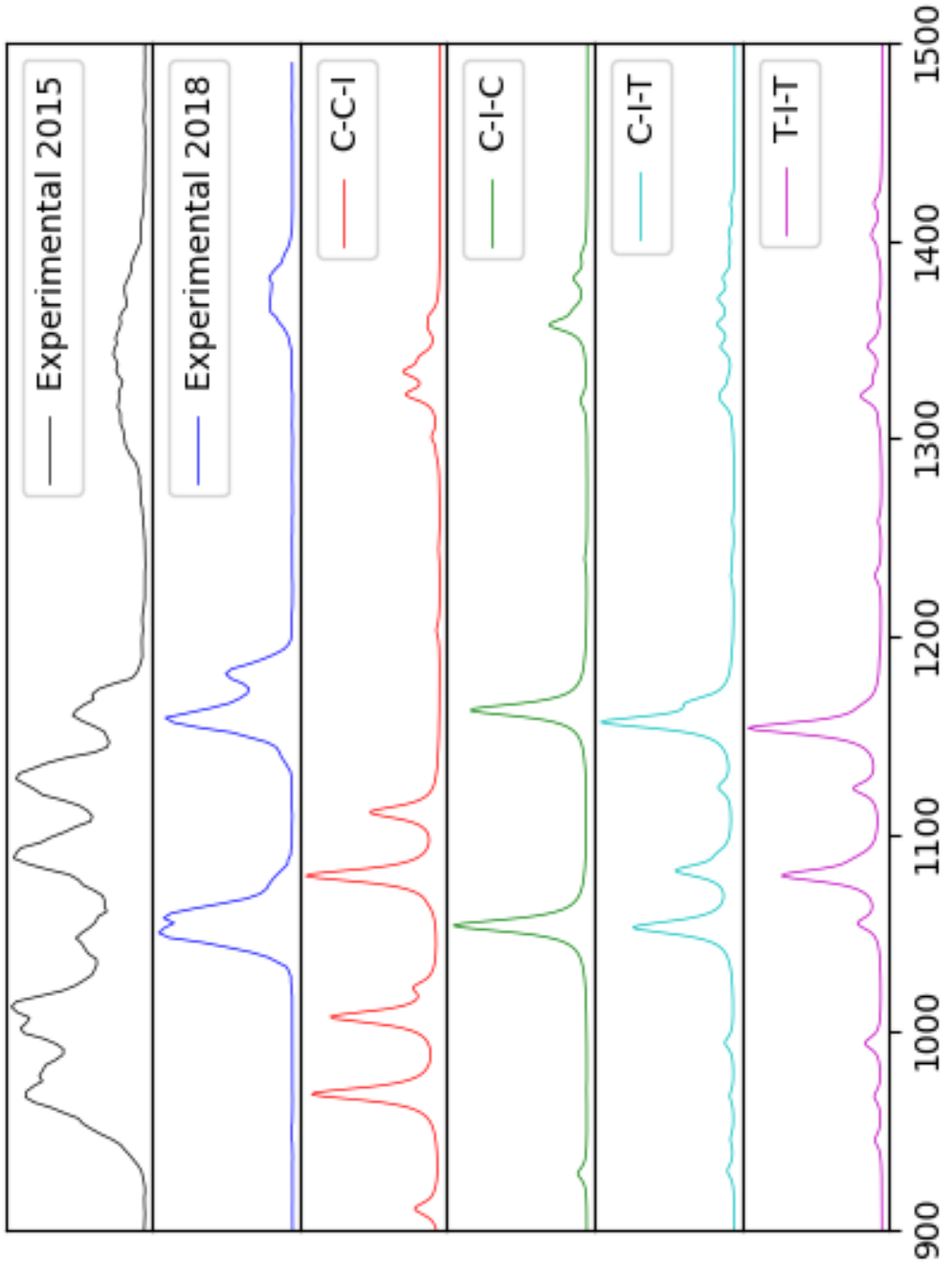

Figure 5.15: A comparison of the experimental smoothed IRMPD spectrum with the chair and twist-boat dimer conformations of HFCH with a fluoride ion.

5.5 Conclusion

All-cis hexafluorocyclohexane has shown an significant propensity for binding both cationic and anionic species. A study using multiple DFT methods highlighted the importance of selecting a method developed for the system in mind. HFCH has been found to be among the strongest molecular entities for binding ionic species as a monomer system and was found to have equally favourable binding in dimer systems, where a number of possible isomers exist.

A study of the experimental IRMPD spectra revealed the importance of maintaining consistent ESI conditions. Experimental spectra captured in 2015 found a number of possible dimer systems, while those in 2018 found only the lowest energy species. This suggests that the conditions of the instrument may have a stronger influence on the spectrum of a species than previously indicated.

Chapter 6

The structure and properties of ionic all-cis pentafluorocyclohexanol and all-cis hexa-trifluoromethyl-cyclohexane complexes

6.1 Introduction

Expanding on the original synthesis of all-cis 1,2,3,4,5,6-hexafluorocyclohexane (HFCH), the O'Hagan group at the University of St. Andrews in the United Kingdom, has successfully modified intermediate species to synthesize all-cis 1,2,3,4,5,6-pentafluorocyclohexanol (PFCHOL) and all-cis 1,2,3,4,5,6-hexa-trifluoromethyl-cyclohexane (HTFMCH).[147] These two derivative products share many of the unique properties of HFCH, in particular being facially polarized, allowing for the binding of both cationic and anionic species. However, the strength of the dipole moment is substantially weakened by substitutions, as shown in **Figure 6.1**.

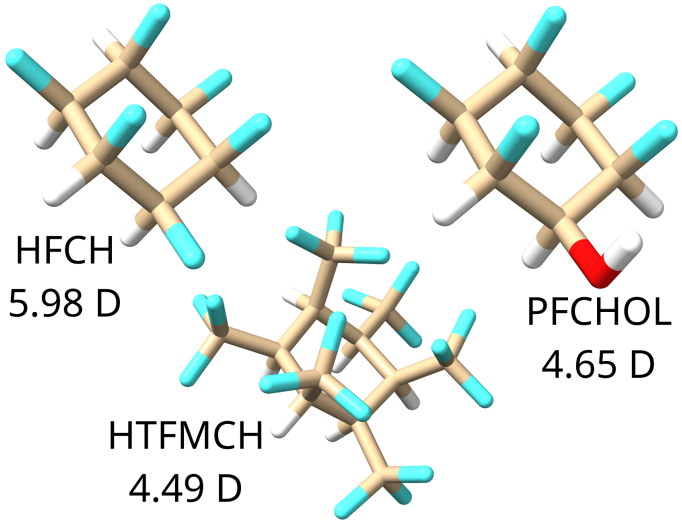

Figure 6.1: The optimized structrues of HFCH, PFCHOL, and HTFMCH. The substitution of a single fluorine to a hydroxyl group substantially weakens the dipole. The dipole moment for all molecules is parallel to the $C-H_{ax}$ bonds starting at the center of the ring on the hydrogen face.

Although the dipole moment is weaker, the substitutions lend themselves to more distinct binding motifs and charge distributions. An examination of partial charges, as shown in **Figure 6.2**, illustrates the shift of charge density throughout the molecules, where the hydrogen face is substantially more charged in the HTFMCH than HFCH suggesting that the species may possess stronger binding affinities for anionic species.

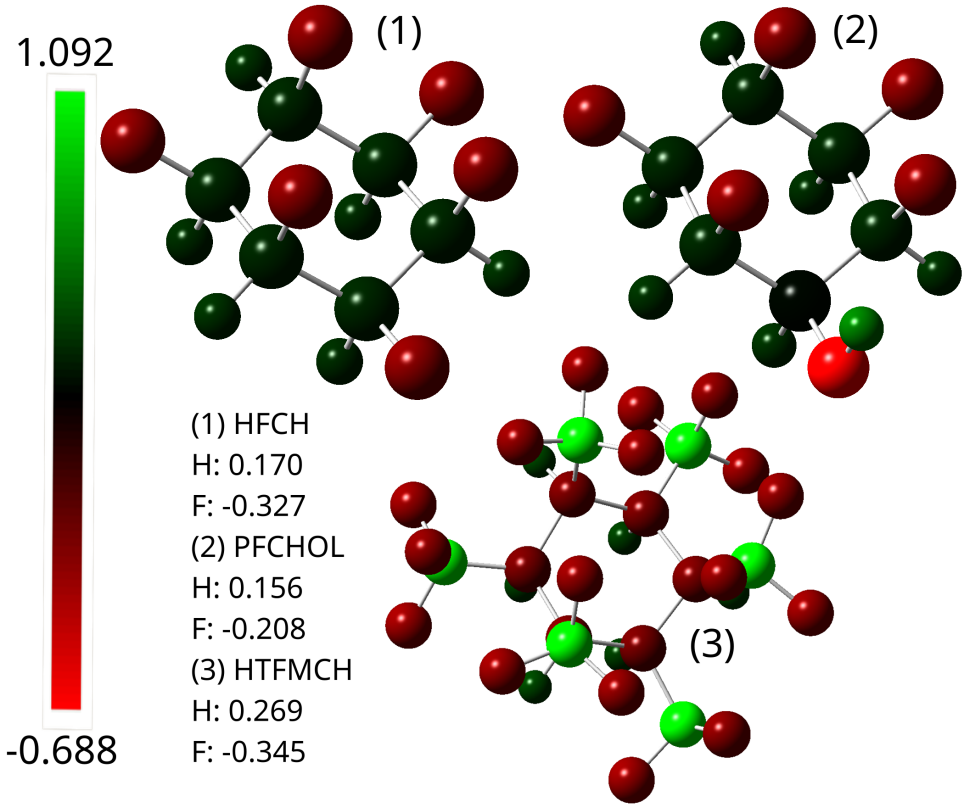

Figure 6.2: Evaluation of charge using the natural bond orbital 6th edition (NBO6) method. The avergae partial charge for each polarized face is listed to assist in evaluating charge distributions.

These molecules are of importance to study as modifying the ability for small molecules to act as ion transport systems may prove invaluable in a number of areas of chemistry.[173–176] HFCH was found to have a significant propensity for binding cationic species, with binding enthalpies only exceeded by appreciably larger cyclic polyethers such as crown ethers and other cryptands.[27–29] Therefore, by modifying the binding affinity and binding motif of HFCH, potential applications throughout chemistry for this family of substituted cyclohexanes becomes significantly larger.

6.2 Experimental

All infrared multiple photon dissociation (IRMPD) spectra were acquired at the Centre de Laser Infrarouge d'Orsay (CLIO) free electron laser (FEL) facility at the university of Paris XI.[81,151] Ionic clusters of PFCHOL were generated by use of electrospray ionisation (ESI) where 100 μM solutions of PFCHOL in water/methanol (50/50 vol%) containing ratios of 1:5 to 1:3 of ionic salts to PFCHOL. A Bruker Esquire 3000+ ion trap mass spectrometer was used to mass select ionic clusters which were then subsequently irradiated by the wavelength tunable output of the FEL. The clusters were examined across the 850-1800 cm^{-1} range at 5 cm^{-1} intervals for periods of 400 ms. This produced a series of vibrational spectra obtained from the fragmentation efficiency of depletion of the ionic PFCHOL cluster species as a function of wavenumber. Additional details of the experimental apparatus and IRMPD process have been previously described.[49,152]

6.3 Computational methods

Following the methodology employed to study all-cis hexafluorocyclohexane, PFCHOL was studied using the single point and thermochemical values calculated using the Minnesota 06-2X (M06-2X) density functional theory (DFT) method employing Grimme Dispersion 3 (GD3) dispersion corrections. This method was initially selected for it's accuracy in calculating fluorocarbon compounds.[51–54] It was found to be able to accurately calculate electronic and thermochemical corrections within 3 kJ mol^{-1} of the Møller–Plesset perturbation theory second order (MP2) level of theory.

The basis sets selected were chosen in an attempt to produce the most computationally reasonable binding energies. All carbon and hydrogen atoms were subject to the def2-tzvp basis set for optimizations and vibrational frequencies as it had previously provided good agreement with experimental spectra, while being relatively computationally inexpensive.[129,161,162] This basis was expanded to include fluroine atoms, not including anionic fluorine, to reduce the overall computational runtime. The sodium and lithium cationic species were treated using the aug-cc-pCVTZ basis set due to accuracy in both energetics and agreement seen in previous comparisons to IRMPD.[50,163,164] All other ionic species were run using the def2-tzvppd basis set to minimize the root mean square difference (RMSD) of the zero-point vibrational energy

(ZPVE).[165] Basis set data for def2-tzvppd was obtained from the basis set exchange (BSE) and all calculations were run using the Gaussian 16 revision C.01 computational suite.[95,166] Thermochemical scaling factors were found to be significantly variable with multiple sources reporting scaling factors in the range of 0.92-0.97%.[165,167,168] Charges were evaluated using the NBO6 software package integrated with Gaussian 16 using M06-2X and the provided basis sets.[177] All structure graphics were generated using the ChimeraX package.[139,140]

6.4 Geometric and Vibrational Analysis of all-cis pentafluorocyclohexanol

The spectra obtained for ionic complexes of PFCHOL are shown in **Figure 6.4**. Anionic species were found to contain an initially unexplained peak around 1080 $cm^{-1}$and 1100 cm^{-1}in the monomer species and 1100 $cm^{-1}$and 1120 cm^{-1}in the dimer species for fluoride and chloride respectively. This vibrational mode can be attributed to a second binding motif with the side of the ring, resulting from the interaction of the hydroxyl hydrogen and two hydrogens on the ring face. A comparison of the three binding motifs of PFCHOL is shown in **Figure 6.3**, where the face centred interactions are slightly off-axis due to the hydroxyl substitution. Another observed feature was that the vibrational spectra obtained for PFCHOL showed less pronounced blueshifting of peaks with increasing ionic size when compared to the spectra obtained for HFCH.

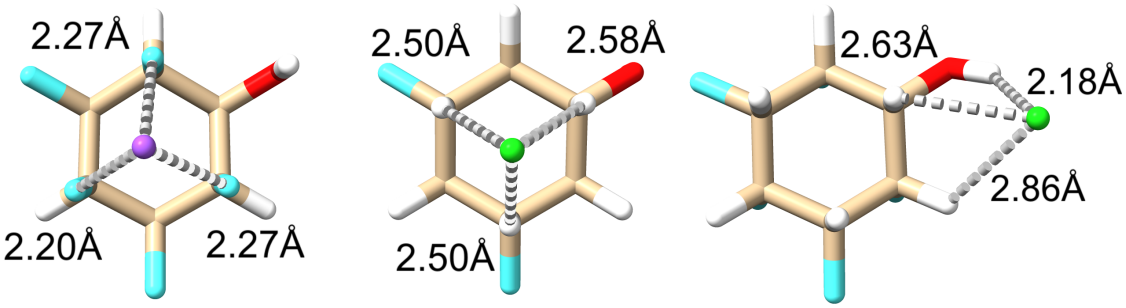

Figure 6.3: The three distinct binding motifs of PFCHOL. with face centred cations (left), face centred anionic (centre), and hydroxyl centred anion (right) interactions.

A weighted spectrum of the two anionic isomers shows excellent agreement when compared to the experimental spectra as shown in **Figure 6.5**. The peaks in the spectrum correspond to the various stretching modes of PFCHOL, with stretching modes in the following order:

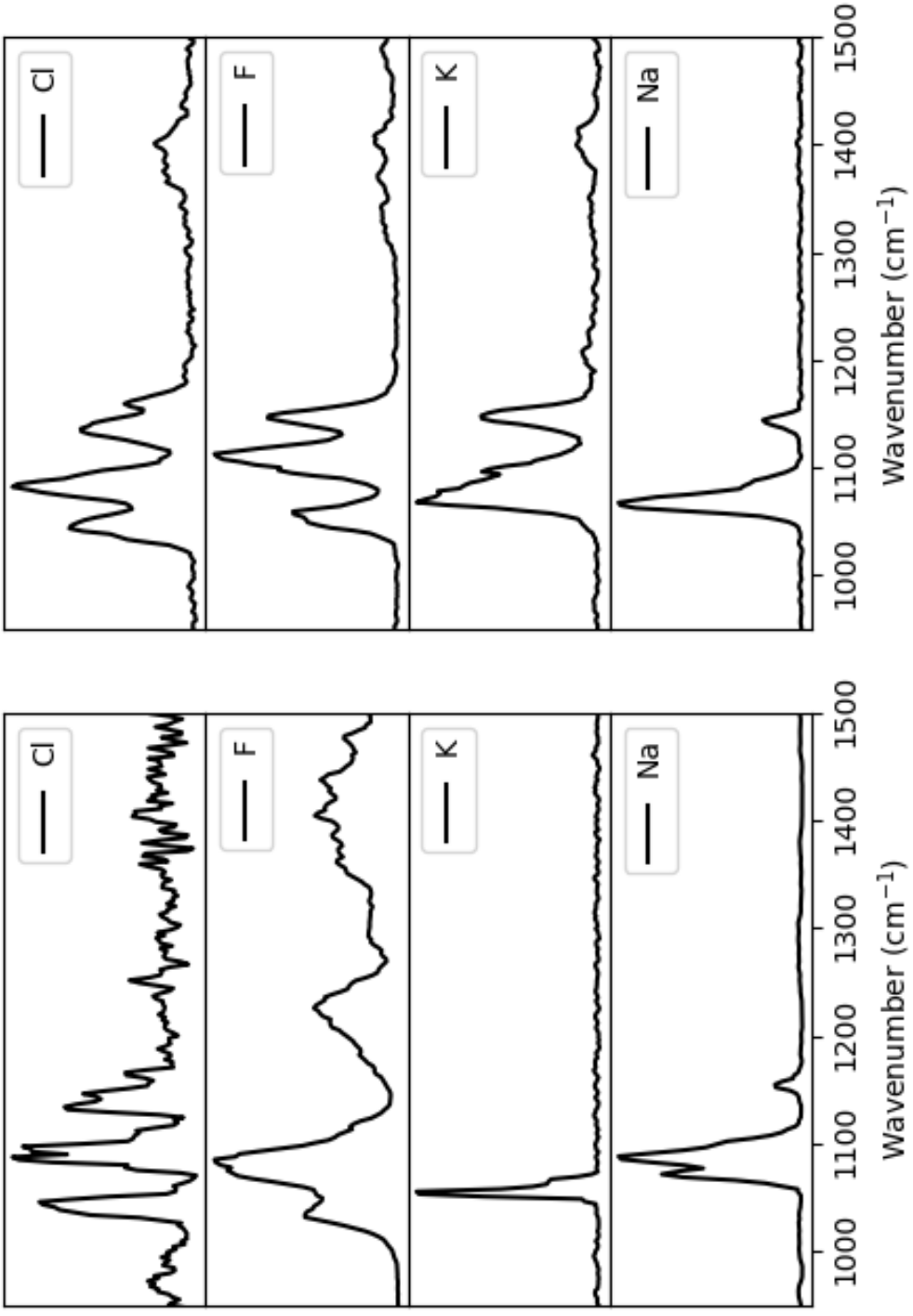

Figure 6.4: Experimental vibration spectra obtained for ionic monomer (left) and dimer (right) systems of PFCHOL.

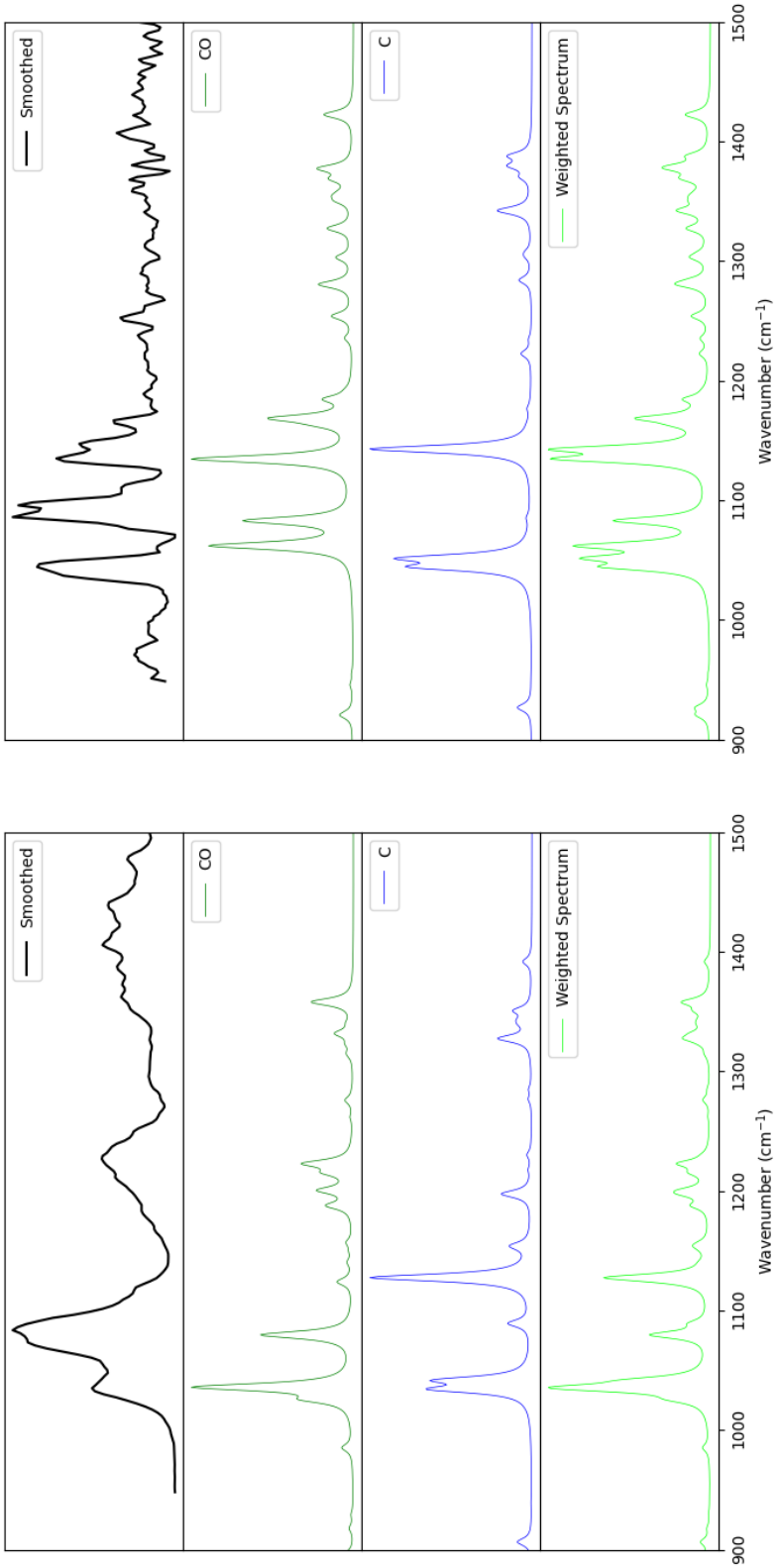

Figure 6.5: A comparison of the experimental vibration spectra obtained for fluoride (left) and chloride (right) monomer systems compared against the two isomers (C=face centred, CO=hydroxyl centred) for anionic species.

C−F_{eq}, C−OH, and C−F_{ax}. In the face centred complexes, the C−F_{eq} and C−OH stretching modes are closer together resulting in a broad or double maximum peak, whereas for the hydroxyl centred complexes, the modes are more separated showing two distinct peaks.

When the binding energy of these systems is considered, as shown in **Table 6.1**, the smaller fluoride anion has a greater binding affinity for the hydroxyl interaction versus the ring centred interaction. This preference is explained by the proximity of the ion to the hydroxyl group, where the fluoride interaction distance, O−H···F, is 1.19 Å compared to the chloride interaction distance, O−H···Cl, of 2.18 Å. Additionally, the fluoride species shows an elongated O-H bond of 1.15 Åcompared to the 0.97 Å of the bare chair molecule. This suggest that the hydrogen is being shared between the oxygen and fluoride. These distances can be compared to the bond lengths of hydrogen halides, with the bond length for H-F and H-Cl being 0.91 Å and 1.28 Å respectively.[28] This illustrates why this interaction is more favourable for fluoride as the distances of these interactions are more similar to covalent bond lengths than the distances of ion dipole interactions.

Table 6.1: Binding energies (kJ mol^{-1}) for PFCHOL monomer ion complexes of face centred (1) and hydroxyl centred (2) isomers calculated using M06-2X with GD3 dispersion corrections.

Ion	Isomer	Electronic	Enthalpy	Free Energy	S (J/Mol-Kelvin)
Na	1	−164.42	−163.68	−129.10	−115.98
K	1	−123.44	−122.80	−90.63	−107.88
F	1	−214.61	−214.11	−183.03	−104.26
F	2	−210.71	−219.26	−189.33	−100.38
Cl	1	−135.14	−134.08	−105.39	−96.22
Cl	2	−120.48	−120.01	−91.27	−96.41

In comparison to the vibrational spectra obtained for HFCH, the simplicity of the vibrational spectra obtained for PFCHOL suggests that only the chair isomer was sampled experimentally. This is supported by a comparison of computational spectra for the chair and twist-boat isomers, where, for cationic species, the twist-boat shows extremely poor agreement with the experimental spectra, as shown in **Figure 6.6**, leading to the weighted spectrum of the two isomers showing extremely poor agreement. Thus, a comparison can be made to the experiment being composed solely of chair isomers for ionic monomer species, as shown in **Figure 6.7**.

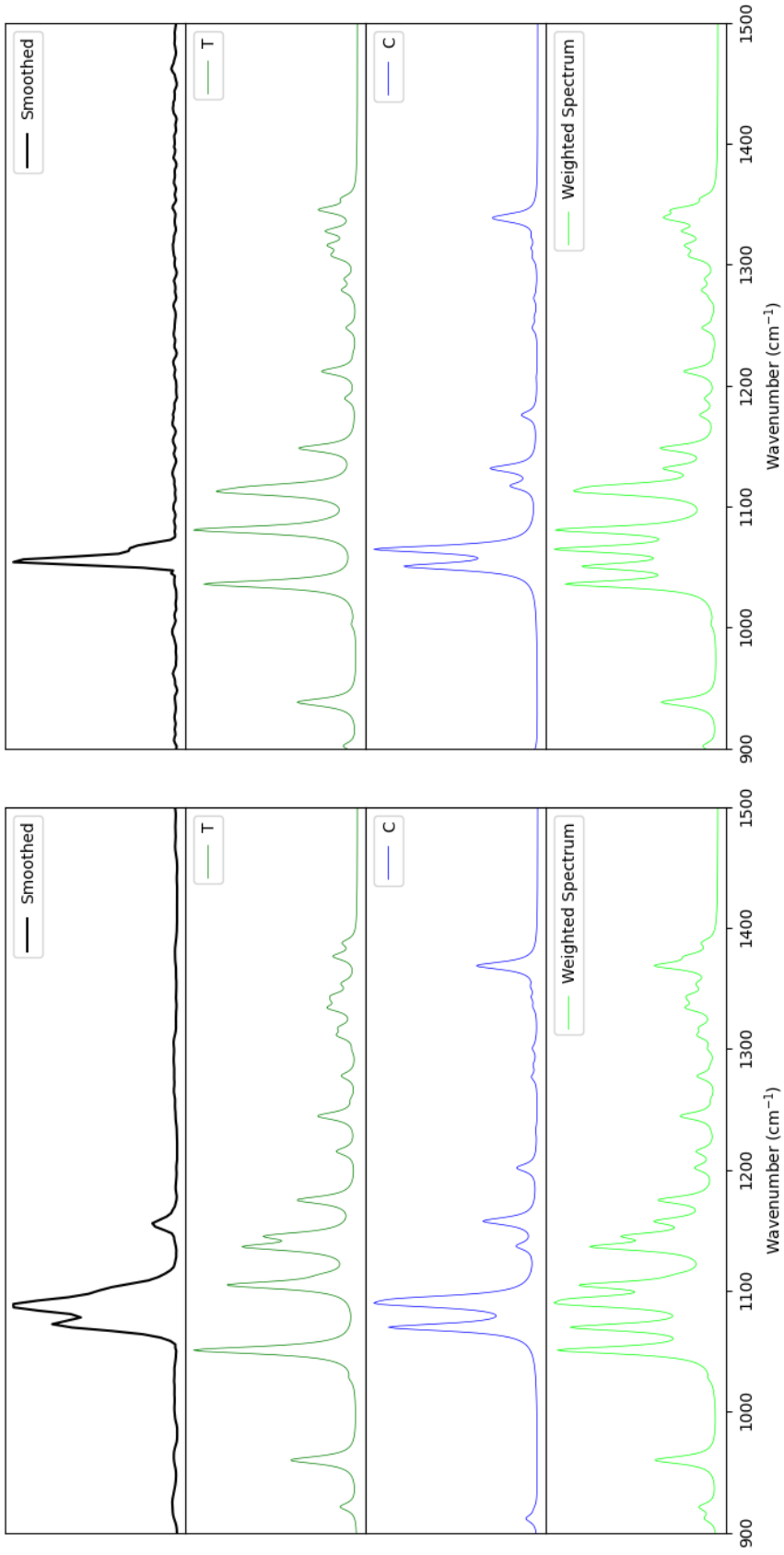

Figure 6.6: A comparison of the experimental vibration spectra obtained for sodium (left) and potassium (right) monomer systems compared against the chair and twist-boat structural isomers of PFCHOL.

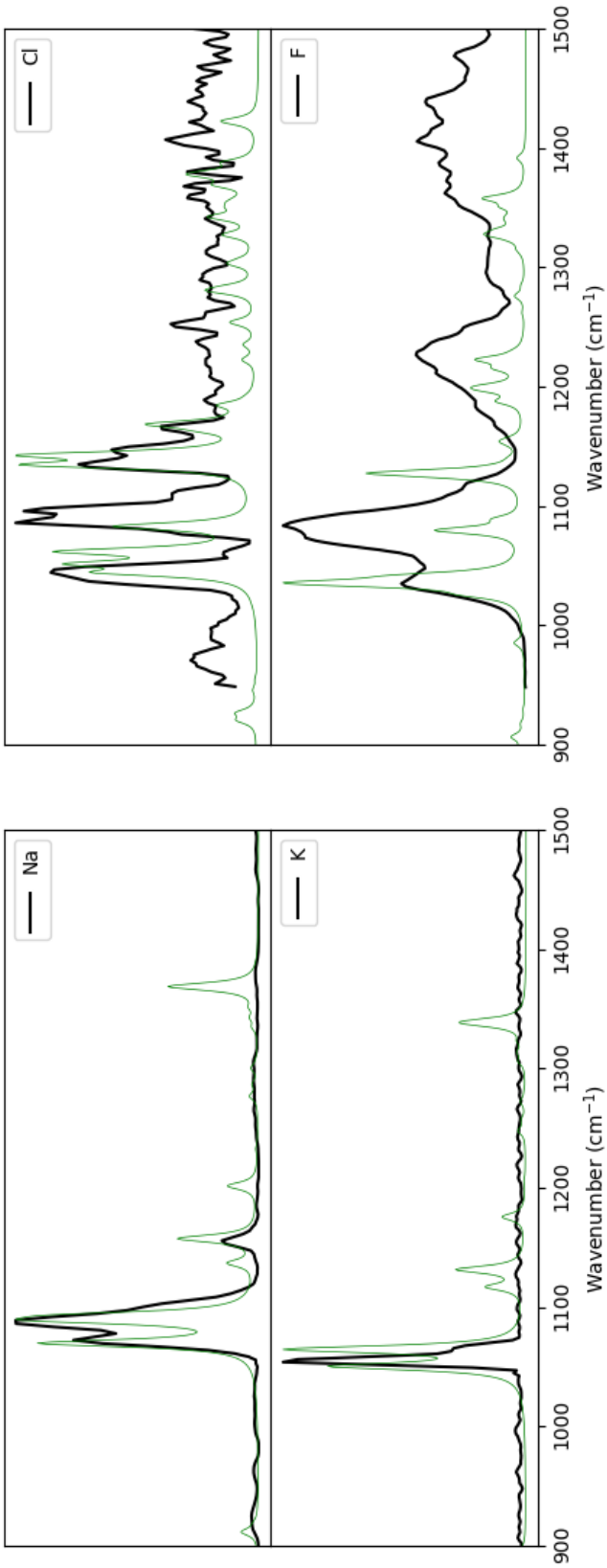

Figure 6.7: A comparison of the experimental vibration spectra obtained for cationic (left) and anionic (right) monomer systems compared against the ion-chair interactions of PFCHOL. The cationic spectra are composed of solely ring centred interactions while the anionic spectra are composed of a weighted spectrum of the ring centred and hydroxyl centred interactions.

Employing the same methodology of analysis to the dimer species, there are two and four possible geometries for the cationic and anionic species respectfully. A comparison of the possible isomers for anionic species is laid out in **Figure 6.8**, where the sandwich chair (isomer 1) and dipole chair (isomer 2) dimers are shared between anionic and cationic species. The other two dimers seen in the anionic complexes are either one (isomer 3) or two (isomer 4) interactions with the hydroxyl group, similar to the monomer species.

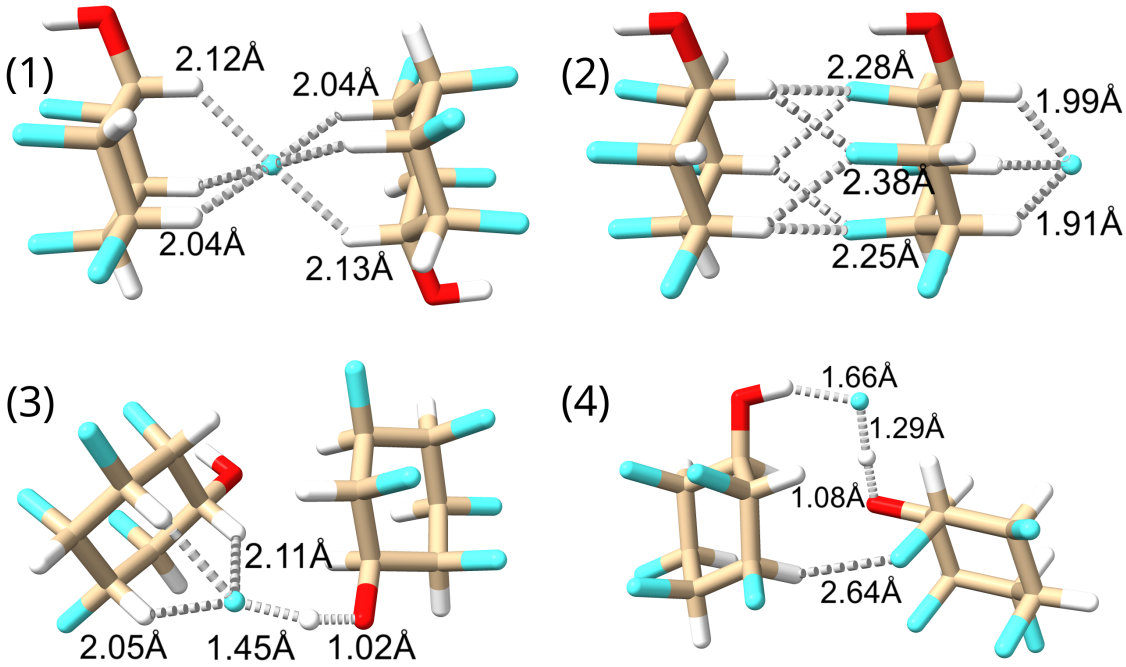

Figure 6.8: The four distinct binding motifs of anionic PFCHOL dimers, with chair sandwich (1), chair dipole (2), hydroxyl-chair sandwich (3), and hydroxyl-hydroxyl sandwich (4). The chair sandwich and dipole dimer are also seen in cationic dimers.

Unlike the monomer systems, the face centred chair sandwich dimer is the most energetically favourable in free energy for all species, as shown in **Table 6.2**. While the enthalpy of formation for both isomers 3 and 4 are more favourable than isomer 1, those systems possess a significant entropy magnitude in comparison, resulting in a less favourable free energy. This barrier was overcome in the monomer system as the proximity of the O−H···F interaction was able to overcome the difference in entropy of 4 J/Mol-Kelvin but in the dimer system the difference is roughly 40 J/Mol-Kelvin.

Table 6.2: Binding energies (kJ mol^{-1}) for PFCHOL dimer ion complexes of: sandwich chair (1), chair dipole (2), sandwich hydroxyl-chair (3) and the sandwich hydroxyl-hydroxyl (4). These isomers were calculated using M06-2X with GD3 dispersion corrections.

Ion	Isomer	Electronic	Enthalpy	Free Energy	S (J/Mol-Kelvin)
Na	1	−298.64	−292.68	−209.42	−279.26
Na	2	−246.80	−240.53	−162.11	−263.01
K	1	−232.19	−226.21	−145.63	−270.27
K	2	−197.40	−191.27	−114.73	−256.73
F	1	−357.50	−350.59	−284.68	−221.05
F	3	−360.49	−356.17	−278.52	−260.43
F	4	−356.02	−354.94	−277.89	−258.41
F	2	−312.22	−306.15	−228.84	−259.27
Cl	1	−238.02	−231.04	−169.32	−207.01
Cl	4	−224.90	−219.46	−148.58	−237.75
Cl	3	−222.77	−218.91	−146.06	−244.33
Cl	2	−217.38	−210.51	−135.70	−250.92

Similarly to the monomer species, the dimer species showed relatively simple vibrational spectra, further supporting the hypothesis that the twist-boat isomer was not present experimentally to any significant extent. A comparison of the four isomers of the anionic dimers is shown in **Figure 6.9**, where the weighted spectrum shows excellent agreement with the experimental spectrum. The weighted spectrum of isomers 1 and 2 for the cationic species also showed excellent agreement to the experiment, as shown in **Figure 6.12**. The dimer system show identical modes to the monomer species with a slight blueshift of peak location. The peaks in the spectrum correspond to the various stretching modes of PFCHOL, with stretching modes in the following order: C−F_{eq}, C−OH, and C−F_{ax}. Each dimer shows some variation in the spacing between peaks, with isomer 1 showing perfect overlap of the modes for the two molecules and isomer 4 showing the most separation between the modes of the two molecules.

While not studied in the current work, it would have been interesting to examine the propensity of this species for molecules that can hydrogen bond. The introduction of the hydroxyl group introduces new possibilities for stabilizing a network with both ionic and hydrogen bonding interactions. This could potentially prove useful in a number of biological systems where hydrogen bonding and ionic interactions are commonly seen.[1,2,6–8]

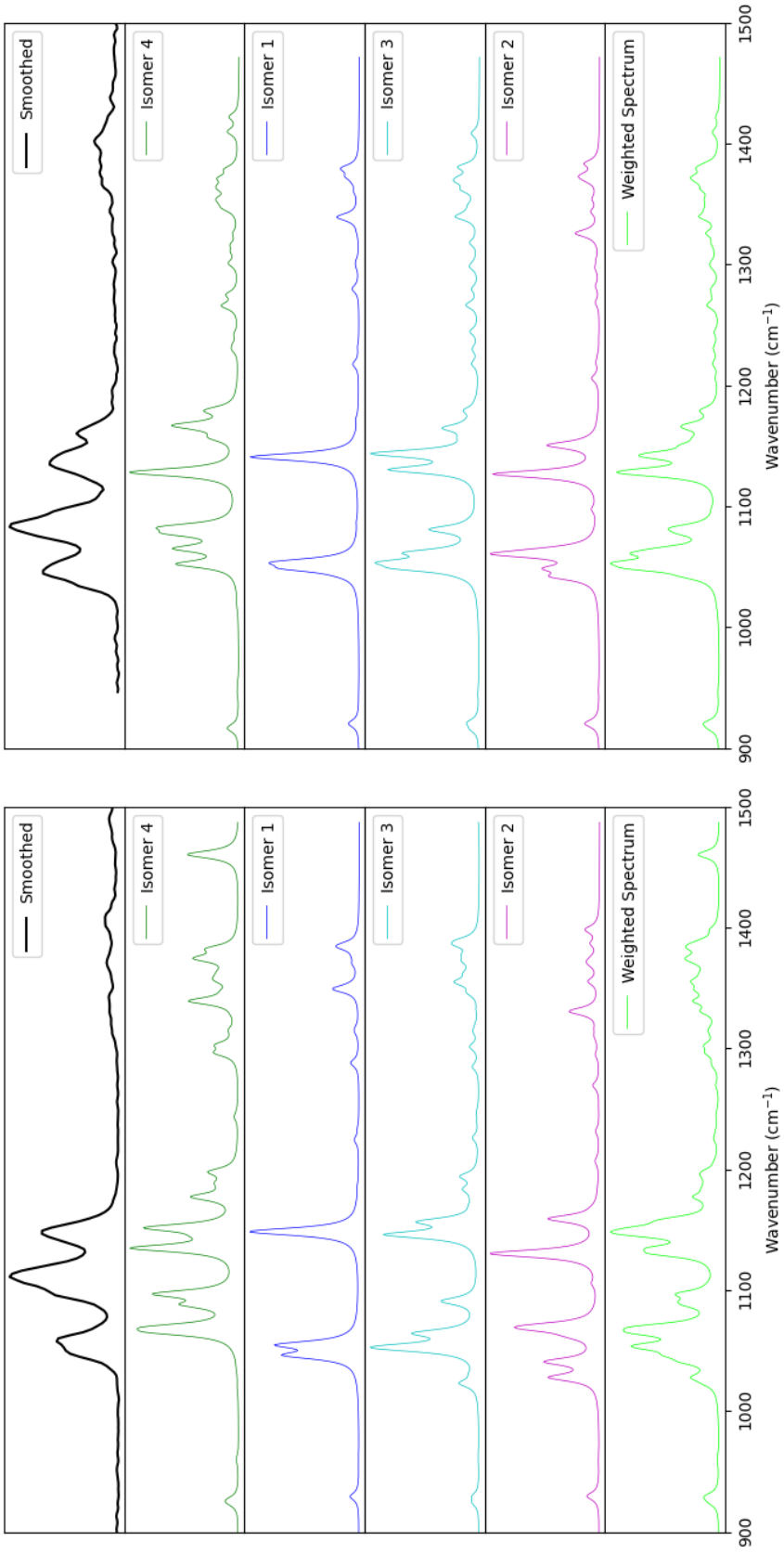

Figure 6.9: A comparison of the experimental vibrational spectra obtained for fluoride (left) and chloride (right) dimer systems compared against the various isomers of PFCHOL.

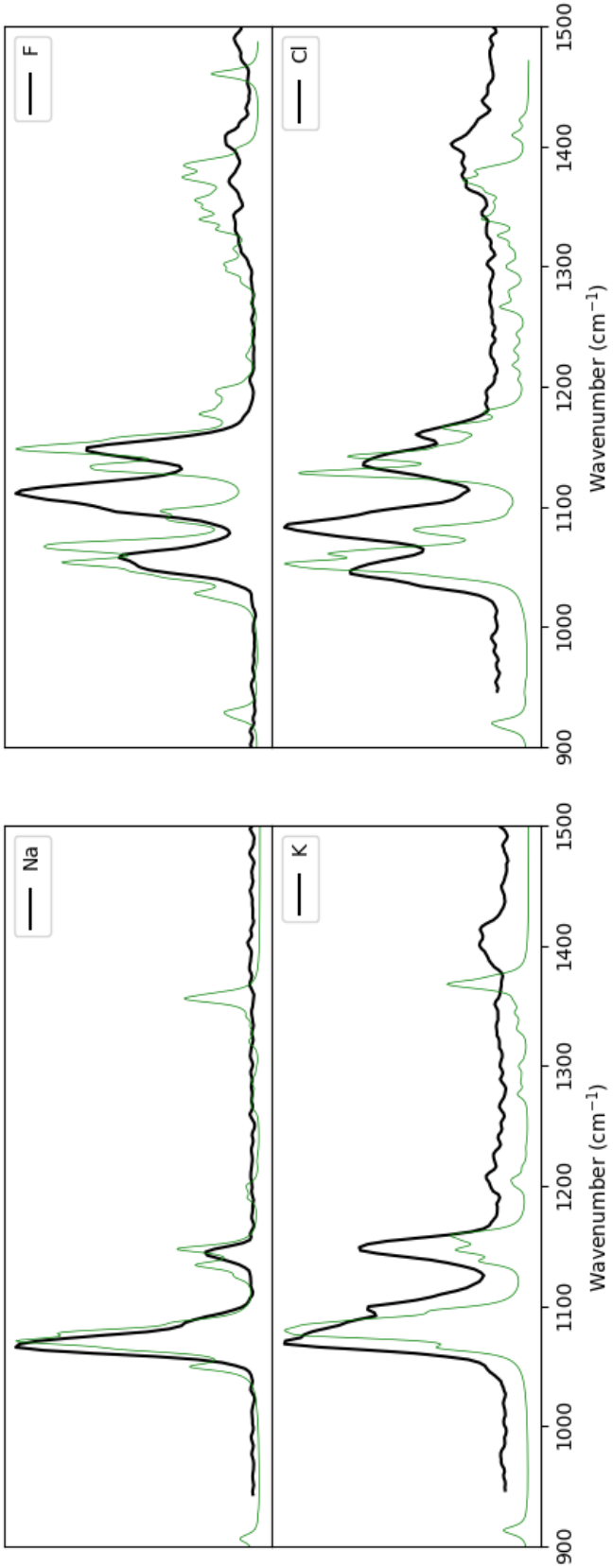

Figure 6.10: A comparison of the experimental vibrational spectra obtained for cationic (left) and anionic (right) dimer systems compared against the calculated weighted dimer spectra for PFCHOL.

6.5 Geometric Analysis of all-cis hexa-trifluoromethyl-cyclohexane

Due to unforeseen circumstances, the experimental spectra for complexes of HTFMCH are yet to be obtained. An analysis using conventional mass spectrometry (MS) confirmed that the monomeric complexes were attainable under ESI conditions. Following the methodology employed to study PFCHOL, the assumption was made that experimentally only the chair isomer would be observed.

Similarly to that found for PFCHOL, HTFMCH shows the rise of a new binding motif for ionic species. Substitution of the fluorine face by trifluoromethyl groups, introduces an increased surface area for interaction, allowing cationic species to interact with two sites, as shown in **Figure 6.11**. The new binding motif (isomer 2), is a methyl centred interaction, in which the cationic species rest between three trifluoromethyl groups on the ring face.

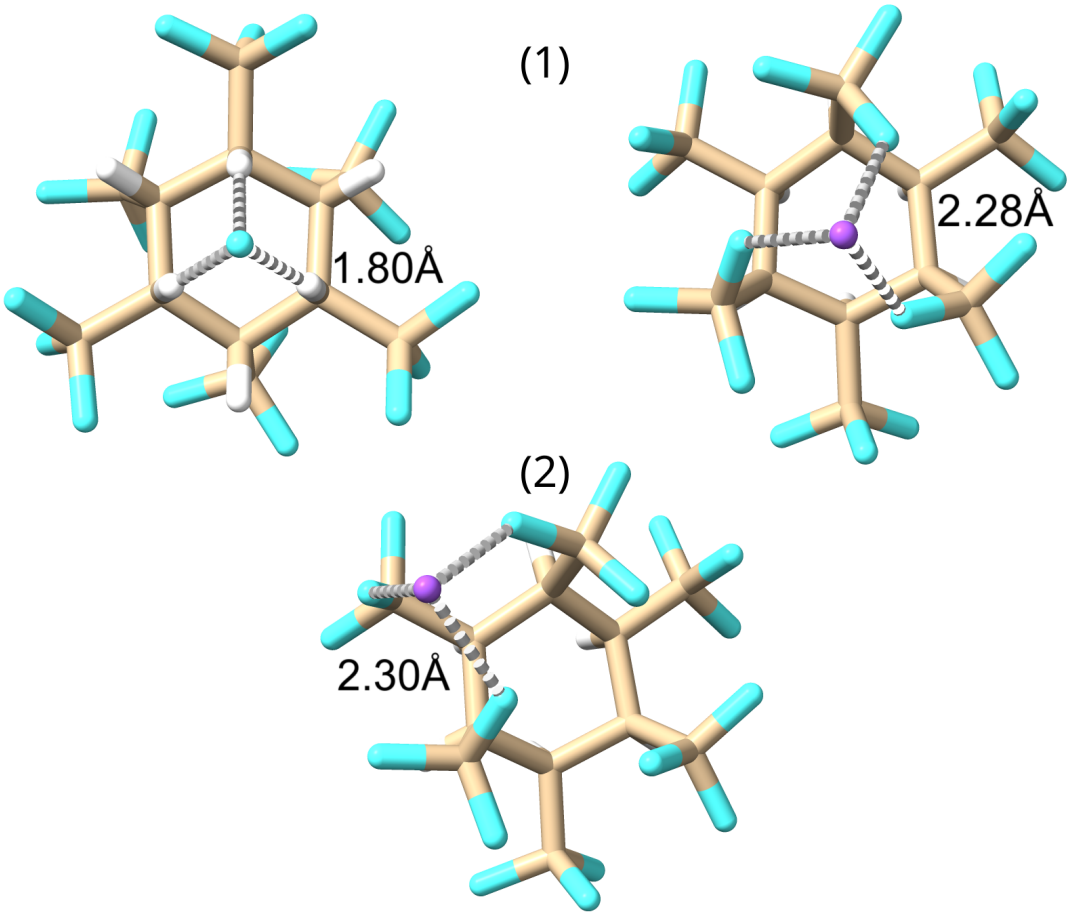

Figure 6.11: The binding motifs of fluoride (ring centred - left) and sodium (ring centred - right, methyl centred - bottom) monomer complexes of (HTFMCH.

Even though the ion interaction in isomer 2 is off axis of the ring centred dipole, the interaction is nearly as favourable to that of isomer 1, as shown in **Table 6.3**. This strongly suggests that both motifs would be present experimentally resulting in a spectrum with broad peaks due to the overlap of the two motifs for cationic species. This could prove problematic for comparison to calculated spectra as a weighted spectrum of these two motifs shows the complexity of this species, as shown for the sodium ion complex in **Figure 6.12**. This problem arises from the significant number of modes present in this species. In this species there are C−C_{eq}, C−C_{ax}, C−H_{eq}, C−H_{ax}, and C−F stretching modes, C−H_{wag} modes, and ring breathing modes that add complexity to the spectrum. Should experimental conditions permit the conversion to the twist-boat, the resulting raw spectrum may consist of very broad peaks with poor resolution from $\sim$ 1050 cm^{-1} to $\sim$ 1400 cm^{-1}.

Table 6.3: Binding energies (kJ mol^{-1}) for HTFMCH monomer ion complexes of: ring centred chair (1) and methyl centred chair (2) interactions. These isomers were calculated using M06-2X with GD3 dispersion corrections.

Ion	Isomer	Electronic	Enthalpy	Free Energy	S (J/Mol-Kelvin)
Li	1	−170.52	−169.00	−131.62	−125.37
Na	1	−114.65	−114.12	−79.57	−115.88
K	1	−83.67	−83.12	−50.71	−108.70
Rb	1	−74.49	−74.05	−44.42	−99.38
Cs	1	−67.49	−67.00	−37.27	−99.71
Li	2	−164.66	−163.27	−127.15	−121.16
Na	2	−110.29	−109.85	−77.11	−109.80
K	2	−80.20	−79.59	−49.20	−101.92
Rb	2	−71.35	−70.90	−42.15	−96.42
Cs	2	−64.55	−63.99	−34.77	−97.99
Cl	1	−184.84	−185.79	−156.25	−99.08
Br	1	−168.38	−169.13	−139.79	−98.42
I	1	−150.61	−151.34	−122.67	−96.14

A comparison to the other species shows that HTFMCH has the highest propensity for anionic species, with the free energy for chloride being -116.61 kJ mol^{-1} -105.39 kJ mol^{-1} and -156.25 kJ mol^{-1}, for HFCH, PFCHOL, and HTFMCH respectively. However this species pales in comparison to the other species for cationic species, with the free energy for sodium being -137.82 kJ mol^{-1}, -105.39 kJ mol^{-1}, and -79.57 kJ mol^{-1}, for HFCH, PFCHOL, and HTFMCH respectively.

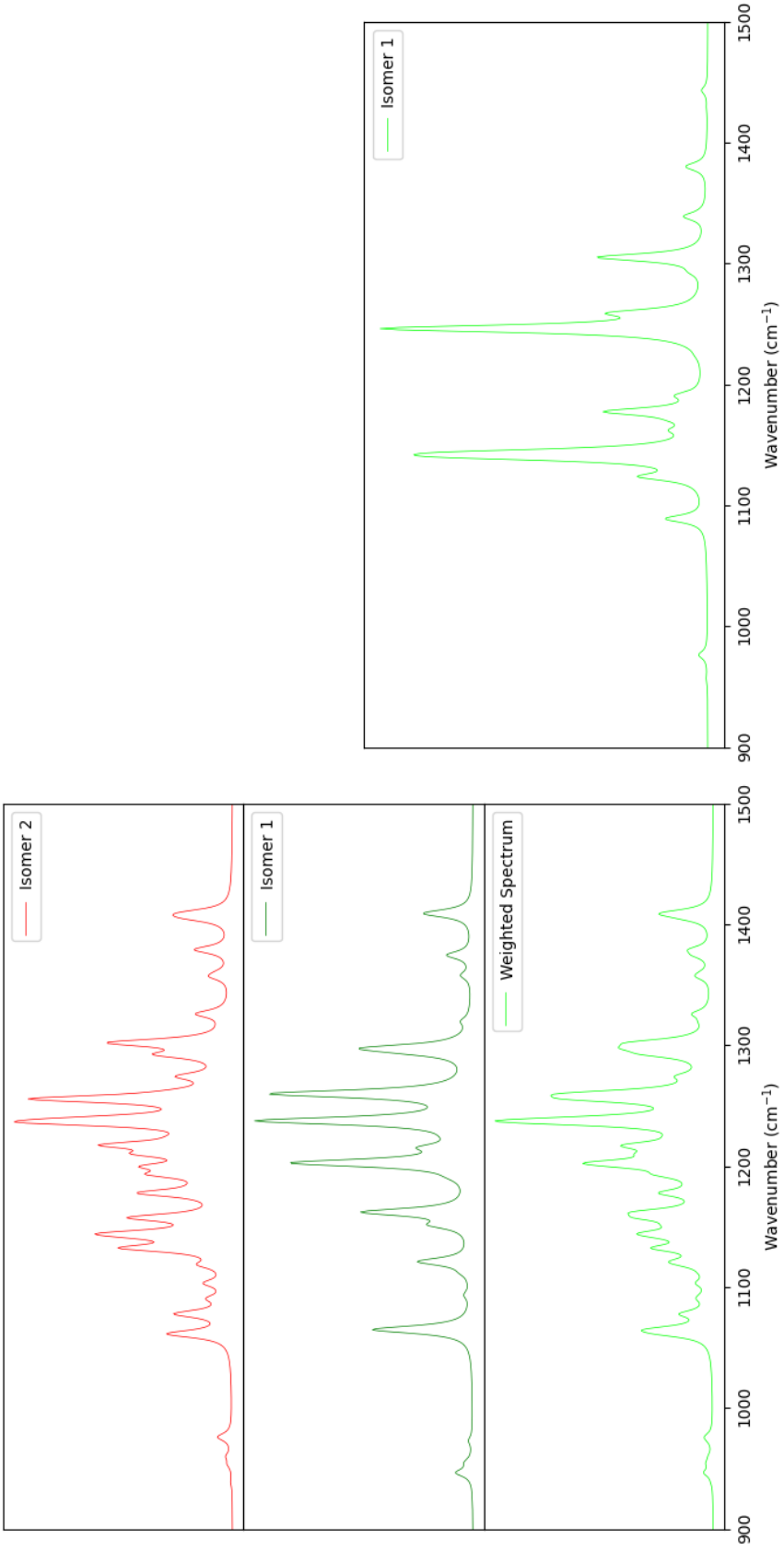

Figure 6.12: A comparison of the weighted computational vibrational spectra obtained for sodium (left) and chloride (right) monomer complexes of HTFMCH.

6.6 Conclusion

In summary, these HFCH derivatives showed a number of interesting binding motifs and binding affinities. HTFMCH readily interacts with cationic species, significantly more favourably than the other molecules, but pales in comparison for anionic interactions. PFCHOL introduces the ability to interact with hydrogen bonded species potentially introducing applications in biological systems, while maintaining a strong affinity for ionic species. These derivative species show the potential for applications of substituted cyclohexane species in terms of how they may further the understanding of cyclic binding motifs in the gas phase.

Chapter 7

Inverse Sandwich Cyclopentadienyl Complexes of Sodium in the Gas Phase

7.1 Introduction

The synthesis of ferrocene in the early 1950's and the subsequent elucidation of its structure as that of a "sandwich" compound rapidly led to the development of the new area of organometallic chemistry.[178,179] Similarly, the subsequent demonstration that the cyclopentadienyl (Cp) anion could form complexes with main group elements gave rise to a wide structural diversity depending upon the nature of the main group cation involved.[180] In addition however, it also led to the realization that a new type of chemical bond had been demonstrated, that of π complexes, which has since been extremely valuable for the understanding of subtle influences on the structures of many polyfunctional molecules and complexes. The quantitative study of gas phase ion-molecule π complexes was initiated by Kebarle and coworkers who, in 1981, demonstrated that the potassium cation was bound to benzene by ~80 kJ mol^{-1}, which was, in fact, greater than the magnitude of the binding of K^+ to H_2O of ~75 $kJmol^{-1}$.[181] Subsequent studies of the series of alkali cation binding enthalpies to benzene revealed the expected trend of decreasing bond strength with increasing cation size, ranging from 161 $kJmol^{-1}$ for Li^+ down to 64 $kJmol^{-1}$ for Cs^+.[182] Kebarle had also pointed out the importance of ion-quadrupole and ion-induced dipole interactions for the determination of the geometry of these π complexes as well as the understanding of the magnitude of the interaction energies. Many subsequent studies have shown the ubiquitous importance of cation-π interactions in a wide variety of chemical bonding environments involving π systems, with an especially rich amount of data now available for aromatic amino acids.[152,183–186]

X-ray crystallographic methods have also been shown to be very valuable in elucidating the nature of the interactions occurring in π complexes, particularly those involving alkali cations.

For example, for the simplest metallocene sandwich complex, the lithocene anion ($LiCp_2^-$), the structure has been determined for the salt formed with the tetraphenylphosphonium cation (Ph_4P^+), to reveal that the Cp-rings are near co-planar with a Li distance to the ring centroids of 2.008 Å, Li-C distances of 2.32 ±0.05Å and an angle of 87° between the ring planes and the line of centres between the ring centroids.[187] While the crystal structure shows the rings to be nearly parallel, they are rotated in the plane by 180° with respect to each other. An analogous study by the same authors of the sodocene species with Ph_4P^+ determined the Na^+ to ring centroid distance to be 2.366 Å.[188]

The term "inverse sandwich compounds" was first proposed by Streitwieser and Smith who had defined them as having a "central dianion and two cationic π-rings as ligands".[189] They then computationally explored the potential existence of a number of neutral compounds consisting of two substituted cyclopropenyl cations coordinated with various dianions.[189] The first experimental demonstration of an inverse sandwich compound was by Wessel et al. who carried out a reaction of the lithocene anion with the tris(dimethylamino)sulfonium (TAS) cation, resulting in a cationic "inverse" sandwich species,$[(TAS)Cp(TAS)]^+$, which crystallized as a salt with a so-called "naked" Cp^- a the counter ion.[190] Subsequent reaction of this salt with CpM species (M = Li, Na, K) resulted in formation of salts containing $CpMCp^-$ units which could be characterized cyrstallographically. The resulting lithocene species exhibited a structure nearly identical to that formed with Ph_4P^+ as the counterion. The corresponding sodocene anion, $[CpNaCp]^-$, has nearly perfect D_{5d} symmetry with rings tilted out of co-planarity by only ∼1° and with Na-C bond distances of 2.618 ± 0.02 Å corresponding to a distance from Na to the ring centroid of 2.322 Å.

While there have been several studies of gas phase π complexes of metal ions with benzene, analogous studies of the gas phase ion chemistry of metallocene complexes, other than those of ferrocene, are relatively limited.[33–39] Protonation of ferrocene at the metal center is apparently the most energetically favorable site, however there are suggestions, based on gas phase H/D exchange measurements, that either ring protonation, or an agostically bonded structure, may also be energetically accessible.[33,39] Foster and Beauchamp have examined ion-molecule reactions of ions derived from ferrocene with neutral ferrocene and one such reaction led to the formation of a $Fe_2Cp_3^+$ species which the authors had suggested might have a "triple-

decker sandwich" structure.[33] In the present work, the characterization of several complexes of sodium cations with cyclopentadienyl anions has been carried out via infrared multiple photon dissociation (IRMPD) spectroscopy and electronic structure calculations.

7.2 Methods

In the present study, computational investigation of structure and energetics of the complexes involving Na^+ and Cp^- units observed via electrospray ionisation (ESI) was carried out using the Gaussian 09 program with geometry optimizations and frequencies determined using the B3LYP functional and 6-311++G(d,p) basis set on carbon and hydrogen atoms and the aug-cc-pCVDZ basis set for sodium.[164,191] Subsequently, single point energies were determined at the MP2 level of theory using the same basis sets.

Experimentally, vibrational characterization of complexes of the general form $[Na_{n+1}Cp_n]^+$ was carried out at the FELIX free electron laser (FEL) laboratory.[82] Aliquots of 5M NaCp in THF were dissolved in a 50:50 methanol water mixture at $\sim$50 μM concentration and the desired ions resulting from ESI were mass selected and trapped in a modified quadrupole ion trap mass spectrometer (Bruker Amazon) interfaced with the output of the FELIX infrared (IR) beam.[82] After irradiation of the trapped ions, mass spectra were recorded as a function of the wavelength-tunable output of the FEL. The resulting data were reduced to obtain the fractional dissociation of mass-selected parent ions into fragment ions to yield a consequence spectrum serving as a proxy for the IR absorption spectrum that can be compared to the computed linear absorption IR spectra.

7.3 Results and Discussion

The structures of the three species experimentally observed, Na_2Cp^+, $Na_3Cp_2{}^+$ and $Na_4Cp_3{}^+$, are shown in **Figure 7.1** with the corresponding Na^+ to ring centroid distances. For each of the three structures shown in **Figure 7.1** the computed geometries of the cyclopentadienyl rings remain essentially unchanged to within 0.001 Å with C-C bond distances of 1.423 Å and C-H bond distances of 1.082 Å as well as C-C-C bond angles of 108° and H-C-C bond angles of 126°. In the case of $Na_4Cp_3{}^+$ there are two different Cpenvironments and the C-C bond

distances in the outer rings are computed to be 1.423 Å while those in the central Cp-ring are 1.421 Å. These Cp-ring geometries are only slightly different from those computed for the isolated cyclopentadienyl anion, where each of the bond angles are essentially identical to those in the sodium complexes, while the C-C bond distances are somewhat shorter at 1.415 Å and the C-H bond distances very slightly longer at 1.086 Å. Thus it is clear that the interactions of the cyclopentadienyl moieties with the sodium cations perturb the geometries of the cyclopentadienyl moieties to a very minor extent, leading to a suggestion that the binding forces in these complexes may be predominantly electrostatic.

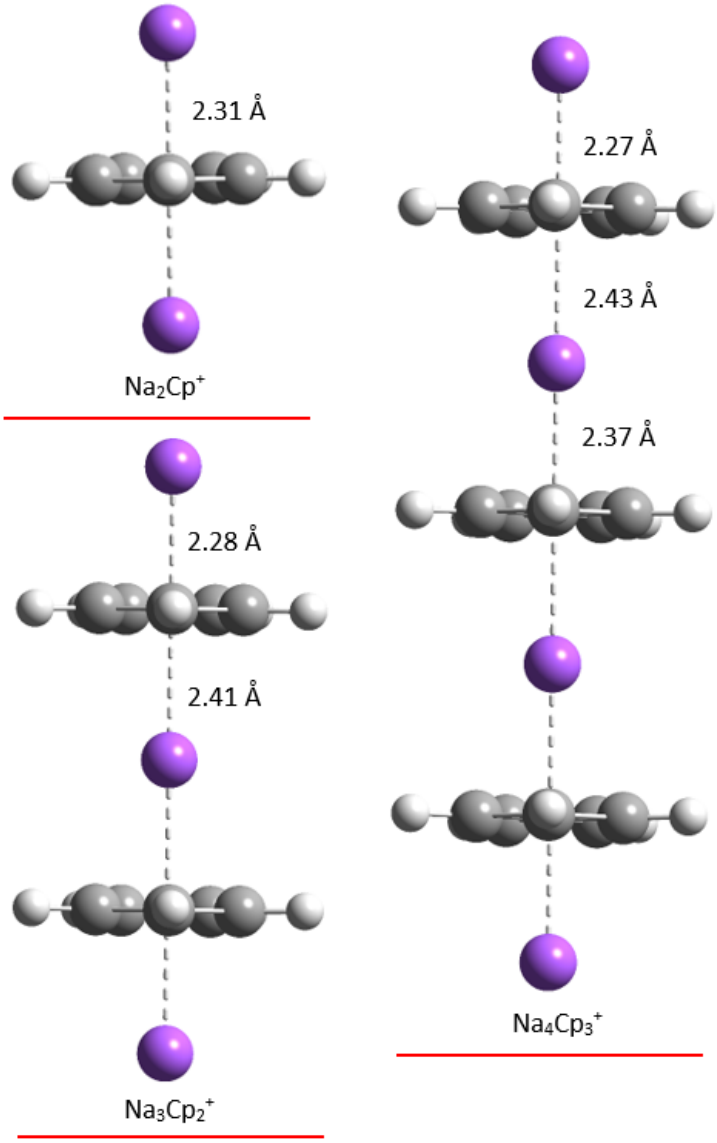

Figure 7.1: Structures of the complexes observed with the corresponding Na^+ to ring centroid distance.

In the case of Na_2Cp^+, where Na^+ was the only dissociation fragment, the lower mass range of the mass spectrometer did not permit observation of the fragment and the consequence spectrum was obtained from the net depletion of the parent ion intensity. The relevant computed mode frequencies with their associated intensities for the three cationic NaCp adducts experimentally observed are summarized in **Table 7.1** and the corresponding spectra, computed and experimentally observed, are shown in **Figure 7.2**. The computational data reveal a number of vibrational modes which are predicted to have considerable absorption intensities but which lie at lower wavenumbers which were not interrogated in the current experiments. Nevertheless, as discussed below, these modes can prove to be of considerable importance in the interpretation of the IRMPD spectra observed. These modes are included in **Table 7.1**.

Table 7.1: Computed Mode Vibrations (cm^{-1}) *and Corresponding IR Linear Absorption Intensities* ($kmmol^{-1}$)

Mode	Na-Cp-Na bend	Na-Cp-Na asym stretch	C-H oop bending	C-H ip bending
Cp^-			621 (267)	982 (41)
Na_2Cp^+	109 (25)	272 (86)	780 (250)	985 (34)
$Na_3Cp_2^+$	119 (25)	281 (166)	760 (552) 769 (1)	986 (54)
$Na_4Cp_3^+$	123 (27)	283 (53)	762 (692) 747 (191)	987 (66)
$NaCp_2^-$	59 (5)	268 (71)	682 (574)	985 (57)
$Na_2Cp_3^-$	86 (6)	278 (152)	725 (182) 690 (714)	987 (55) 984 (21)

The modes in the vicinity of 110 - 125 cm^{-1} for the three species can be described as symmetric bending modes in which the Na^+ atoms move laterally, in a concerted fashion, relative to the ring planes while the rings move in the opposite direction. This effectively gives a change in the Na^+-ring centroid-Na^+ bond angles which can be both positive and negative. In the cases of the two larger species the amplitude of motion of the Na^+ between two rings is larger than the amplitude of motion of the "outside" Na^+ entities. The modes from 272 - 283 cm^{-1} each involve simultaneous motion of each of the Na^+ in the same direction relative to the adjacent ring centroids thus giving rise to what is effectively an asymmetric stretch of each pair of Na^+ atoms relative to the adjacent ring centroids. The strongest absorption modes in each case are those from 747 - 780 cm^{-1} and these involve simultaneous motion of all of the C-H bonds above and below the ring planes. For $Na_3Cp_2^+$ the modes at 760 cm^{-1} involve out of plane motion of the C-H bonds of both rings in the same direction while the weaker mode at 768 cm^{-1} has out of plane motions of the C-H bonds of the two rings in opposite directions. In the case of the two

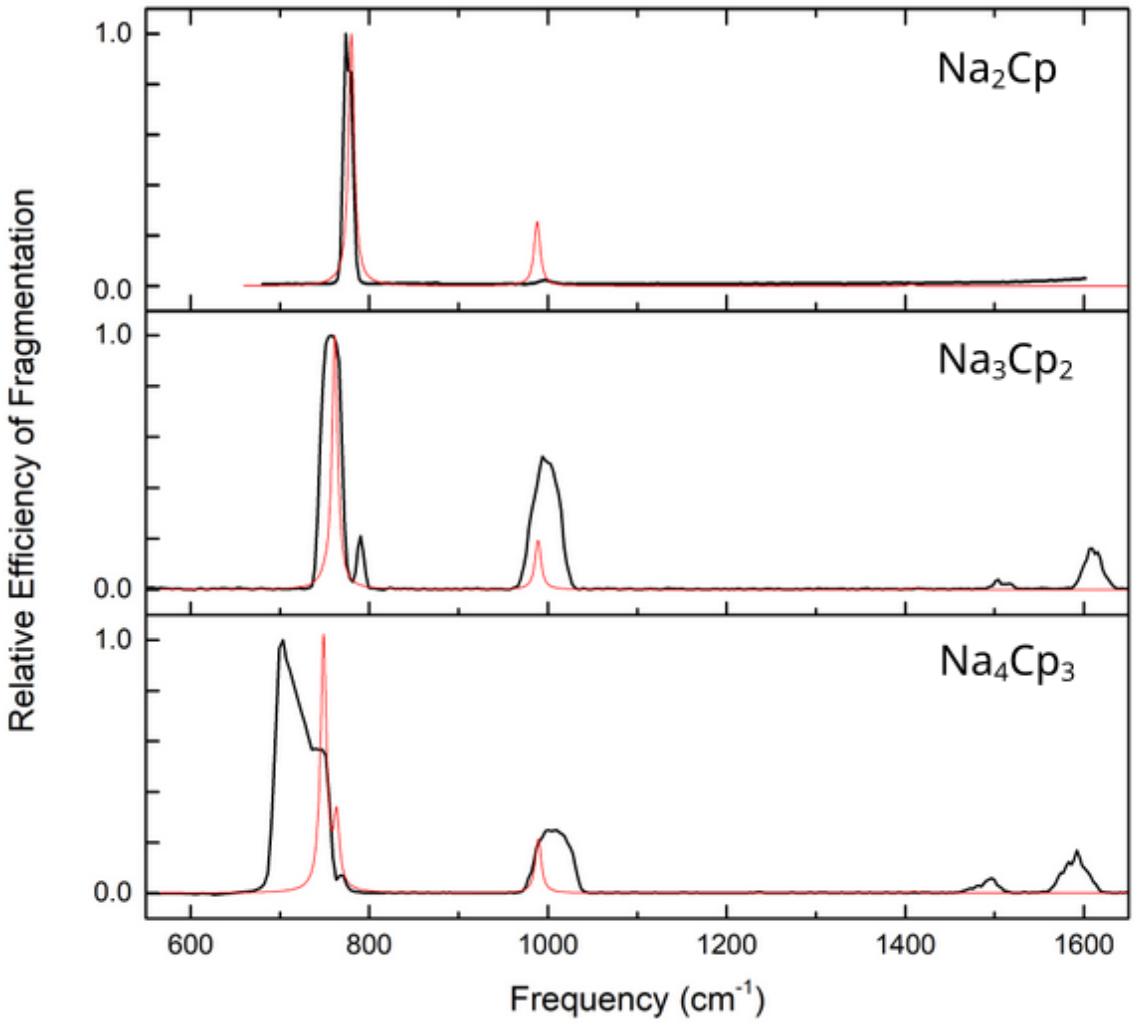

Figure 7.2: Experimental IRMPD spectra of the three sodium cyclopentadienide complexes (black) together with the corresponding computed vibrational absorption spectra (red). In each case, relative experimental intensities represent fractional extents of fragmentation relative to the most intense feature in the individual spectra.

C-H bending modes observed for $Na_4Cp_3^+$, the mode at 747 cm^{-1} has motion of all C-H bonds above and below all three ring planes in unison, with the amplitude of out-of-plane motion for the central ring being somewhat larger than those of the exterior rings. The less intense mode at 762 cm^{-1} involves the C-H out-of-plane bending of the central ring in the opposite sense to those of the exterior rings, now with the out of plane motions of the exterior rings being somewhat larger in amplitude. The modes near 985cm^{-1} in each case are C-H in-plane bending modes in which the ring centroid-C-H bond angles deviate above and below 180° while remaining in the ring plane. The similarity of the frequencies of all of these in plane bending modes and their intensities, as well as those for the isolated cyclopentadienide anion is quite striking.

Modes other than those summarized here are predicted to have absorption intensities at least one to two orders of magnitude lower than those summarized in **Table 7.1**. Also shown in **Table 7.1** are the corresponding values for the bare cyclopentadienide anion as well as those computed for the two analogous anionic species. It is immediately apparent that the agreement between the experimental frequencies of the two major peaks observed in the 760 and 985 cm^{-1} regions for the cationic species and those obtained computationally is excellent. As noted above, in each case, these modes represent the concerted out-of-plane and in-plane bending motions respectively of the C-H moieties of the Cp-rings. The experimental features which do not match well any of the computed mode frequencies are those observed at ∼1500 and ∼1600 cm^{-1} in the experimental spectra of both the $Na_3Cp_2^+$ and $Na_4Cp_3^+$ whereas no modes are found computationally between 1420 and 3000cm^{-1} for either of these species. This thus suggests that the peaks experimentally observed in these regions may be due either to overtones or combination bands, or some combination of the two. As shown in **Table 7.1**, the modes observed in the 740 - 780 cm^{-1} range are the most intense in each of the three cases which would suggest that these would be the most likely to contribute to overtone and combination bands. As a result, it seems highly likely that the features observed near 1500 cm^{-1} for $Na_3Cp_2^+$ and $Na_4Cp_3^+$ correspond to the first overtones of the C-H out of plane bending modes at 760 and 747 cm^{-1} respectively. Similarly, the features near 1600cm^{-1} may then be associated to the first overtones of the out-of-plane bending modes coupled with the corresponding Na-Cp-Na bending modes near 120 cm^{-1} in each case. Finally, the rather unusual shape of the broad feature observed in the 670 - 780 cm^{-1} region for $Na_4Cp_3^+$ might then also be rationalized as the result of the second overtone of the Na-Cp-Na asymmetric stretching mode overlaid on the out-of-plane C-H bending mode. The absence of an analogous feature in the spectrum of $Na_3Cp_2^+$ might then also be explained as result of the lower energy requirement to effect dissociation in the $Na_4Cp_3^+$ species. In this respect it is of interest to note that in the solution phase IR spectrum of sodium cyclopentadienide in THF the authors conclude that "weak and medium bands in the range of 1500 - 2000 cm^{-1} are likely due to second-order transitions (overtones and combination tones)".[192,193]

The evolution of the experimental relative intensities of the modes at ∼760 cm^{-1} and ∼985 cm^{-1} for the three species observed can be largely attributed to the decrease in dissociation energy for loss of NaCp in proceeding from Na_2Cp^+ to $Na_4Cp_3^+$. For Na_2Cp^+ very little

fragmentation is observed near 982 cm^{-1} and the spectrum is dominated by dissociation at ~780 cm^{-1}. For $Na_3Cp_2^+$ the dissociation energy for NaCp loss has decreased by ~55 $kJmol^{-1}$ giving rise to enhanced dissociation at the weaker 986 cm^{-1} mode. Following this argument, for $Na_4Cp_3^+$, an even larger ratio of intensities of the 987 to 747 cm^{-1} modes might have been anticipated. However, any such enhancement is likely now obscured by the participation of the overtone/combination band in this vicinity, described above.

It is also of interest to note that, for the cyclopentadienide anion and the two anionic complexes computed, the C-H in plane bending modes are effectively exactly the same as those found for the cationic species. Similarly, the stretching modes near 270 cm^{-1} are also nearly the same for both cationic and anionic complexes regardless of size. Those modes where there are substantial differences between anionic and cationic species are those for the cationic Na-Cp-Na bending and anionic Cp-Na-Cp bending motions. Finally, it is very noteworthy that in all cases the stretching modes all occur near the same frequency of 278 ± 6 cm^{-1}. These vibrational results thus also point very strongly toward the predominance of an electrostatic bonding for these complexes.

In order to fully understand and interpret the IRMPD data it is of interest also to examine the relative energetics of the dissociation processes associated with each IRMPD spectrum. In each case, the lowest energy dissociation process involves loss of a single NaCp unit which, in the case of the two larger species, may be followed by loss of a subsequent NaCp unit. The data for the relevant processes, 1-3, summarized in **Table 7.2** show that each successive loss of a NaCp unit becomes less endothermic, a phenomenon which is usually observed for dissociation of multimeric species of increasing size. However, in the case of the two larger species it is also of interest to examine the energetics of a possible alternative dissociation pathway, that of loss of Na^+ to yield a neutral Na_nCp_n species as shown in reactions 4 and 5. In contrast to the decreasing progression for loss of NaCp units in reactions 1-3, the enthalpy changes for loss of Na^+ in reactions 4,5 and 6 show a considerable increase as the size of the parent complex increases. Although somewhat counterintuitive from a cluster complex point of view, this progression of enthalpy changes for loss of Na^+ can be understood from an examination of the dipole moments of the neutral Na_nCp_n units involved, which are found to increase from 6.67 D in the case of NaCp, to 16.4 D for Na_2Cp_2 and 27.0 D for Na_3Cp_3. Thus, if as is suspected, the binding in these gas phase inverse sandwich

complexes is primarily electrostatic, the significant increase in enthalpy of binding to a single Na^+ with increasing number of NaCp units, is a result of the greater magnitude of the ion-dipole interactions as the number of NaCp units grows. The decrease in the difference between reactions 5 and 6 relative to the difference for reactions 4 and 5 might then be understood as a result of the greater distance between the departing sodium ion and the origin of the dipole moment of the Na_nCp_n residue or the smaller ratio of dipole moments for the pair of the two larger species.

Table 7.2: Dissociation Energetics for Selected Sodium Cyclopentadienide Complexes at 298 K

Reaction	$\Delta\mathbf{H}^\circ$(kJmol^{-1})	$\Delta\mathbf{S}^\circ$(JK^{-1}mol^{-1})	$\Delta\mathbf{G}^\circ$(kJmol^{-1})
1. $Na_2Cp^+ \rightarrow Na^+ + NaCp$	219.6	103.8	188.6
2. $Na_3Cp_2{}^+ \rightarrow Na_2Cp^+ + NaCp$	165.8	111.1	132.7
3. $Na_4Cp_3{}^+ \rightarrow Na_3Cp_2{}^+ + NaCp$	151.4	123.6	114.5
4. $Na_2Cp^+ \rightarrow Na^+ + NaCp$	219.6	103.8	188.6
5. $Na_3Cp_2{}^+ \rightarrow Na^+ + Na_2Cp_2$	284.7	110.1	251.9
6. $Na_4Cp_3{}^+ \rightarrow Na^+ + Na_3Cp_3$	313.8	105.5	283.3
7. $NaCp_2{}^- \rightarrow Cp^- + NaCp$	217.0	123.4	180.2
8. $Na_2Cp_3{}^- \rightarrow Cp^- + Na_2Cp_2$	280.7	126.2	243.1
9. $Na_2Cp_3{}^- \rightarrow NaCp_2{}^- + NaCp$	164.4	107.7	132.3

In this context, it is also of interest to examine the distances from the sodium cations to the adjacent cyclopentadienide ring centroids. For the three complexes examined here, the distance from an "outside" Na^+ to the adjacent ring centroid decreases from 2.31 Å in Na_2Cp^+ to 2.28 Å in $Na_3Cp_2{}^+$ and further to 2.27 Å in $Na_4Cp_3{}^+$, consistent with the corresponding computed enthalpy changes for loss of Na^+ from each of these species. In addition, it is significant to note that for the "interior" Na+ to ring centroid distances of 2.41 Å in $Na_3Cp_2{}^+$ and 2.37 Å $Na_4Cp_3{}^+$ there is a slight decrease going from the smaller to the larger complex and that the larger complex begins to very closely approach the crystallographic result of 2.357 Å for solid NaCp.[194] Thus, these complexes represent a very good gas phase proxy for the solid state species.

Due to the fact that the solution phase acidity of cyclopentadiene is less than that of the ESI solvent species used, negative ion sodium cyclopentadienide complexes were not observed. Nevertheless, it is revealing to examine the computational results for dissociations reactions of anionic complexes analogous to the positive ion complexes experimentally examined. Thus, a comparison of reactions 1 and 7 and reactions 2 and 9, which all involve a loss of a NaCp unit, shows that the enthalpy changes for each of these pairs of dissociations are essentially the

same. Similarly, the dissociation enthalpies for reactions 5 and 8, which each involve loss of a Na_2Cp_2 moiety, are also very close in magnitude. The fact that that the dissociation reactions involving loss of Na_2Cp_2 are substantially greater than those involving the loss of NaCp is again consistent with the fact that the dipole moment of Na_2Cp_2 is greater than that of NaCp giving rise to the greater magnitude of the ion-dipole interaction, which is likely the dominant factor in the bonding of the ionic aggregates.

The similarity in binding energetics for loss of NaCp or Na_nCp_n units from either Na^+ or Cp^- ions leads to the implication that such complexes are very largely electrostatically bound by a combination of ion-ion and/or ion-dipole interactions. For example, the dissociation of NaCp to yield Na^+ and Cp^- is computed to involve a change in enthalpy of $\sim$600 kJmol^{-1} whereas a point charge model, using a separation equal to the computed distance for the Na^+ to ring centroid of 2.21 Å gives a value of 628 kJmol^{-1}. An examination of the molecular orbitals computed for each of the cationic species investigated here also shows that, in no case, is there any "orbital overlap" between the sodium and cyclopentadienide moieties as exemplified by the HOMO for $Na_4Cp_3{}^+$ shown in **Figure 7.3**. Consistent with this, is the finding that, computationally, effectively zero barrier is observed for rotation of the Cp rings about the axis formed by the line of centres of the Na^+ atoms and the ring centroids.

Interestingly, a somewhat analogous cluster structural motif had been proposed by Masubuchi et al. for anionic complexes of vanadium with benzene.[195] In that work, laser ablation of vanadium in a supersonic expansion generated anions which, in reaction with benzene (Bz) gas diluted in helium, gave rise to $(V_nBz_{n+1})^-$ and $(V_nBz_n)^-$ species for n = 1 - 5 which were interrogated by negative ion photoelectron spectroscopy. Accompanying computational work proposed that the lowest energy structures were sandwich species with vanadium to ring centroid distances ranging from 1.63 to 1.75 Å. However, subsequent work revealed that, although these sandwich species were indeed energy minima, the global minima for the V2 species were based on a vanadium dimer core.[196] V3 species possibly had a mixture of structure types while V4 and V5 species were concluded to have the originally proposed sandwich structures. The much smaller vanadium to ring centroid distances relative to those in the present work, and the molecular orbital calculations suggest covalent bonding in the sandwich structures.

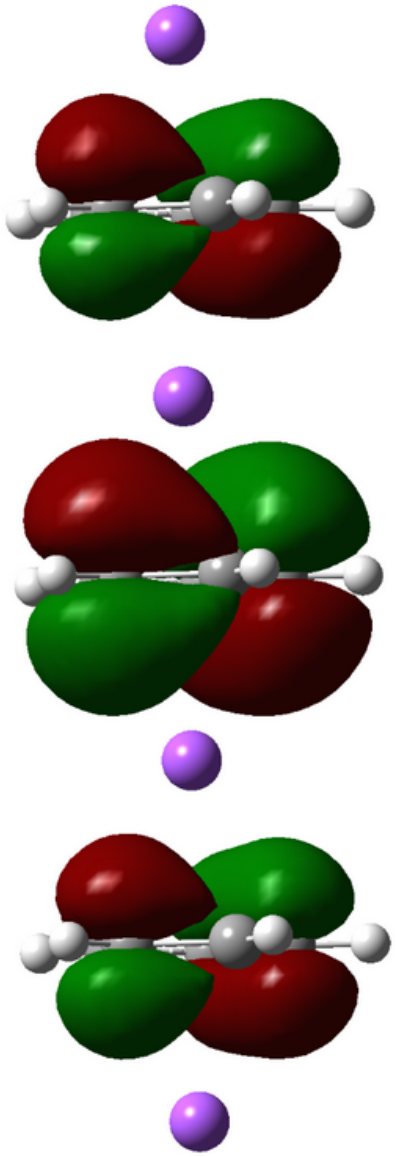

Figure 7.3: HOMO for $Na_4Cp_3^+$.

7.4 Conclusion

The "interior" and "exterior" distances, expanding and contracting respectively, in increasing ionic complex size serves as an understanding to the limitation of the dipole moment or electrostatic ability to form "sandwich" compounds as distances become too dramatic for these interactions to occur. Together with the experimental IRMPD data presented here in conjunction with the associated computational geometries and vibrational frequencies thus provide valuable insight into the nature of the bonding in these gas phase sodium cyclopentadienyl complexes, which also serve to understand the nature of the analogous solid state species.

Chapter 8

Conclusion

In summary, the cyclic species studied herein have shown a number of promising intermolecular interactions, illustrating the need to further study these species in gas phase ion chemistry. They introduce a number of binding motifs that are inadequately studied or misunderstood in the literature and show a significant propensity for binding ionic species in both ion-dipole and ion-π environments.

In Chapter 3, the efficacy of the systematic sampling of cluster surfaces (SSCS) technique was examined through the study of a number of model clusters, such as clusters of neutral and protonated solvents, and showed results that were topologically identical to those produced using the classical discovery methods. Additionally, in heterogeneous clusters it demonstrated the ability to discover new low lying experimental minima, while still producing topologically identical global minimum geometries as those found using the Basin Hopping (BH) method. Though the SSCS technique is flawed for systems with significant degrees of freedom, incorporation of this new method in conjunction with other classical techniques, such as the BH algorithm, could prove invaluable, thus reducing the flaws of both techniques if used in tandem.

In Chapter 4, a study on deprotonated para-hydroxybenzoic acid (PHBA) found significant evidence that debate for gas phase tautomer preference in the literature is likely a result of electrospray ionisation (ESI) spray conditions. Investigation of 'solution phase' conditions found that regardless of the type of solvent selected, be it protic or aprotic, all solvents show a shift towards 'gas phase' tautomer preference with an increase in temperature to some extent. Examining 'gas phase' conditions by modeling solvent clusters of size n = 1 - 5 for common ESI solvents found identical behaviour, showing again that all solvents show a shift towards 'gas phase' tautomer preference with an increase in temperature. Examining the relative populations of 'gas phase' clusters, dependent upon temperature, allowed for an approximation of tautomer preference by matching the cluster size to the relative energy of the two tautomers.

Therefore, the tautomer preference shown in the literature for this system is a result of the effective cluster temperature and not solvent selection.

In Chapters 5 and 6, a study of substituted cyclohexanes found a number of promising results for applications in a number of areas for chemistry and biology. The first compound investigated, all-cis 1,2,3,4,5,6-hexafluorocyclohexane (HFCH), was shown to have a significant propensity for both cationic and anionic species in both monomeric and dimeric systems. The alcohol derivative of this compound, all-cis 1,2,3,4,5,6-pentafluorocyclohexanol (PFCHOL), had a binding propensity weaker than that of HFCH for ionic systems, however it introduced an anchor for hydrogen bonding networks, showing potential applications in biological systems. Finally, all-cis 1,2,3,4,5,6-hexa-trifluoromethyl-cyclohexane (HTFMCH) was found to have the weakest binding propensity for cationic species, but the strongest for anionic species. This illustrates the various use cases for these substituted cyclohexanes, introducing a number of novel binding modes for cyclic species in the gas phase.

In Chapter 7, a study on the cation-π interactions in sodium cyclopentadienyl complexes displayed a significant binding enthalpy, with the addition of each subunit becoming more favourable. This feature explains the ability of this species to readily form solid state species experimentally. It was found that vibrational infrared multiple photon dissociation (IRMPD) spectra did not show good agreement with conventional computational spectra, requiring the analysis of anharmonic vibrational modes in these systems. This brings to light the need to expand the study of such species to further the applicability of conventional vibrational mode analysis of gas phase ions.

Thus, this thesis presents the many novel properties of cyclic species in the gas phase. These species demonstrate the ability to bind with a number of molecules and ionic species through a number of binding motifs. With the work presented in this thesis, we hope to enable a more efficient study of these cyclic species while providing insight into how valuable these species could be in a number of areas of scientific research.

References

1. WATSON, J. D.; CRICK, F. H. C. Molecular Structure of Nucleic Acids: A Structure for Deoxyribose Nucleic Acid. *Nature* **1953**, *171*, 737–738.
2. Singleton, M. R.; Dillingham, M. S.; Wigley, D. B. Structure and Mechanism of Helicases and Nucleic Acid Translocases. *Annual Review of Biochemistry* **2007**, *76*, 23–50.
3. Wu, G. Amino acids: metabolism, functions, and nutrition. *Amino Acids* **2009**, *37*, 1–17.
4. Maloy, S. *Brenner's Encyclopedia of Genetics*; Elsevier, 2013; pp 108–110.
5. Dietzen, D. J. *Principles and Applications of Molecular Diagnostics*; Elsevier, 2018; pp 345–380.
6. McGaughey, G. B.; Gagné, M.; Rappé, A. K. π-Stacking Interactions. *Journal of Biological Chemistry* **1998**, *273*, 15458–15463.
7. Gazit, E. A possible role for π-stacking in the self-assembly of amyloid fibrils. *The FASEB Journal* **2002**,
8. McRae, E. K.; Booy, E. P.; Padilla-Meier, G. P.; McKenna, S. A. On characterizing the interactions between proteins and guanine quadruplex structures of nucleic acids. 2017.
9. Thiele, J. Zur Kenntniss der ungesättigten Verbindungen. Theorie der ungesättigten und aromatischen Verbindungen. *Justus Liebig's Annalen der Chemie* **1899**, *306*, 87–142.
10. Muller, P. Glossary of terms used in physical organic chemistry (IUPAC Recommendations 1994). *Pure and Applied Chemistry* **1994**, *66*, 1099.
11. Wu, C.; Siems, W. F.; Klasmeier, J.; Hill, H. H. Separation of isomeric peptides using electrospray ionization/high- resolution ion mobility spectrometry. *Analytical Chemistry* **2000**,
12. Lintonen, T. P.; Baker, P. R.; Suoniemi, M.; Ubhi, B. K.; Koistinen, K. M.; Duchoslav, E.; Campbell, J. L.; Ekroos, K. Differential mobility spectrometry-driven shotgun lipidomics. *Analytical Chemistry* **2014**,
13. Lanucara, F.; Holman, S. W.; Gray, C. J.; Eyers, C. E. The power of ion mobility-mass spectrometry for structural characterization and the study of conformational dynamics. 2014.
14. Hinz, C.; Liggi, S.; Griffin, J. L. The potential of Ion Mobility Mass Spectrometry for high-throughput and high-resolution lipidomics. 2018.
15. Zhou, C.; Ieritano, C.; Hopkins, W. S. Augmenting Basin-Hopping With Techniques From Unsupervised Machine Learning: Applications in Spectroscopy and Ion Mobility. *Frontiers in Chemistry* **2019**, *7*, 519.
16. Bakó, I.; Jedlovszky, P.; Pálinkás, G. Molecular clusters in liquid methanol: a Reverse Monte Carlo study. *Journal of Molecular Liquids* **2000**, *87*, 243–254.
17. Wright, D.; El-Shall, M. S. A Monte Carlo study of methanol clusters (CH 3 OH) N , N =5–256. *The Journal of Chemical Physics* **1996**, *105*, 11199–11208.

18. Estrogenic Effects ofp-Hydroxybenzoic Acid in CD1 Mice. *Environmental Research* **1997**, *75*, 130–134.

19. Hoberg, E.; Meier, B.; Sticher, O. An analytical high performance liquid chromatographic method for the determination of agnuside andp-hydroxybenzoic acid contents in Agni-casti fructus. *Phytochemical Analysis* **2000**, *11*, 327–329.

20. Barkosky, R. R.; Einhellig, F. A. Allelopathic interference of plant-water relationships by parahydroxybenzoic acid. *Botanical Bulletin of Academia Sinica* **2003**,

21. Barr, L.; Metaxas, G.; Harbach, C. A. J.; Savoy, L. A.; Darbre, P. D. Measurement of paraben concentrations in human breast tissue at serial locations across the breast from axilla to sternum. *Journal of Applied Toxicology* **2012**, *32*, 219–232.

22. K. Khetan, S. *Endocrine Disruptors in the Environment*; John Wiley & Sons, Inc.: Hoboken, NJ, USA, 2014; p 109.

23. Tian, Z.; Kass, S. R. Does electrospray ionization produce gas-phase or liquid-phase structures? *Journal of the American Chemical Society* **2008**, *130*, 10842–10843.

24. Tian, Z.; Wang, X. B.; Wang, L. S.; Kass, S. R. Are carboxyl groups the most acidic sites in amino acids? Gas-phase acidities, photoelectron spectra, and computations on tyrosine, p-hydroxybenzoic acid, and their conjugate bases. *Journal of the American Chemical Society* **2009**, *131*, 1174–1181.

25. Steill, J. D.; Oomens, J. Gas-phase deprotonation of p-hydroxybenzoic acid investigated by IR spectroscopy: Solution-phase structure is retained upon ESI. *Journal of the American Chemical Society* **2009**, *131*, 13570–13571.

26. Schröder, D.; Buděšínský, M.; Roithová, J. Deprotonation of p-hydroxybenzoic acid: Does electrospray ionization sample solution or gas-phase structures? *Journal of the American Chemical Society* **2012**, *134*, 15897–15905.

27. More, M. B.; Ray, D.; Armentrout, P. B. Intrinsic Affinities of Alkali Cations for 15-Crown-5 and 18-Crown-6: Bond Dissociation Energies of Gas-Phase M + +Crown Ether Complexes. *Journal of the American Chemical Society* **1999**, *121*, 417–423.

28. Linstrom, P. J., Mallard, W. G., E. NIST Chemistry WebBook, NIST Standard Reference Database Number 69. 2015.

29. Ziegler, B. E.; Lecours, M.; Marta, R. A.; Featherstone, J.; Fillion, E.; Hopkins, W. S.; Steinmetz, V.; Keddie, N. S.; O'Hagan, D.; McMahon, T. B. Janus Face Aspect of All-cis 1,2,3,4,5,6-Hexafluorocyclohexane Dictates Remarkable Anion and Cation Interactions In the Gas Phase. *Journal of the American Chemical Society* **2016**, *138*, 7460–7463.

30. Dougherty, D. A. Cation-π interactions in chemistry and biology: A new view of benzene, Phe, Tyr, and Trp. *Science* **1996**,

31. Wouters, J. Cation-π- (Na+-Trp) interactions in the crystal structure of tetragonal lysozyme. *Protein Science* **1998**,

32. Gallivan, J. P.; Dougherty, D. A. Cation-π interactions in structural biology. *Proceedings of the National Academy of Sciences of the United States of America* **1999**,

33. Foster, M. S.; Beauchamp, J. L. Ion-molecule reactions and gas-phase basicity of ferrocene. *Journal of the American Chemical Society* **1975**, *97*, 4814–4817.

34. Corderman, R. R.; Beauchamp, J. L. Ion chemistry and gas-phase basicity of nickelocene by ion cyclotron resonance spectroscopy. *Inorganic Chemistry* **1976**, *15*, 665–668.

35. Hunt, D. F.; Sethi, S. K. Gas-phase ion/molecule isotope-exchange reactions: methodology for counting hydrogen atoms in specific organic structural environments by chemical ionization mass spectrometry. *Journal of the American Chemical Society* **1980**, *102*, 6953–6963.

36. Ikonomou, M. G.; Sunner, J.; Kebarle, P. Kinetics and thermodynamics of protonation of ferrocene in the gas phase. *The Journal of Physical Chemistry* **1988**, *92*, 6308–6312.

37. Meot-Ner, M. Ion chemistry of ferrocene. Thermochemistry of ionization and protonation and solvent clustering. Slow and entropy-driven proton-transfer kinetics. *Journal of the American Chemical Society* **1989**, *111*, 2830–2834.

38. Allison, C. E.; Cramer, J. A.; Hop, C. E. C. A.; Szulejko, J. E.; McMahon, T. B. Strong hydrogen bonding in gas-phase ions. A high-pressure mass spectrometric study of the proton affinity, proton transfer kinetics, and hydrogen-bonding capability of iron pentacarbonyl. *Journal of the American Chemical Society* **1991**, *113*, 4469–4473.

39. Hop, C. E. C. A.; McMahon, T. B. Protonation of Ferrocene in the Gas Phase. *Journal of the American Society for Mass Spectrometry* **1994**, *5*, 274–281.

40. Kohn, W.; Sham, L. J. Self-Consistent Equations Including Exchange and Correlation Effects. *Physical Review* **1965**, *140*, A1133–A1138.

41. Su, N. Q.; Zhu, Z.; Xu, X. Doubly hybrid density functionals that correctly describe both density and energy for atoms. *Proceedings of the National Academy of Sciences* **2018**, *115*, 2287–2292.

42. Su, N. Q.; Xu, X. Development of New Density Functional Approximations. *Annual Review of Physical Chemistry* **2017**, *68*, 155–182.

43. Medvedev, M. G.; Bushmarinov, I. S.; Sun, J.; Perdew, J. P.; Lyssenko, K. A. Density functional theory is straying from the path toward the exact functional. *Science* **2017**, *355*, 49–52.

44. Cohen, A. J.; Mori-Sánchez, P.; Yang, W. Challenges for Density Functional Theory. *Chemical Reviews* **2012**, *112*, 289–320.

45. Kohn, W.; Becke, A. D.; Parr, R. G. Density Functional Theory of Electronic Structure. *The Journal of Physical Chemistry* **1996**, *100*, 12974–12980.

46. Becke, A. D. A new mixing of Hartree–Fock and local density-functional theories. *The Journal of Chemical Physics* **1993**, *98*, 1372–1377.

47. Perdew, J. P.; Ernzerhof, M.; Burke, K. Rationale for mixing exact exchange with density functional approximations. *The Journal of Chemical Physics* **1996**, *105*, 9982–9985.

48. Bogdanov, B.; McMahon, T. B. An Ab Initio and Density Functional Theory Investigation

of the Structures and Energetics of Halide Ion+Alcohol Complexes in the Gas Phase. *The Journal of Physical Chemistry A* **2000**, *104*, 7871–7880.

49. Hopkins, W. S.; Marta, R. A.; McMahon, T. B. Proton-Bound 3-Cyanophenylalanine Trimethylamine Clusters: Isomer-Specific Fragmentation Pathways and Evidence of Gas-Phase Zwitterions. *The Journal of Physical Chemistry A* **2013**, *117*, 10714–10718.

50. Featherstone, J.; Chong, T.; Martens, J. K.; Oomens, J.; McMahon, T. B. Inverse Sandwich Cyclopentadienyl Complexes of Sodium in the Gas Phase. *The Journal of Physical Chemistry A* **2018**, *122*, 8659–8664.

51. Kreienborg, N. M.; Merten, C. How to treat C-F stretching vibrations? A vibrational CD study on chiral fluorinated molecules. *Physical Chemistry Chemical Physics* **2019**, *21*, 3506–3511.

52. Mardirossian, N.; Head-Gordon, M. Thirty years of density functional theory in computational chemistry: an overview and extensive assessment of 200 density functionals. *Molecular Physics* **2017**, *115*, 2315–2372.

53. Walker, M.; Harvey, A. J.; Sen, A.; Dessent, C. E. Performance of M06, M06-2X, and M06-HF density functionals for conformationally flexible anionic clusters: M06 functionals perform better than B3LYP for a model system with dispersion and ionic hydrogen-bonding interactions. *Journal of Physical Chemistry A* **2013**,

54. Grimme, S.; Ehrlich, S.; Goerigk, L. Effect of the damping function in dispersion corrected density functional theory. *Journal of Computational Chemistry* **2011**,

55. Mardirossian, N.; Head-Gordon, M. ωb97X-V: A 10-parameter, range-separated hybrid, generalized gradient approximation density functional with nonlocal correlation, designed by a survival-of-the-fittest strategy. *Physical Chemistry Chemical Physics* **2014**, *16*, 9904–9924.

56. McQuarrie, D. A. *Statistical Mechanics.*; Harper and Row: New York, 1976; p 641.

57. McQuarrie, D. A. *Statistical thermodynamics.*; Harper and Row: New York, 1973; p 343.

58. Ochterski, J. W.; Ph, D. Thermochemistry in Gaussian. *Gaussian Inc Pittsburgh PA* **2000**,

59. Bruins, A. P. Mechanistic aspects of electrospray ionization. *Journal of Chromatography A* **1998**, *794*, 345–357.

60. Ho, C. S.; Lam, C. W. K.; Chan, M. H. M.; Cheung, R. C. K.; Law, L. K.; Lit, L. C. W.; Ng, K. F.; Suen, M. W. M.; Tai, H. L. Electrospray ionisation mass spectrometry: principles and clinical applications. *The Clinical biochemist. Reviews* **2003**, *24*, 3–12.

61. Wilm, M. S.; Mann, M. Electrospray and Taylor-Cone theory, Dole's beam of macromolecules at last? *International Journal of Mass Spectrometry and Ion Processes* **1994**, *136*, 167–180.

62. Soleilhac, A.; Dagany, X.; Dugourd, P.; Girod, M.; Antoine, R. Correlating Droplet Size with Temperature Changes in Electrospray Source by Optical Methods. *Analytical Chemistry* **2015**, *87*, 8210–8217.

63. Bakhoum, S. F. W.; Agnes, G. R. Study of Chemistry in Droplets with Net Charge before and after Coulomb Explosion: Ion-Induced Nucleation in Solution and Implications for Ion Production in an Electrospray. *Analytical Chemistry* **2005**, *77*, 3189–3197.

64. Taflin, D. C.; Ward, T. L.; Davis, E. J. Electrified droplet fission and the Rayleigh limit. *Langmuir* **1989**, *5*, 376–384.

65. Fenn, J. B.; Mann, M.; Meng, C. K.; Wong, S. F.; Whitehouse, C. M. Electrospray ionization-principles and practice. *Mass Spectrometry Reviews* **1990**, *9*, 37–70.

66. Iribarne, J. V. On the evaporation of small ions from charged droplets. *The Journal of Chemical Physics* **1976**, *64*, 2287–2294.

67. Wilm, M. Principles of Electrospray Ionization. *Molecular & Cellular Proteomics* **2011**, *10*, M111.009407(1–8).

68. Bakker, J. M.; Aleese, L. M.; Meijer, G.; von Helden, G. Fingerprint IR Spectroscopy to Probe Amino Acid Conformations in the Gas Phase. *Physical Review Letters* **2003**, *91*, 203003.

69. Lucas, B.; Grégoire, G.; Lemaire, J.; Maître, P.; Ortega, J.-M.; Rupenyan, A.; Reimann, B.; Pierre Schermann, J.; Desfrançois, C. Investigation of the protonation site in the dialanine peptide by infrared multiphoton dissociation spectroscopy. *Phys. Chem. Chem. Phys.* **2004**, *6*, 2659–2663.

70. Dopfer, O.; Solcà, N.; Lemaire, J.; Maitre, P.; Crestoni, M.-E.; Fornarini, S. Protonation Sites of Isolated Fluorobenzene Revealed by IR Spectroscopy in the Fingerprint Range. *The Journal of Physical Chemistry A* **2005**, *109*, 7881–7887.

71. Oomens, J.; Sartakov, B. G.; Meijer, G.; von Helden, G. Gas-phase infrared multiple photon dissociation spectroscopy of mass-selected molecular ions. *International Journal of Mass Spectrometry* **2006**, *254*, 1–19.

72. Hopkins, W. S. Determining the properties of gas-phase clusters. *Molecular Physics* **2015**, *113*, 3151–3158.

73. Fu, W.; Xiong, J.; Lecours, M. J.; Carr, P. J.; Marta, R. A.; Fillion, E.; McMahon, T.; Steinmetz, V.; Hopkins, W. S. The structures of proton-bound dimers of glycine with phenylalanine and pentafluorophenylalanine. *Journal of Molecular Spectroscopy* **2016**, *330*, 194–199.

74. Lecours, M. J.; Marta, R. A.; Steinmetz, V.; Keddie, N.; Fillion, E.; O'Hagan, D.; McMahon, T. B.; Hopkins, W. S. Interaction of $B_{12}X_{12}^{2-}$ with All-cis 1,2,3,4,5,6-Hexafluorocyclohexane in the Gas Phase. *The Journal of Physical Chemistry Letters* **2017**, *8*, 109–113.

75. Fu, W.; Carr, P. J. J.; Lecours, M. J.; Burt, M.; Marta, R. A.; Steinmetz, V.; Fillion, E.; McMahon, T. B.; Hopkins, W. S. Intramolecular cation–π interactions in protonated phenylalanine derivatives. *Physical Chemistry Chemical Physics* **2017**, *19*, 729–734.

76. Carr, P. J. J.; Lecours, M. J.; Burt, M. J.; Marta, R. A.; Steinmetz, V.; Fillion, E.; Hopkins, W. S. Mode-Selective Laser Control of Palladium Catalyst Decomposition. *The Journal of Physical Chemistry Letters* **2018**, *9*, 157–162.

77. De Vlugt, I. J. S.; Lecours, M. J.; Carr, P. J. J.; Anwar, A.; Marta, R. A.; Fillion, E.; Steinmetz, V.; Hopkins, W. S. Infrared-Driven Charge-Transfer in Transition Metal-Containing $B_{12}X_{12}{}^{2-}$ (X = H, F) Clusters. *The Journal of Physical Chemistry A* **2018**, *122*, 7051–7061.

78. Carr, P. J. J.; Warneke, J.; Featherstone, J.; Jenne, C.; Loire, E.; Hopkins, W. S. The structure of proton-bound Triethylammonia (X = F, Cl) Clusters. *Molecular Physics* **2019**, *117*, 2972–2979.

79. Prazeres, R.; Berset, J.; Glotin, F.; Jaroszynski, D.; Ortega, J. Optical performance of the CLIO infrared FEL. *Nuclear Instruments and Methods in Physics Research Section A: Accelerators, Spectrometers, Detectors and Associated Equipment* **1993**, *331*, 15–19.

80. Oepts, D.; van der Meer, A.; van Amersfoort, P. The Free-Electron-Laser user facility FELIX. *Infrared Physics & Technology* **1995**, *36*, 297–308.

81. Ortega, J.; Glotin, F.; Prazeres, R. Extension in far-infrared of the CLIO free-electron laser. *Infrared Physics & Technology* **2006**, *49*, 133–138.

82. Martens, J.; Berden, G.; Gebhardt, C. R.; Oomens, J. Infrared ion spectroscopy in a modified quadrupole ion trap mass spectrometer at the FELIX free electron laser laboratory. *Review of Scientific Instruments* **2016**, *87*, 103108.

83. March, R. E. An introduction to quadrupole ion trap mass spectrometry. *Journal of Mass Spectrometry* **1997**, *32*, 351–369.

84. Simon, A. Activation du méthane par deux cations métalliques de la troisième série, W+ et Ta+ : synergie entre expériences en phase gazeuse et calculs de chimie quantique. Ph.D. thesis, Universite Paris Sud, 2002.

85. Fink, T. M. A.; Ball, R. C. How Many Conformations Can a Protein Remember? *Physical Review Letters* **2001**, *87*, 198103.

86. Scheraga, H. A. Some approaches to the multiple-minima problem in the calculation of polypeptide and protein structures. *International Journal of Quantum Chemistry* **1992**, *42*, 1529–1536.

87. Piela, L.; Olszewski, K. A.; Pillardy, J. On the stability of conformers. *Journal of Molecular Structure: THEOCHEM* **1994**, *308*, 229–239.

88. Wales, D. J.; Doye, J. P. K. Global Optimization by Basin-Hopping and the Lowest Energy Structures of Lennard-Jones Clusters Containing up to 110 Atoms. *The Journal of Physical Chemistry A* **1997**, *101*, 5111–5116.

89. Lecours, M. J.; Chow, W. C. T.; Hopkins, W. S. Density Functional Theory Study of Rh n S 0,± and Rh n +1 0,± (n = 1–9). *The Journal of Physical Chemistry A* **2014**, *118*, 4278–4287.

90. Skyner, R. E.; McDonagh, J. L.; Groom, C. R.; Van Mourik, T.; Mitchell, J. B. A review of methods for the calculation of solution free energies and the modelling of systems in solution. *Physical Chemistry Chemical Physics* **2015**, *17*, 6174–6191.

91. Xu, L.; Fang, G.; Tao, J.; Ye, Z.; Xu, S.; Li, Z. Molecular Mechanism and Solvation Effect of Supramolecular Catalysis in a Synthetic Cavitand Receptor with an Inwardly Directed Carboxylic Acid for Ring-Opening Cyclization of Epoxy Alcohols. *ACS Catalysis* **2018**, *8*, 11910–11925.

92. Ren, P.; Chun, J.; Thomas, D. G.; Schnieders, M. J.; Marucho, M.; Zhang, J.; Baker, N. A. Biomolecular electrostatics and solvation: A computational perspective. *Quarterly Reviews of Biophysics* **2012**, *45*, 427–491.

93. Cramer, C. J.; Truhlar, D. G. Implicit Solvation Models: Equilibria, Structure, Spectra, and Dynamics. *Chemical Reviews* **1999**, *99*, 2161–2200.

94. Rappe, A. K.; Casewit, C. J.; Colwell, K. S.; Goddard, W. A.; Skiff, W. M. UFF, a full periodic table force field for molecular mechanics and molecular dynamics simulations. *Journal of the American Chemical Society* **1992**, *114*, 10024–10035.

95. Frisch, M. J. et al. Gaussian˜16 Revision B.01. 2016; Gaussian Inc. Wallingford CT.

96. Lebedev, V. I.; Laikov, D. N. A quadrature formula for the sphere of the 131st algebraic order of accuracy. *Doklady Mathematics* **1999**, *59*, 477–481.

97. Jeffrey, G. A. *An Introduction to Hydrogen Bonding*; Topics in Physical Chemistry - Oxford University Press; Oxford University Press, 1997; pp 12,14,191,200.

98. Orville-Thomas, W. Molecular spectra and molecular structure, iv, constants of diatomic molecules. *Journal of Molecular Structure* **1980**, *64*, 299.

99. Li, B.; Han, L. Distance weighted cosine similarity measure for text classification. Lecture Notes in Computer Science (including subseries Lecture Notes in Artificial Intelligence and Lecture Notes in Bioinformatics). 2013.

100. Fu, W.; Hopkins, W. S. Applying Machine Learning to Vibrational Spectroscopy. *The Journal of Physical Chemistry A* **2018**, *122*, 167–171.

101. O'Boyle, N. M.; Banck, M.; James, C. A.; Morley, C.; Vandermeersch, T.; Hutchison, G. R. Open Babel: An Open chemical toolbox. *Journal of Cheminformatics* **2011**,

102. Stewart, J. J. P. Optimization of parameters for semiempirical methods VI: more modifications to the NDDO approximations and re-optimization of parameters. *Journal of Molecular Modeling* **2013**, *19*, 1–32.

103. Martin, B. P.; Brandon, C. J.; Stewart, J. J.; Braun-Sand, S. B. Accuracy issues involved in modeling in vivo protein structures using PM7. *Proteins: Structure, Function and Bioinformatics* **2015**,

104. Stewart, J. J. An investigation into the applicability of the semiempirical method PM7 for modeling the catalytic mechanism in the enzyme chymotrypsin. *Journal of Molecular Modeling* **2017**,

105. Mato, J.; Guidez, E. B. Accuracy of the PM6 and PM7 Methods on Bare and Thiolate-Protected Gold Nanoclusters. *Journal of Physical Chemistry A* **2020**,

106. Buck, U.; Schmidt, B. A perturbation approach to predict infrared spectra of small molecular clusters applied to methanol. *The Journal of Chemical Physics* **1993**, *98*, 9410–9424.

107. Dang, L. X.; Chang, T.-M. Molecular dynamics study of water clusters, liquid, and liquid–vapor interface of water with many-body potentials. *The Journal of Chemical Physics* **1997**, *106*, 8149–8159.

108. König, S.; Fales, H. M. Formation and decomposition of water clusters as observed in a triple quadrupole mass spectrometer. *Journal of the American Society for Mass Spectrometry* **1998**, *9*, 814–822.

109. Kebarle, P.; Searles, S. K.; Zolla, A.; Scarborough, J.; Arshadi, M. Solvation of the hydrogen ion by water molecules in the gas phase. Heats and entropies of solvation of individual reactions. H+(H2O)n-1 + H2O .fwdarw. H+(H2O)n. *Journal of the American Chemical Society* **1967**, *89*, 6393–6399.

110. Kaya, Y.; Kalkan, Y.; Veenhof, R. Protonated water clusters in TPC's. *Nuclear Instruments and Methods in Physics Research Section A: Accelerators, Spectrometers, Detectors and Associated Equipment* **2016**, *824*, 535–537.

111. Kazachenko, S.; Bulusu, S.; Thakkar, A. J. Methanol clusters (CH3OH)n: Putative global minimum-energy structures from model potentials and dispersion-corrected density functional theory. *Journal of Chemical Physics* **2013**, *138*.

112. Neese, F. Software update: the ORCA program system, version 4.0. *WIREs Computational Molecular Science* **2018**, *8*.

113. Sure, R.; Grimme, S. Corrected small basis set Hartree-Fock method for large systems. *Journal of Computational Chemistry* **2013**, *34*, 1672–1685.

114. El-Shall, M. S.; Wright, D.; Ibrahim, Y.; Mahmoud, H. Theoretical study of styrene (methanol)n clusters, n = 1-9. Comparison with methanol clusters. *Journal of Physical Chemistry A* **2003**, *107*, 5933–5940.

115. Hagemeister, F. C.; Gruenloh, C. J.; Zwier, T. S. Density functional theory calculations of the structures, binding energies, and infrared spectra of methanol clusters. *Journal of Physical Chemistry A* **1998**, *102*, 82–94.

116. Fifen, J. J.; Nsangou, M.; Dhaouadi, Z.; Motapon, O.; Jaidane, N. E. Structures of protonated methanol clusters and temperature effects. *Journal of Chemical Physics* **2013**, *138*, 10–16.

117. White, M. C.; Mizrahi, R. E.; Ruliffson, J. E.; Khoury, M.; Melko, J. J. Mechanisms of sequential ion-molecule reactions in protonated methanol using mass spectrometry, ab initio methods, and statistical modeling. *Chemical Physics* **2019**, *525*, 110420.

118. Maheshwary, S.; Patel, N.; Sathyamurthy, N.; Kulkarni, A. D.; Gadre, S. R. Structure and stability of water clusters (H2O)n, n = 8-20: An ab initio investigation. *Journal of Physical Chemistry A* **2001**, *105*, 10525–10537.

119. Liu, X.; Lu, W. C.; Wang, C. Z.; Ho, K. M. Energetic and fragmentation stability of water clusters (H 2O)n, n = 2-30. *Chemical Physics Letters* **2011**, *508*, 270–275.

120. Shields, R. M.; Temelso, B.; Archer, K. A.; Morrell, T. E.; Shields, G. C. Accurate predictions of water cluster formation, (H2O) n=2-10. *Journal of Physical Chemistry A* **2010**, *114*, 11725–11737.

121. Hodges, M. P.; Wales, D. J. Global minima of protonated water clusters. *Chemical Physics Letters* **2000**, *324*, 279–288.

122. Sobolewski, A. L.; Domcke, W. Ab initio investigation of the structure and spectroscopy of hydronium-water clusters. *Journal of Physical Chemistry A* **2002**, *106*, 4158–4167.

123. Likholyot, A.; Lemke, K. H.; Hovey, J. K.; Seward, T. M. Mass spectrometric and quantum chemical determination of proton water clustering equilibria. *Geochimica et Cosmochimica Acta* **2007**, *71*, 2436–2447.

124. Yu, Q.; Bowman, J. M. Tracking Hydronium/Water Stretches in Magic H3O+(H2O)20 Clusters through High-level Quantum VSCF/VCI Calculations. *The Journal of Physical Chemistry A* **2020**, *124*, 1167–1175.

125. López-Corcuera, B.; Geerlings, A.; Aragón, C. Glycine neurotransmitter transporters: an update. *Molecular Membrane Biology* **2001**, *18*, 13–20.

126. Hobson, R. M.; Saunders, B.; Ball, G.; Harris, R. C.; Sale, C. Effects of β-alanine supplementation on exercise performance: a meta-analysis. *Amino Acids* **2012**, *43*, 25–37.

127. Quesnele, J. J.; Laframboise, M. A.; Wong, J. J.; Kim, P.; Wells, G. D. The Effects of Beta-Alanine Supplementation on Performance: A Systematic Review of the Literature. *International Journal of Sport Nutrition and Exercise Metabolism* **2014**, *24*, 14–27.

128. Hoffman, J. R.; Stout, J. R.; Harris, R. C.; Moran, D. S. β-Alanine supplementation and military performance. *Amino Acids* **2015**, *47*, 2463–2474.

129. Fischer, K. C.; Sherman, S. L.; Garand, E. Competition between Solvation and Intramolecular Hydrogen-Bonding in Microsolvated Protonated Glycine and β-Alanine. *Journal of Physical Chemistry A* **2020**, *124*, 1593–1602.

130. Marsh, B. M.; Voss, J. M.; Garand, E. A dual cryogenic ion trap spectrometer for the formation and characterization of solvated ionic clusters. *The Journal of Chemical Physics* **2015**, *143*, 204201.

131. Ieritano, C.; Featherstone, J.; Carr, P. J.; Marta, R. A.; Loire, E.; McMahon, T. B.; Hopkins, W. S. The structures and properties of anionic tryptophan complexes. *Physical Chemistry Chemical Physics* **2018**, *20*, 26532–26541.

132. Yamdagni, R.; McMahon, T. B.; Kebarle, P. Substituent Effects on The Intrinsic Acidities of Benzoic Acids Determined by Gas Phase Proton Transfer Equilibria Measurements. *Journal of the American Chemical Society* **1974**, *96*, 4035–4037.

133. McMahon, T. B.; Kebarle, P. Intrinsic acidities of substituted phenols and benzoic acids determined by gas phase proton transfer equilibriua. *J. Am. Chem. Soc.* **1977**, *99*, 2222–2230.

134. Fujio, M.; Mclver, R. T.; Taft, R. W. Effects on the Acidities of Phenols from Specific Substituent-Solvent Interactions. Inherent Substituent Parameters from Gas-Phase Acidities. *Journal of the American Chemical Society* **1981**, *103*, 4017–4029.

135. Bartmess, J. E.; Scott, J. A.; Mclver, R. T. Substituent and Solvation Effects on Gas-Phase Acidities. *Journal of the American Chemical Society* **1979**, *101*, 6056–6063.

136. Besler, B. H.; Merz, K. M.; Kollman, P. A. Atomic charges derived from semiempirical methods. *Journal of Computational Chemistry* **1990**, *11*, 431–439.

137. Singh, U. C.; Kollman, P. A. An approach to computing electrostatic charges for molecules. *Journal of Computational Chemistry* **1984**, *5*, 129–145.

138. Chai, J.-D.; Head-Gordon, M. Long-range corrected hybrid density functionals with damped atom–atom dispersion corrections. *Physical Chemistry Chemical Physics* **2008**, *10*, 6615.

139. Goddard, T. D.; Huang, C. C.; Meng, E. C.; Pettersen, E. F.; Couch, G. S.; Morris, J. H.; Ferrin, T. E. UCSF ChimeraX: Meeting modern challenges in visualization and analysis. *Protein Science* **2018**, *27*, 14–25.

140. Pettersen, E. F.; Goddard, T. D.; Huang, C. C.; Meng, E. C.; Couch, G. S.; Croll, T. I.; Morris, J. H.; Ferrin, T. E.<scp>UCSF ChimeraX</scp>: Structure Visualization for Researchers, Educators, and Developers. *Protein Science* **2020**, pro.3943.

141. Cossi, M.; Barone, V.; Cammi, R.; Tomasi, J. Ab initio study of solvated molecules: a new implementation of the polarizable continuum model. *Chemical Physics Letters* **1996**, *255*, 327–335.

142. Mennucci, B.; Tomasi, J. Continuum solvation models: A new approach to the problem of solute's charge distribution and cavity boundaries. *The Journal of Chemical Physics* **1997**, *106*, 5151–5158.

143. Haack, A.; Crouse, J.; Schlüter, F. J.; Benter, T.; Hopkins, W. S. A First Principle Model of Differential Ion Mobility: the Effect of Ion-Solvent Clustering. *Journal of the American Society for Mass Spectrometry* **2019**, *30*, 2711–2725.

144. Drahos, L.; Heeren, R. M.; Collette, C.; De Pauw, E.; Vékey, K. Thermal energy distribution observed in electrospray ionization. *Journal of Mass Spectrometry* **1999**, *34*, 1373–1379.

145. Naban-Maillet, J.; Lesage, D.; Bossée, A.; Gimbert, Y.; Sztáray, J.; Vékey, K.; Tabet, J. C. Internal energy distribution in electrospray ionization. *Journal of Mass Spectrometry* **2005**, *40*, 1–8.

146. Gabelica, V.; De Pauw, E.; Karas, M. Influence of the capillary temperature and the source pressure on the internal energy distribution of electrosprayed ions. *International Journal of Mass Spectrometry* **2004**, *231*, 189–195.

147. Keddie, N. S.; Slawin, A. M. Z.; Lebl, T.; Philp, D.; O'Hagan, D. All-cis 1,2,3,4,5,6-hexafluorocyclohexane is a facially polarized cyclohexane. *Nature Chemistry* **2015**, *7*, 483–488.

148. Gurs, J.E., Lightner, D. Organic Conformational Analysis and Stereochemistry from Circular Dichroism Spectroscopy. 2000.

149. Mcneii, D.; Snyder, R. G.; Schachtschneider, J. H.; Crowder, A.; Priettlangkura, P.; Hallam, H. E.; Planche, A. L.; Rogers, M. T.; Basus, J.; Bradley, C. H. Spectroscopic Detection of the Twist-Boat Conformation of Cyclohexane. A Direct Measurement of the Free Energy Difference between the Chair and the Twist-Boat. *J. Am. Chem. Soc.* **2000**, *97*, 3244–3246.

150. O'Hagan, D. Understanding organofluorine chemistry. An introduction to the C–F bond. *Chem. Soc. Rev.* **2008**, *37*, 308–319.

151. Aleese, L. M.; Simon, A.; McMahon, T. B.; Ortega, J.-M.; Scuderi, D.; Lemaire, J.; Maître, P. Mid-IR spectroscopy of protonated leucine methyl ester performed with an FTICR or a Paul type ion-trap. *International Journal of Mass Spectrometry* **2006**, *249-250*, 14–20.

152. Burt, M.; Wilson, K.; Marta, R.; Hasan, M.; Scott Hopkins, W.; McMahon, T. Assessing the impact of anion–π effects on phenylalanine ion structures using IRMPD spectroscopy. *Phys. Chem. Chem. Phys.* **2014**, *16*, 24223–24234.

153. Minenkov, Y.; Singstad, Å.; Occhipinti, G.; Jensen, V. R. The accuracy of DFT-optimized geometries of functional transition metal compounds: A validation study of catalysts for olefin metathesis and other reactions in the homogeneous phase. *Dalton Transactions* **2012**, *41*, 5526–5541.

154. Bachrach, S. M. Amine superbases stabilized by extended hydrogen bond networks. *Journal of Organic Chemistry* **2013**, *78*, 10909–10916.

155. Roca-Sabio, A.; Regueiro-Figueroa, M.; Esteban-Gómez, D.; de Blas, A.; Rodríguez-Blas, T.; Platas-Iglesias, C. Density functional dependence of molecular geometries in lanthanide(III) complexes relevant to bioanalytical and biomedical applications. *Computational and Theoretical Chemistry* **2012**, *999*, 93–104.

156. Rayne, S.; Forest, K. of short- through long-chain [n] acenes and [n] phenacenes. **2016**, *258*, 251–258.

157. Schenker, S.; Schneider, C.; Tsogoeva, S. B.; Clark, T. Assessment of popular DFT and semiempirical molecular orbital techniques for calculating relative transition state energies and kinetic product distributions in enantioselective organocatalytic reactions. *Journal of Chemical Theory and Computation* **2011**, *7*, 3586–3595.

158. Frisch, M. J.; Head-Gordon, M.; Pople, J. A. Semi-direct algorithms for the MP2 energy and gradient. *Chemical Physics Letters* **1990**, *166*, 281–289.

159. Frisch, M. J.; Head-Gordon, M.; Pople, J. A. A direct MP2 gradient method. *Chemical Physics Letters* **1990**, *166*, 275–280.

160. Roy, D.; Marianski, M.; Maitra, N. T.; Dannenberg, J. J. Comparison of some dispersion-corrected and traditional functionals with CCSD(T) and MP2 ab initio methods: Dispersion, induction, and basis set superposition error. *The Journal of Chemical Physics* **2012**, *137*, 134109.

161. Voss, J. M.; Fischer, K. C.; Garand, E. Accessing the Vibrational Signatures of Amino Acid Ions Embedded in Water Clusters. *Journal of Physical Chemistry Letters* **2018**,

162. Fischer, K. C.; Sherman, S. L.; Voss, J. M.; Zhou, J.; Garand, E. Microsolvation Structures of Protonated Glycine and l -Alanine. *Journal of Physical Chemistry A* **2019**,

163. Del Bene, J. E. Basis Set and Correlation Effects on Computed Lithium Ion Affinities †. *The Journal of Physical Chemistry* **1996**, *100*, 6284–6287.

164. Feller, D.; Dixon, D. A.; Nicholas, J. B. Binding Enthalpies for Alkali Cation-Benzene Complexes Revisited. *The Journal of Physical Chemistry A* **2000**, *104*, 11414–11419.

165. Kesharwani, M. K.; Brauer, B.; Martin, J. M. L. Frequency and Zero-Point Vibrational Energy Scale Factors for Double-Hybrid Density Functionals (and Other Selected Methods): Can Anharmonic Force Fields Be Avoided? *The Journal of Physical Chemistry A* **2015**, *119*, 1701–1714.

166. Pritchard, B. P.; Altarawy, D.; Didier, B.; Gibson, T. D.; Windus, T. L. New Basis Set Exchange: An Open, Up-to-Date Resource for the Molecular Sciences Community. *Journal of Chemical Information and Modeling* **2019**, *59*, 4814–4820.

167. Kashinski, D. O.; Chase, G. M.; Nelson, R. G.; Di Nallo, O. E.; Scales, A. N.; Vanderley, D. L.; Byrd, E. F. C. Harmonic Vibrational Frequencies: Approximate Global Scaling Factors for TPSS, M06, and M11 Functional Families Using Several Common Basis Sets. *Journal of Physical Chemistry A* **2017**, *121*, 2265–2273.

168. Alecu, I. M.; Zheng, J.; Zhao, Y.; Truhlar, D. G. Computational Thermochemistry: Scale Factor Databases and Scale Factors for Vibrational Frequencies Obtained from Electronic Model Chemistries. *Journal of Chemical Theory and Computation* **2010**, *6*, 2872–2887.

169. Ieritano, C.; Carr, P. J.; Hasan, M.; Burt, M.; Marta, R. A.; Steinmetz, V.; Fillion, E.; McMahon, T. B.; Scott Hopkins, W. The structures and properties of proton-and alkali-bound cysteine dimers. *Physical Chemistry Chemical Physics* **2016**, *18*, 4704–4710.

170. Drahos, L.; Heeren, R. M.; Collette, C.; De Pauw, E.; Vékey, K. Thermal energy distribution observed in electrospray ionization. *Journal of Mass Spectrometry* **1999**, *34*, 1373–1379.

171. Yamaguchi, Y.; Frisch, M.; Gaw, J.; Schaefer, H. F.; Binkley, J. S. Analytic evaluation and basis set dependence of intensities of infrared spectra. *The Journal of Chemical Physics* **1986**, *84*, 2262–2278.

172. Porezag, D.; Pederson, M. R. Infrared intensities and Raman-scattering activities within density-functional theory. *Physical Review B* **1996**, *54*, 7830–7836.

173. He, G.-X.; Kurita, M.; Ishii, I.; Wada, F.; Matsuda, T. New applications of crown ethers. 11. Structural effect of the counter anion on crown-ether mediated cation extraction and transport. A direct examination of the crown ether-cation complex in the organic phase of extraction and transport. *Journal of Membrane Science* **1992**, *69*, 61–73.

174. Mohammadzadeh Kakhki, R. Application of crown ethers as stationary phase in the chromatographic methods. *Journal of Inclusion Phenomena and Macrocyclic Chemistry* **2013**, *75*, 11–22.

175. Lakshmanan, V. I.; Vijayan, S. *A Review on Application of Crown Ethers in Separation of Rare Earths and Precious Metals*; 2018; pp 1913–1930.

176. Chehardoli, G.; Bahmani, A. The role of crown ethers in drug delivery. *Supramolecular Chemistry* **2019**, *31*, 221–238.

177. Glendening, E. D.; Landis, C. R.; Weinhold, F. NBO 6.0 : Natural bond orbital analysis program. *Journal of Computational Chemistry* **2013**, *34*, 1429–1437.

178. Kealy, T. J.; Pauson, P. L. A New Type of Organo-Iron Compound. *Nature* **1951**, *168*, 1039–1040.

179. Wilkinson, G.; Rosenblum, M.; Whiting, M. C.; Woodward, R. B. THE STRUCTURE OF IRON BIS-CYCLOPENTADIENYL. *Journal of the American Chemical Society* **1952**, *74*, 2125–2126.

180. Jutzi, P.; Burford, N. Structurally Diverse π-Cyclopentadienyl Complexes of the Main Group Elements. *Chemical Reviews* **1999**, *99*, 969–990.

181. Sunner, J.; Nishizawa, K.; Kebarle, P. Ion-solvent molecule interactions in the gas phase. The potassium ion and benzene. *The Journal of Physical Chemistry* **1981**, *85*, 1814–1820.

182. Amicangelo, J. C.; Armentrout, P. B. Absolute Binding Energies of Alkali-Metal Cation Complexes with Benzene Determined by Threshold Collision-Induced Dissociation Experiments and ab Initio Theory. *The Journal of Physical Chemistry A* **2000**, *104*, 11420–11432.

183. Dougherty, D. A. The Cation-π Interaction. *Accounts of Chemical Research* **2013**, *46*, 885–893.

184. Kolakkandy, S.; Pratihar, S.; Aquino, A. J. A.; Wang, H.; Hase, W. L. Properties of Complexes Formed by Na^+, $Mg_2{}^+$, and $Fe_2{}^+$ Binding with Benzene Molecules. *The Journal of Physical Chemistry A* **2014**, *118*, 9500–9511.

185. Davis, M. R.; Dougherty, D. A. Cation–π interactions: computational analyses of the aromatic box motif and the fluorination strategy for experimental evaluation. *Physical Chemistry Chemical Physics* **2015**, *17*, 29262–29270.

186. Dunbar, R. C. Complexation of Na^+ and K^+ to Aromatic Amino Acids: A Density Functional Computational Study of Cation-π Interactions. *The Journal of Physical Chemistry A* **2000**, *104*, 8067–8074.

187. Harder, S.; Prosenc, M. H. The Simplest Metallocene Sandwich: the Lithocene Anion. *Angewandte Chemie International Edition in English* **1994**, *33*, 1744–1746.

188. Harder, S.; Prosenc, M. H.; Rief, U. Syntheses and X-ray Structures of Anionic Sodocene Sandwiches †. *Organometallics* **1996**, *15*, 118–122.

189. Streitwieser, A.; Smith, K. A. Inverse sandwich compounds. *Journal of Molecular Structure: THEOCHEM* **1988**, *163*, 259–265.

190. Wessel, J.; Lork, E.; Mews, R. Alkali Metallocene Anions: Syntheses and Structures. *Angewandte Chemie International Edition in English* **1995**, *34*, 2376–2378.

191. Frisch, M. J. et al. Gaussian 09 Revision D.01. 2009; Gaussian Inc. Wallingford CT.

192. Garbuzova, I.; Garkusha, O.; Lokshin, B.; Borisov, G.; Morozova, T. Vibrational spectra of alkali metal cyclopentadienides. *Journal of Organometallic Chemistry* **1985**, *279*, 327–335.

193. Garkusha, O.; Garbuzova, I.; Lokshin, B.; Nesmeyanov, A.; Borisov, G. Infrared spectra of cyclopentadienyl-alkali metal (Li, Na) ion pairs in tetrahydrofuran and hexamethylphosphoric triamide. *Journal of Organometallic Chemistry* **1987**, *336*, 13–22.

194. Dinnebier, R. E.; Behrens, U.; Olbrich, F. Solid State Structures of Cyclopentadienyllithium, -sodium, and -potassium. Determination by High-Resolution Powder Diffraction. *Organometallics* **1997**, *16*, 3855–3858.

195. Masubuchi, T.; Ohi, K.; Iwasa, T.; Nakajima, A. Experimental and theoretical studies on the electronic properties of vanadium-benzene sandwich cluster anions, $V_nBz_{n+1}^+$ (n = 1-5). *The Journal of Chemical Physics* **2012**, *137*, 224305.

196. Masubuchi, T.; Iwasa, T.; Nakajima, A. Experimental and theoretical studies of the structural and electronic properties of vanadium–benzene sandwich clusters and their anions: $V_nBz_n^{0/+}$ (n = 1–5) and $V_nBz_{n-1}^{0/+}$ (n = 2–5). *The Journal of Chemical Physics* **2014**, *141*, 214304.